Characteristics of Scalar Admixture in the Atmospheric Boundary Layer and Estimation of Regional Surface Fluxes Over Semi-arid Area

January 2006

Ayumi KOTANI

Characteristics of Scalar Admixture in the Atmospheric Boundary Layer and Estimation of Regional Surface Fluxes Over Semi-arid Area

A Dissertation Submitted to
the Graduate School of Life and Environmental Sciences.
the University of Tsukuba
in Partial Fulfilment of the Requirements
for the Degree of Doctor of Philosophy in Science
(Doctoral Program in Geoenvironmental Sciences)

Ayumi KOTANI

Abstract

Turbulence data obtained by aircraft observations in the mixed layer was analysed to estimate the regional surface heat fluxes through the application of the variance methods. Several heights within and above the mixed layer were flown repeatedly above the flux observation site in a steppe region in Mongolia. The observed profiles of temperature and humidity showed vertical development of the mixed layer and scatter of the second order moments, i.e., the variance, near the top due to the effects of entrainment heat flux from the above atmosphere. The vertical profiles of the dimensionless temperature variance were found to follow, in most of the cases, the functional forms proposed in previous studies.

These variance statistics were applied to the variance formulations to estimate surface sensible heat fluxes. First, the flux estimation was made with these equations and the constant parameters as derived in previous studies. Then, the constants were re-calibrated with the current data set and eddy correlation measurements on the ground. These constants were, then, used for the second flux estimation. Finally, additional variables, which represent the large scale atmospheric conditions, namely baroclinicity and horizontal temperature advection, were considered for improvement of the flux estimation. The resulting root mean square difference of the sensible heat flux by estimation and ground based measurements was reduced from about 40-100 W m^{-2} for the results obtained with the constants and formulations by the previous studies, to 30 W m^{-2} or less for those obtained with locally calibrated constants and introduction of four additional variables. Difference among types of formulation was not significant, and thus the usage of simpler formulation, which needs less number of parameters, is preferable for the practical application of the variance methods. The major cause of estimation error in variance methods was error of temperature variance, which is possible to be maximal at the higher level for free convection formulation and middle level for the others.

The present analyses reveal that the mixed layer variance methods are capable of producing surface fluxes with turbulence data measured from an aircraft. However, it also indicates that there remains some uncertainty, which partly comes from the sampling error of temperature fluctuations by aircraft observation due to insufficient data length and the reliability in evaluation of the surface flux as reference value and its spatial representation. As a whole, it is not clear at this point whether or not the need of the local calibration is an indication of the lack of universality of the equations, given the wide range of data sets employed in the past. The need for calibration means that these experimental constants would contain uncertainties of data set and the formulations including unsuitable scaling and parameters, and the reduction of the error by the local calibration suggests that refinement of the formulations is still needed for the estimation of the surface flux by the mixed layer variance methods with sufficient accuracy.

Keywords: mixed layer, variance methods, similarity approach, regional surface flux, aircraft observations

Table of Contents

Abstract i
Table of Contents ii
List of Tables iv
List of Figures v
List of Symbols viii
List of Abbreviations xii

1 Introduction 1
1-1 A Review of Recent Studies 2
1-1-1 Scalar Admixture Profile Formulations in the Mixed Layer 2
1-1-2 Methods to Estimate Surface Fluxes from Mixed Layer Data 4
1-2 Objective of This Study 5

2 Methods 7
2-1 Study Area 7
2-2 Aircraft Observations 13
2-3 Ground Based Observations 20
2-4 Large Scale Atmospheric Data 25

3 Scalar Variance Relationships in the Mixed Layer 28
3-1 Vertical Structure of Scalar Admixture in the Observed Mixed Layer 28
3-2 Formulations of Scalar Variance in the Mixed Layer 37
3-2-1 Validity of Similarity Arguments and Scaling Scheme in the Mixed Layer 37
3-2-2 Profile Equations of Variance Statistics 39
(1) Free Convective Formulation 39
(2) Formulation by Sorbjan (1989) 40
(3) Top-down and Bottom-up Diffusion Model 41
3-2-3 Comparisons with Observed Data 43

4 Surface Flux Estimation with Variance Methods 49
4-1 Derivation of Flux-Variance Formulations 49
4-2 Calibrations of the Experimental Coefficients 52
4-3 Addition of Large Scale Atmospheric Parameters 72
4-4 Validity of the Variance Methods 84

5 Remaining Issues of Mixed Layer Variance Methods 93
5-1 Observation Uncertainty in This Study 93
5-1-1 Variance Observations by Aircraft 93
5-1-2 Surface Flux Observations at the Ground Station 95
5-2 Universality of Scalar Variance Formulations in the Mixed Layer 103

6 Conclusions 105

Acknowledgements 108

References 110

Appendices 118
A-1 Estimation of Mixed Layer Height 118
A-2 Estimation of Regional Friction Velocity 118
A-3 Evaluation of Large Scale Atmospheric Parameters 121

List of Tables

2-1 Instruments for the observation aboard aircraft 14
2-2 Flight segments information above the KBU area..... 17
2-3 Instruments for the observation at the KBU flux station 22

4-1 List of constants in variance profile equations..... 50

4-2 Statistics in the comparison of flux, $\overline{w'\theta'_s}$ derived form the eddy covariance method at the ground station, and $\overline{w'\theta'_{vm}}$ estimated by the variance methods 59

4-3 Dimensionless parameters added to variance equations 74
4-4 Statistics in the comparison of flux, $[\sigma_\theta^2 T_*^{-2}]_{\mathrm{air}}$ derived form the aircraft observations, and $[\sigma_\theta^2 T_*^{-2}]_{\mathrm{pro}}$ estimated by the variance formulations..... 92

5-1 Statistics in the comparison of flux, $\overline{w'\theta'_s}$ derived form the eddy covariance method at the ground station, and $\overline{w'\theta'_{vm}}$ estimated by the variance methods, but correction for $\overline{w'\theta'_s}$ was not carried out. 100

A-1 Estimation of surface roughness length with DEM data..... 122

List of Figures

2-1 Location of the experimental area 8
2-2 Topographic map of the study area based on GTOPO30 dataset with the flight paths 9
2-3 Vegetation distribution in the study area based on Saandar and Sugita (2004) 10
2-4 Topographic map with ASTER true color image of the KBU area with all the flight segments 11
2-5 Photographs of the landscape around the KBU flux station 12
2-6 Schematic diagram of the observation system aboard aircraft 15
2-7 Photographs of the observation system aboard aircraft 16
2-8 Power spectra *fS* for temperature fluctuation as a function of cyclic frequency *f* 19
2-9 Trend removal procedure applied to a temperature time series 21
2-10 Schematic diagram of the observation system of the KBU flux station 23
2-11 Photograph of the observation system of the KBU flux station 24
2-12 Distribution of TERC-RAMS grid points 26

3-1 Vertical profiles of mean potential temperature θ observed above the KBU area 29
3-2 Same as 3-1 but for mean specific humidity q 30
3-3 Same as 3-1 but with y-axis normalized height ξ 31
3-4 Same as 3-1 but for mean specific humidity q and with y-axis normalized height ξ . 32
3-5 Same as 3-1 but for variance of potential temperature σ_θ^2 33
3-6 Same as 3-1 but for correlation coefficient of potential temperature θ and specific humidity q 34
3-7 Same as 3-5 but with y-axis normalized height ξ 35
3-8 Same as 3-6 but with y-axis normalized height ξ 36
3-9 Same as 3-7 but for normalized potential temperature variance $\sigma_\theta^2 T_*^{-2}$ with y-axis normalized height ξ, with previously proposed profile equations 38
3-10a Comparison between the normalized variance of potential temperature $[\sigma_\theta^2 T_*^{-2}]_{\mathrm{pro}}$ estimated with Eq.(3.2) and $[\sigma_\theta^2 T_*^{-2}]_{\mathrm{air}}$ that of observed above the KBU area 44
3-10b Same as 3-10a but for Eq.(3.3) and the data of normalized height $\xi < 0.8$ 45
3-10c Same as 3-10a but for Eq.(3.5) and the data of normalized height $\xi < 0.8$ 46
3-10d Same as 3-10a but for Eq.(3.10) and the data of normalized height $\xi < 0.8$ 48

4-1a Comparison between the sensible heat fluxes $\overline{w'\theta'}_{vm}$ estimated from Eq. (4.1) with the original constants in the literatures and $\overline{w'\theta'}_s$ observed by eddy

covariance method at the KBU flux station 53
4-1b Same as 4-1a but for Eq. (4.2) and the data of normalized height $\xi < 0.8$..... 54
4-1c Same as 4-1a but for Eq. (4.3) and the data of normalized height $\xi < 0.8$..... 55
4-1d Same as 4-1a but for Eq. (4.4) with velocity scale $v_0 = v_h = w_*$ and entrainment model (3.4), and the data of normalized height $\xi < 0.8$ 56
4-1e Same as 4-1a but for Eq. (4.4) with velocity scale $v_0 = v_*$, $v_h = w_*$ and entrainment model (3.4), and the data of normalized height $\xi < 0.8$ 57
4-1f Same as 4-1a but for Eq. (4.4) with velocity scale $v_0 = v_h = v_*$ and entrainment model (3.9), and the data of normalized height $\xi < 0.8$ 58
4-2a Comparison between the sensible heat fluxes $\overline{w'\theta'}_{vm}$ estimated from Eq. (4.1) with calibrated constants and $\overline{w'\theta'}_s$ observed by the eddy covariance method at the KBU flux station 61
4-2b Same as 4-2a but for Eq. (4.1) and the data of normalized height $\xi < 0.8$..... 62
4-2c Same as 4-2a but for Eq. (4.2) and the data of normalized height $\xi < 0.8$..... 63
4-2d Same as 4-2a but for Eq. (4.3) and the data of normalized height $\xi < 0.8$..... 64
4-2e Same as 4-2a but for Eq. (4.4) with velocity scale $v_0 = v_h = w_*$ and entrainment model (3.4), and the data of normalized height $\xi < 0.8$ 65
4-2f Same as 4-2a but for Eq.(4.4) with velocity scale $v_0 = v_*$, $v_h = w_*$ and entrainment model (3.4), and the data of normalized height $\xi < 0.8$ 66
4-2g Same as 4-2a but for Eq.(4.4) with velocity scale $v_0 = v_h = v_*$ and entrainment model (3.9), and the data of normalized height $\xi < 0.8$ 67
4-3a Sensitivity test of the variance methods of Eq. (4.4) with the original constants in the literatures for different velocity scale..... 68
4-3b Same as 4-3a but for Eq. (4.4) with calibrated constants..... 69
4-4 Vertical distribution of difference between estimation by means of (4.4) with different velocity scale and observed flux $\overline{w'\theta'}_{vm} - \overline{w'\theta'}_s$ 71
4-5a Comparison between the sensible heat fluxes $\overline{w'\theta'}_{vm}$ estimated from Eq. (4.1) with calibrated constants and additional dimensionless parameters and $\overline{w'\theta'}_s$ observed by eddy covariance method at the KBU flux station 76
4-5b Same as 4-5a. but for Eq. (4.1) with data at normalized height $\xi < 0.8$..... 77
4-5c Same as 4-5a. but for Eq. (4.2) with data at normalized height $\xi < 0.8$..... 78
4-5d Same as 4-5a. but for Eq. (4.3) with data at normalized height $\xi < 0.8$..... 79
4-5e Same as 4-5a. but for Eq. (4.4) with $v_0 = v_h = w_*$, entrainment model (3.4) and data at normalized height $\xi < 0.8$..... 80
4-6a Number of additional dimensionless parameters and resulted rms (root mean square) difference between $\overline{w'\theta'}_s$ derived form eddy covariance method at the KBU flux station, and $\overline{w'\theta'}_{vm}$ estimated by the variance methods (4.4) with $v_h = v_0 = w_*$ and entrainment model (3.4) 81
4-6b Same as 4-6a but for μ, ν, β_x, β_y and γ..... 82

4-6c Same as 4-6a but for μ, ν, β, γ_x and γ_y 83
4-7 Error propagation analysis for the variance methods 86
4-8a Comparison between the normalized variance of potential temperature $[\sigma_\theta^2 T_*^{-2}]_{pro}$ estimated from Eq. (3.2) with calibrated constants and $[\sigma_\theta^2 T_*^{-2}]_{air}$ that of observed above the KBU area 88
4-8b Same as 4-8a but for Eq. (3.3) and data at normalized height $\xi < 0.8$ 89
4-8c Same as 4-8a but for Eq. (3.10) and data at normalized height $\xi < 0.8$ 90
4-8d Same as 4-8a but for Eq. (3.11) and data at normalized height $\xi < 0.8$ 91

5-1 Vertical profile of normalized variance of potential temperature $\sigma_\theta^2 T_*^{-2}$ observed above the KBU area with previously proposed profile equations 97
5-2 Comparison between the sensible heat flux $\overline{w'\theta'}_{vm}$ estimated from Eq.(4.4) with original constants and $\overline{w'\theta'}_s$ observed by eddy covariance method with and without energy closed correction at the KBU flux station. 98
5-3 Same as 5-2 but for Eq.(4.4) with calibrated constants 99

List of Symbols

A	silhouette area of the roughness elements on a horizontal area S
A_G	universal function in Rossby-number similarity (A.1)
A_θ	entrainment constant
$A_1 - A_6$	constant coefficient in Eq. (A.9)
a	constant coefficient in Eq. (3.2)
a	coefficient in linear regression $y = ax + b$ (in chapter 2 and Table 2-2, 2-4 and 5-1)
a_{RE}	constant coefficient in the random error equation (5.2)
a_1 - a_7	constant coefficient in Eq. (3.6)
B	constant coefficient in Eq. (3.8)
B_G	universal function in Rossby-number similarity (A.1)
b	coefficient in linear regression $y = ax + b$ (in chapter 2 and Table 2-2, 2-4 and 5-1)
b_1 - b_4	constant coefficient in Eq. (3.10)
C_{Rau}	constant coefficient in Eq. (5.4)
$C_{m\theta_0}$	constant coefficient in Eq. (3.3)
$C_{m\theta_i}$	constant coefficient in Eq. (3.3)
c	constant coefficient in Eq. (A.3)
c_1 - c_9	constant coefficient in Eq. (4.12)
c_p	specific heat of air at constant pressure (J kg^{-1} K^{-1})
D	the ratio Δ / h_i
D_{EB}	energy balance closure ($D_{EB} = (H+LE)/(R_n+G)$)
$D_{h/2}$	drag coefficient of the major obstacles at $z = h$ / 2
d_0	displacement height (m)
F	form drag

f	the Coriolis parameter (s^{-1})
f_b	universal function of ξ in Eq. (3.5)
f_{tb}	universal function of ξ in Eq. (3.5)
f_t	universal function of ξ in Eq. (3.5)
f_p	spectral peak frequency (Hz)
G	ground heat flux (W m^{-2})
GW	geostrophic wind (m s^{-1})
g	gravity acceleration (m s^{-2})
H	sensible heat flux (W m^{-2})
h	mean height of the major obstacles
h_i	height of mixed layer / convective boundary layer (m)
h_r	the Ekman height scale $h_r = \kappa u_* f^{-1}$ (m)
k	von Kármán's constant
L	the Obukhov length (m)
L_{Rau}	surface heterogeneous scale (m)
L_{θ^2}	averaging length for temperature variance
LE	latent heat flux (W m^{-2})
P	functional form of additional parameters
p	air pressure (hPa)
q	specific humidity of air (kg kg^{-1})
R_n	net radiation (W m^{-2})
$r_{\theta q}$	correlation coefficients between potential temperature and specific humidity
S	horizontal area on which roughness elements exist
T_a	air temperature (K)
T_*	mixed layer (convective) temperature scale (K)
U	wind speed (m s^{-1})
U_g	eastward component of geostrophic wind speed (m s^{-1})

$u_{h/2}$	wind speed at $z = h / 2$ (m s^{-1})
u_*	friction velocity (m s^{-1})
V_g	northward component of geostrophic wind speed (m s^{-1})
v_0	velocity scale at the surface (m s^{-1})
v_h	velocity scale at the inversion base (m s^{-1})
v_*	combined velocity scale $v_* = (w_*^3 + 8u_*^3)^{1/3}$ (m s^{-1})
w_*	mixed layer (convective) velocity scale (m s^{-1})
$\overline{w'\theta'}_0$	surface temperature flux $\overline{w'\theta'}_0 = H/(\rho c_p)$ (K m s^{-1})
$\overline{w'\theta'}_h$	entrainment (inversion) temperature flux (K m s^{-1})
$\overline{w'\theta'}_s$	surface temperature flux observed at ground station (K m s^{-1})
$\overline{w'\theta'}_{vm}$	surface temperature flux estimated by variance methods (K m s^{-1})
z	height of measurement (m)
z_0	surface roughness length (m)
z_{0l}	local roughness length of the surface (m)
β	dimensionless parameter $\beta = \left(\beta_x^2 + \beta_y^2\right)^{1/2}$
β_x	dimensionless parameter $\beta_x = \frac{\partial u_g}{\partial z}\left(\frac{h_i}{h_r}\right)^2 \frac{1}{\lvert f \rvert}$
β_y	dimensionless parameter $\beta_y = \frac{\partial v_g}{\partial z}\left(\frac{h_i}{h_r}\right)^2 \frac{1}{\lvert f \rvert}$
γ	dimensionless parameter $\gamma = \left(\gamma_x^2 + \gamma_y^2\right)^{1/2}$
γ_x	dimensionless parameter $\gamma_x = \frac{\partial \overline{u}\overline{\theta}}{\partial x}\frac{h_i}{\overline{w'\theta'}_0}$
γ_y	dimensionless parameter $\gamma_y = \frac{\partial \overline{v}\overline{\theta}}{\partial y}\frac{h_i}{\overline{w'\theta'}_0}$
Δ	depth of interfacial (entrainment) layer (m)
δ	absolute error

θ air potential temperature (K)

θ_* surface layer temperature scale $\theta_* = -\overline{w'\theta'}_0 u_*^{-1}$ (K)

λ roughness density $\lambda = AS^{-1}$

λ_{θ^2} integral length scale of temperature variance

μ stability parameter $\mu = h_i L^{-1}$

ν dimensionless parameter $\nu = h_i h_r^{-1}$

ξ normalized mixed layer height $\xi = z h_i^{-1}$

ρ air density (kg m^{-3})

$\sigma_\theta{}^2$ variance of potential temperature (K^2)

Ψ_m stability correction function for momentum

$\partial \overline{u}\overline{\theta} / \partial x$ eastward component of horizontal temperature advection

$\partial U_g / \partial z$ vertical gradient of eastward component of geostrophic wind speed

$\partial \overline{v}\overline{\theta} / \partial y$ northward component of horizontal temperature advection

$\partial V_g / \partial z$ vertical gradient of northward component of geostrophic wind speed

List of Abbreviations

ABL	atmospheric boundary layer
CBL	convective boundary layer
HFP	heat flux plate
IRGA	Infrared Gas Analyzer
IRT	infrared thermometer
KBU	Kherlen Bayan-Ulaan
LES	large-eddy simulation
PRT	platinum resistance thermometer
REBS	Radiation and Energy Balance Systems
rms	root mean square
SAT	sonic anemometer-thermometer
TDBU	top-down bottom-up
TDR	time domain reflectmetry

1 Introduction

Knowledge of the exchange process and amount of energy, mass and momentum between the land surfaces and the atmosphere gives us important information because they have direct influence to our living environment near the ground surface. It is also required in many situations; behaviours and quantity of anthropogenic traceable gases for air pollution problem or global warming issues (Arya, 1999), flux of water vapour, i.e., evapotranspiration for water resource management and atmospheric circulation studies (Garrat et al, 1996).

The atmospheric boundary layer (ABL) is an interface between the earth's surface and the atmosphere. The daytime ABL, namely the convective boundary layer (CBL), in which the air transport is driven mainly by turbulence, can be divided into three sublayers; the surface layer is extended from the surface to about 10 percent of the whole CBL (sometimes when the height of the lowest layer is the same order of roughness obstacles, it is treated separately as the roughness sublayer) and characterized by large gradients of scalar admixture with its source/sink in the surface and wind speed for example, and nearly constant fluxes of heat and momentum; the mixed layer above the surface layer occupies the middle of CBL and forms vigorous turbulence mixing by convection driven by buoyancy and shear effects, which results vertically uniform distribution of scalars and wind speed; the upper limit of the mixed layer to the free atmosphere is the interfacial (or the entrainment) layer. By following the air motion in the CBL, scalar admixture such as temperature, water vapor, CO_2, and various tracer gases are transported between the earth surface and free atmosphere, or sometimes remained inside the CBL. Since the physical state of the CBL probably reflects the surface fluxes with horizontal scales of the order of 10^2-10^5 m (e.g., Raupach and Finnigan, 1995), several approaches to derive surface fluxes with the CBL (mainly the mixed layer) observations have been developed and tested in the past (see next section).

In order to describe the ABL (or CBL) turbulence status, theoretical treatment has been developed with the similarity arguments based on the dimensional analysis, which provides means of grouping the variables into some dimensionless parameters and organizing the

experimental data in the most efficient manner to derive universal similarity relationships (e.g., Arya, 2001; Stull, 1988). The similarity theory and its non-dimensional formulations are independent of the systems of units used and enable order-of-magnitude estimates and comparisons with data obtained elsewhere, and furthermore, often contribute to the discovery of simple functional relationships (Tennekes, 1982). The ABL similarity approach had been developed mainly in the surface layer studies; one of the most important arguments is Monin-Obukhov similarity (Monin and Obukhov, 1954; Monin and Yaglom, 1971; Kader and Yaglom, 1990), which described the mean gradients and turbulence characteristics as a function of variables relevant in the surface layer such as the height from the ground, the buoyancy variable, the kinematic surface stress and heat flux. Those similarity functions described above had been evaluated with extensive data sets obtained through the field, laboratory and numerical experiments for the past few decades, and today they are accepted widely, with some known exceptions such as the breakdown of the surface layer scaling with horizontal velocity fluctuations (e.g., Garrat, 1992). In contrast, such a framework for the mixed layer has not yet met enough arguments and studies as described next section.

In this study, characteristics of the scalar admixture in the mixed layer are focused on and dealt with, with an approach based on the similarity argument.

1-1 A Review of Recent Studies

1-1-1 Scalar Admixture Profile Formulations in the Mixed Layer

For the mixed layer, generalizing treatments of variables have been attempted and a few similarity laws were investigated mainly as expansion of the surface layer theories. There are unique problems for the mixed layer (sometimes also including the interfacial layer) such as the role of entrainment flux from the free atmosphere and the treatment of large scale convective eddies appearing sometimes as counter-gradient heat flux, which lead to the breakdown of Monin-Obukhov similarity, in flux measurements and turbulence closure schemes (Garrat et al, 1996). Generally, in similarity approach, the number of relevant parameters whose effect is not

negligible in the mixed layer is larger than those of the surface layer (Brutsaert and Mawdsley, 1976). The mean flow and the turbulent structure of the mixed layer depend on the mixed layer height, entrainment flux, large scale advection, subsidence, geostrophic wind shear, wind speed at the top of the mixed layer and so on, in addition to the surface layer variables mentioned above. Derivation of the generalized similarity formulation with these possible variables requires both an understanding of the related phenomena and a high quality data set for the verification.

A number of investigations for the turbulent and scalar fields of the mixed layer and related processes have been attempted through the field observations, laboratory experiments and numerical simulations in the past decades. The major attempt related to the mixed layer scalar structure has been based on the top-down and bottom-up (TDBU) diffusion concept, which states that the scalar fluxes can be separated to downward mixing from the top of the mixed layer and upward one from the ground surface (Wyngaard and Brost, 1984). The top-down component, generally mentioned as the entrainment flux or countergradient flux, is one of the most important factors for the formulation of the scalar profile in the mixed layer. The ratio of the entrainment flux to the surface flux is one of indicators that predict the structure (or profile formulation) of scalar admixture in the mixed layer (e.g., Caughey and Palmer, 1976; van Dop et al., 2005), and its parameterisation has been studied (e.g., Tennekes, 1973; De Roode et al., 2004). In contrast, the effect of the bottom-up component, i.e., surface fluxes, is recently investigated from the viewpoint of surface heterogeneity. A large-eddy simulation (LES) results of Hechtel et al. (1990) show a comparison of vertical profiles of wind and scalar variance over heterogeneous at the order of 100 m and homogeneous surface, which is not significantly different, while Strunin et al. (2004) find, with aircraft observation, a breakdown of the mixed layer scaling over an area with heterogeneous surface thermal condition over some horizontal scale comparable to the ABL scale. Kim et al. (2004) also present that a relation of surface heat flux distribution and background wind affects wind and temperature fields in the boundary layer by a LES.

In addition, scalar fluctuations caused by mesoscale scalar gradient has the same order of magnitude as those of the top-down and bottom-up scalars (Jonker et al., 1999; Kimmel et al., 2002), which indicates a breakdown of assumed horizontal homogeneity. Also the baroclinicity effect to the mixed layer structure has been investigated; a modification of thermal and turbulent

structure was found to be caused through horizontal advection of cold or warm air and baroclinic wind shear (Sorbjan, 2004; Sorbjan, 2005). As for the momentum in the mixed layer, baroclinicity and acceleration (namely, local change and advection of momentum) effect contributes similarity formulations (Crago and Brutsaert, 1994, 1995).

As similarity arguments, generalization of these results has not been fully achieved, and a fundamental question, namely whether similarity laws for the conservative scalar admixture, or especially its fluctuation, would exist with these variables in the mixed layer, remains unanswered.

1-1-2 Methods to Estimate Surface Fluxes from Mixed Layer Data

As mentioned in the previous section, several approaches to derive surface fluxes of regional scale with CBL (mainly focused on the mixed layer) observations have been developed and were tested in the past. Examples of such approaches include the eddy covariance method (e.g., Lenschow et al., 1980), the profile or a bulk method of the CBL (e.g., Brutsaert and Sugita, 1991) and the CBL budget approach (e.g., Kustas and Brutsaert, 1987a, 1987b; Betts and Ball, 1994; Cleugh et al., 2004) with data obtained by sensors on a tower (e.g., Berger et al., 2001), on radiosondes (e.g., Sugita et al., 1999), aboard an aircraft (e.g., Lenschow et al., 1980), or by means of ground-based remote sensing devices such as Radar (e.g., Eng et al., 2003). Among them, aircraft measurements have the advantage in both deriving area-averaged values and detecting the spatial variability depending on the object, but they are not without disadvantages. The most notable feature is the random movement of an aircraft as a platform of observations. It continuously moves in all directions, and thus it requires simultaneous measurements of its precise position and also sophisticated and cumbersome treatment of the data afterward in order to allow vector data analysis, in particular for the application of the eddy covariance technique (e.g., Lenschow, 1986).

Methods to estimate surface fluxes from the associated variance measurements, on the other hand, are appealing particularly for the aircraft observation because they allowed the derivation of surface fluxes only from measurements of a scalar variable without data processing

needed for the eddy covariance method as mentioned above. Also, the fluxes to be estimated are those at the surface, unlike those obtained by the eddy covariance method that produces local fluxes at the measurement height. It is often difficult to extrapolate fluxes at a certain height down to the surface (Mahrt, 1998). The variance methods are based on flux-variance relationships derived on the basis of similarity arguments and established through the determination of the constant parameters in the derived relationship. Such relations have been established and verified extensively through experiments in the surface layer and it now appears possible to derive surface fluxes with sufficient accuracy (e.g., Tillman, 1972; Mahrt and Paumier, 1985; Wesely, 1988). Extending studies for surface layer had been conducted for non-uniform terrain (Katul et al., 1995), comparison of different land type (Padro, 1993; Lloyd et al., 1991), roughness sublayer (Katul et al., 1996), and stable conditions (De Bruin and Hartogensis, 2005).

In contrast, for the mixed layer, the relevant flux-variance relationships are still not fully understood and far from established. Up to now the proposed functional relationships between the variances in the mixed layer and the corresponding surface fluxes are still limited in number and they have been insufficiently validated. In addition, they were used mainly for the purpose of organizing derived variances in terms of similarity functions, and only a few studies have tried to apply such relations for the flux estimation. Sugita and Kawakubo (2003) used the variances of temperature in the lower half of the mixed layer obtained from tower observations to derive the surface sensible heat fluxes. There are limited studies using aircraft data, namely the one by Asanuma (1996), who used surface and mixed layer variance relations with temperature and humidity data obtained during HAPEX-Mobilhy (Hydrologic-Atmospheric Pilot Experiment and Modélisation du Bilan Hydrique) in southwestern France (André et al., 1986) to derive the corresponding surface fluxes.

1-2 Objective of This Study

In view of the lack of studies of the mixed layer variance relationships in general and their application for the surface flux estimation with aircraft data in particular, the present study was

initiated with data sets obtained from an aircraft above an extensive steppe region in Mongolia with simultaneous surface flux observations, in order to investigate the mixed layer variance relationships and the feasibility to use them for the purpose of estimations of a regional surface flux.

The rest of the paper is organized as follows. Chapter 2 describes the methodology and related data. In chapter 3, the mixed layer variance formulations proposed by previous studies are presented and compared to our observation. Using these formulations, the mixed layer variance methods are investigated in chapter 4. Discussion on the remaining problems in this study and the universality of these variance formulations is provided in chapter 5. Finally, chapter 6 summarizes the findings and offers some suggestions for the similarity approach in the mixed layer.

2 Methods

2-1 Study Area

The temperature turbulence data in the mixed layer were obtained by aircraft observations carried out from June through October of 2003 as part of the field campaigns of the Rangelands Atmosphere-Hydrosphere-Biosphere Interaction Study Experiment in Northeastern Asia (RAISE, Sugita et al., 2006). The RAISE study area covers the Kherlen river basin in the northeastern part of Mongolia, where arid to semi-arid climate is dominant with a boreal forest in the northern and upper reaches of the watershed and steppe area towards the southern and downstream parts. The location of RAISE area is shown in Fig. 2-1, and the topography and vegetation distribution are illustrated in Figs. 2-2 and 2-3, respectively.

In this study, the data used for the analysis were taken above an extensive steppe region, where a flux observation station was operated as described below. The target area was located at and around a village called Kherlen Bayan-Ulaan (47° 13′ N, 108° 44′ E, 1235m ASL, to be referred to as KBU hereafter); annual average air temperature is 1.2°C and annual precipitation is 196 mm in average from 1993 to 2002 (KBU weather station) and its climate is classified to semiarid (UNEP, 1997). Its surface vegetation is comprised mainly of the cool-season C_3 species and a few C_4 species (Li et al., 2005) with their height around 20 cm and leaf area index 0.5 at most, even at the peak growing season mainly because of the extensive grazing activities in this area (Sugita et al., 2006). The site was on a relatively flat terrace with horizontal extent of the order of 10^1 km along the Kherlen river. Figure 2-4 shows the ASTER true colour image with elevation data as part of ASTER 3D dataset (Abrams, 2000) around the KBU station with aircraft flight segments (see below). Figure 2-5 presents the seasonal change of landscape in this area.

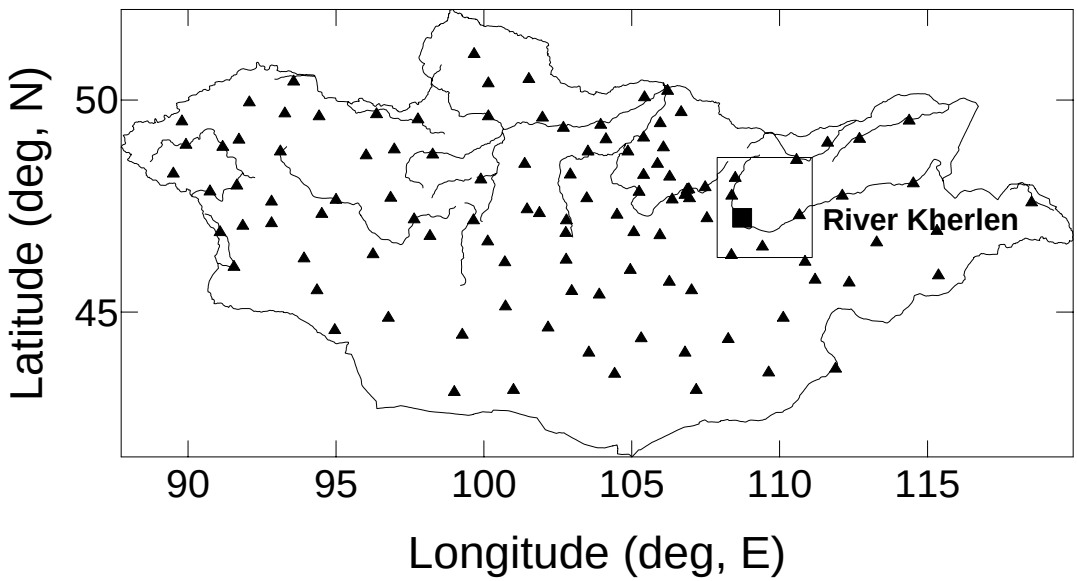

Fig. 2-1 Location of the study area.
Triangles show the meteorological stations of Institute of Meteorology and Hydrology of Mongolia and solid square shows the KBU flux station. Lines show national boundary and major rivers in Mongolia. The closed area is the range of Figs. 2-2 and 2-3.

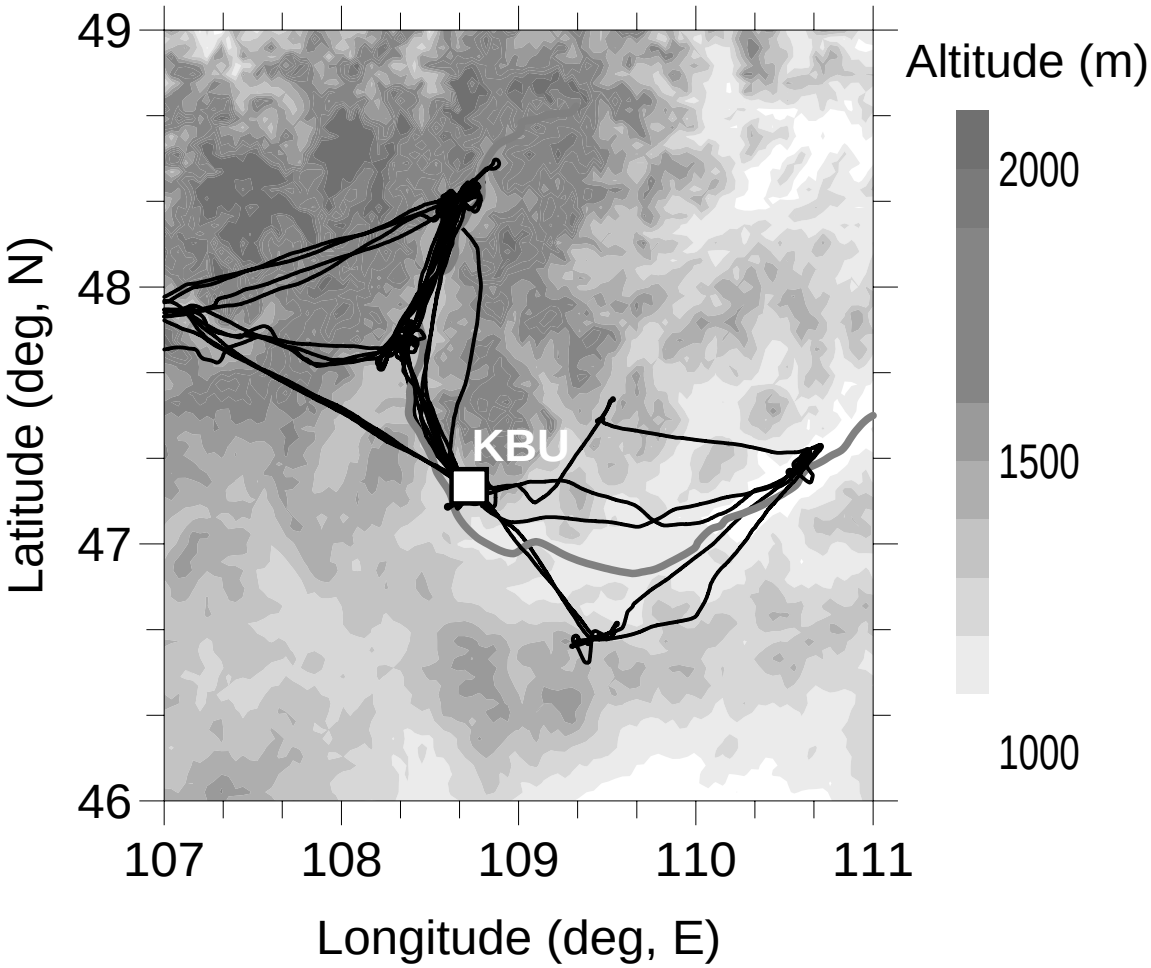

Fig. 2-2 Topographic map of the study area based on GTOPO30 dataset with the flight paths.

Black and gray lines show aircraft flight path (of all flight) and River Kherlen, respectively. GTOPO30 is DEM data provided by USGS (http://edc.usgs.gov/products/elevation/ gtopo30.html).

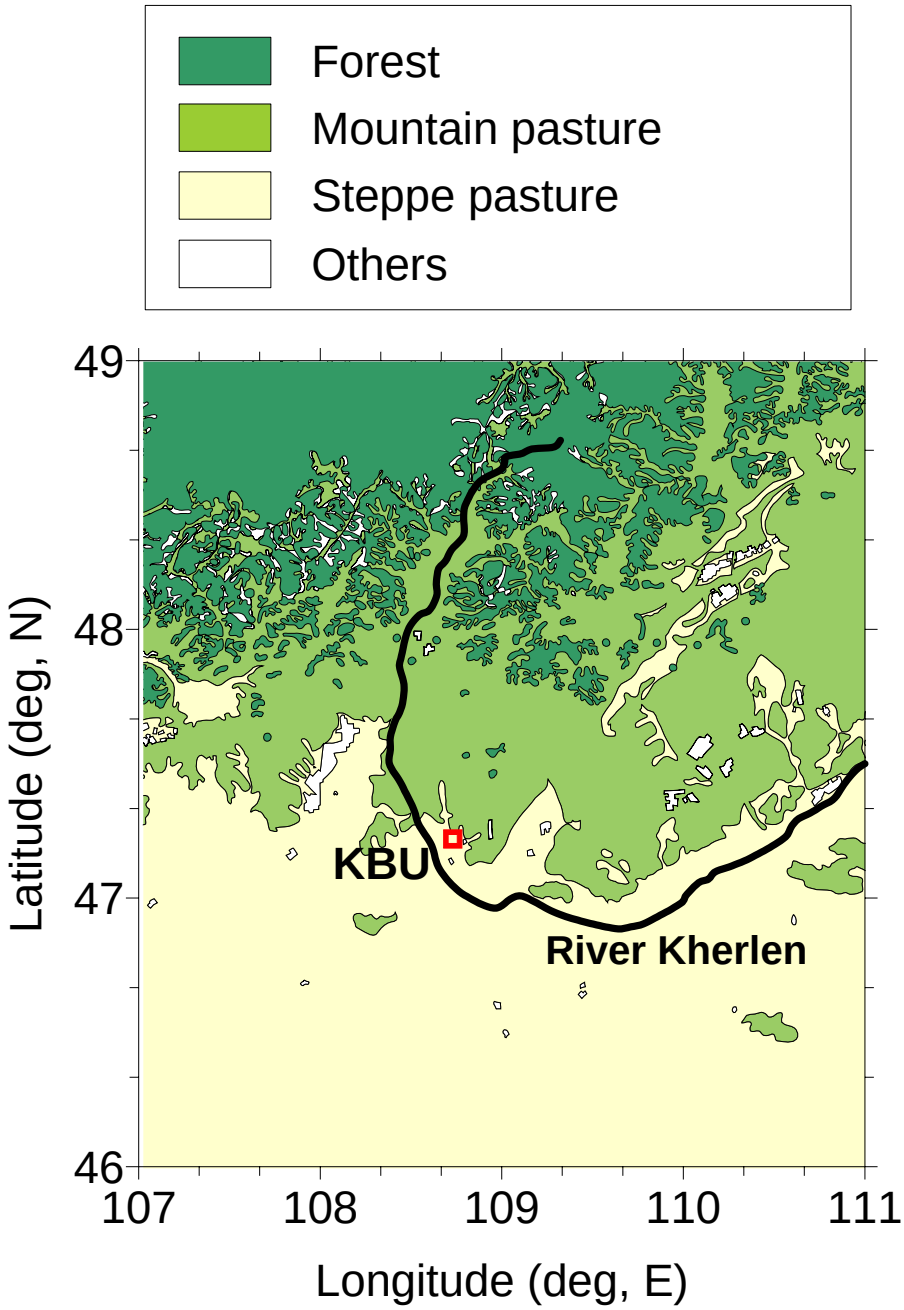

Fig. 2-3 Vegetation distribution in the study area based on Saandar and Sugita (2004).

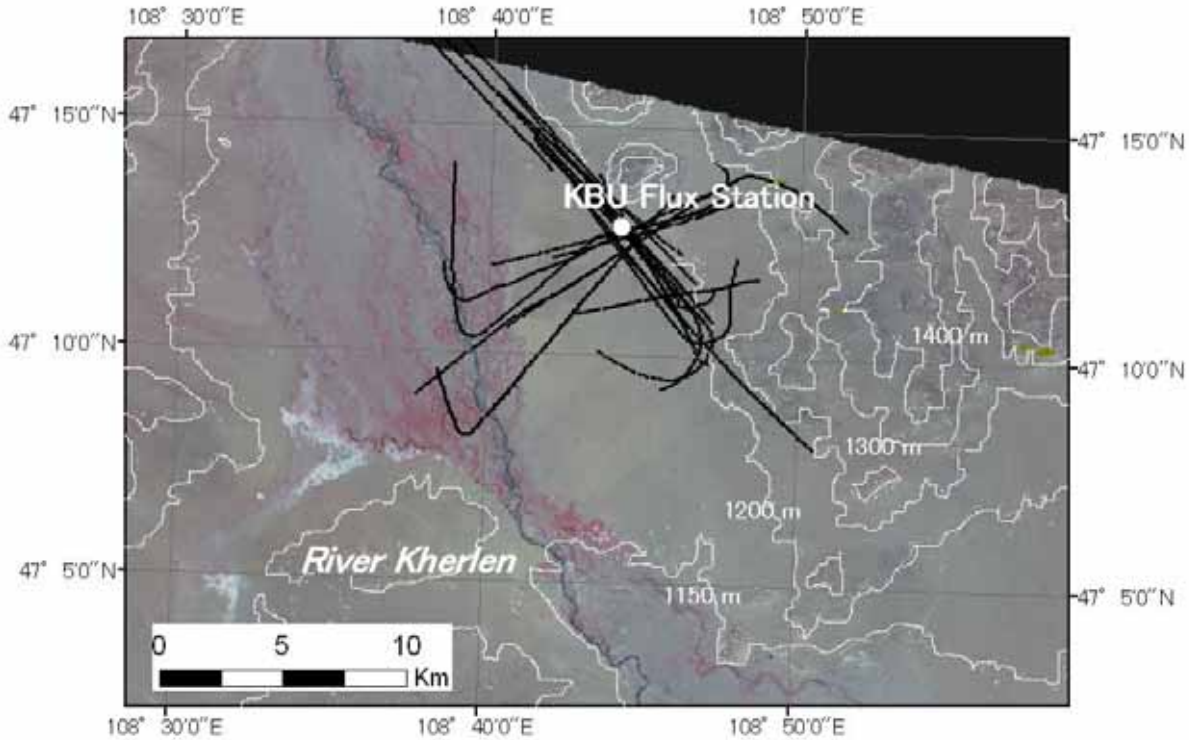

Fig. 2-4 Topographic map with ASTER true color image of the KBU area with all the flight segments.

Contour lines are shown at 50m interval. This image was taken at May 29, 2001 and shade area is out of the image.

a)

b)

Fig. 2-5 Photographs of the landscape around the KBU flux station.
a) August 1, 2003, b) October 7, 2003

2-2 Aircraft Observations

The instruments were installed on a wing of an aircraft (AN2), a single engine biplane, to measure the air temperature with a fine thermocouple whose time constant is rated as 0.4 s. The data were continuously sampled at 10 Hz during the flight by a data logger (CR23X, Campbell Scientific Inc.). Positioning information was simultaneously obtained by a GPS receiver at 0.5 Hz and by a gyroscope that measured the angular velocity of the aircraft in the directions of its main body and the wing at a 10 Hz intervals. Other measurements from the aircraft but not directly used in the present study, included the relative humidity by a Krypton hygrometer (KH-20, Campbell Scientific Inc.), the surface infrared temperature, incoming and outgoing shortwave radiation, and the spectral reflectance of the underlying surfaces in the range of 350-2500 nm. This measurement system is summed in Table 2-1 and pictured in Figs. 2-6 and 2-7.

As mentioned, the flight paths covered the KBU station and the surrounding area (Fig. 2-4) and flight levels of around 200, 500 and 1000m above the ground were flown repeatedly above this site. Although the lengths of the actual flight segments flown above the KBU area were slightly different one from another, depending on the weather condition and on the flight direction, only those flight segments longer than 5 km, which is equivalent to the averaging time of 100 s, and those whose standard deviation of the flight level was smaller than 50 m, were selected for analysis. Also, the data obtained in the June observations were found not to be usable for the present purpose because of data acquisition problems. This selection procedure produced 25 flight segments and data sets for the following analysis (Table 2-2). To check the general reliability of the turbulence data, and also to check the scale of the turbulence observed, a Fourier transformation was applied to the measured time series listed in Table 2-2. The resulting power spectra, weighted by frequency, are shown in Fig. 2-8. The spectral peak frequency was found at around f_p = 0.01 Hz, and this corresponds to the length scale of 3 km, approximately, as the ground speed of the AN2 was around 30 m s^{-1}. Although the peak frequency and the general shape of the power spectra follow those reported in the literature (e.g., Kaimal and Finnigan, 1994), spectra attenuation can be observed in the inertial subrange at 0.1-1.0 Hz, as the slope is steeper than the commonly accepted value of -2/3. This might be

Table 2-1 Instruments for the observation aboard aircraft.

(1) Measurement Instruments

Component	Instrument	Model / Manufacturer (location)	Notes
Air temperature	Thermocouple (Copper-Constantan) with protection shield	A02-0104 / Climatec Inc. (Tokyo, Japan)	time constant = 0.4s
Absolute humidity	Krypton hygrometer	KH20 / Campbel Scientific Inc. (Logan, U.S.)	
Relative humidity / Air temperature	Capacitance hygrometer Platinum resistance thermometer	50Y / Vaisala Oy. (Helsinki, Finland)	
Surface temperature	Infrared thermometer	505 / Konica Minolta Holdings,Inc. (Tokyo, Japan)	8-14μm
Shortwave radiation	Pyranometer	RS-5 / Ishikawa Trading Co., Ltd (Tokyo, Japan)	

(2) Peripheral Device

Component	Instrument	Model / Manufacturer (location)	Notes
Data sampling and logging	Data logger	CR23X / Campbel Scientific Inc. (Logan, U.S.)	
Data storage	Storage module (extended memory)	SM16M / Campbel Scientific Inc. (Logan, U.S.)	16MB
Power source	Lead acid battery	Yuasa NP7-6 / Yuasa Co. Ltd. (Osaka,Japan)	inside datalogger
Positioning information	GPS receiver	GP-31 / Furuno Electric Co., Ltd. (Nishinomiya, Japan)	

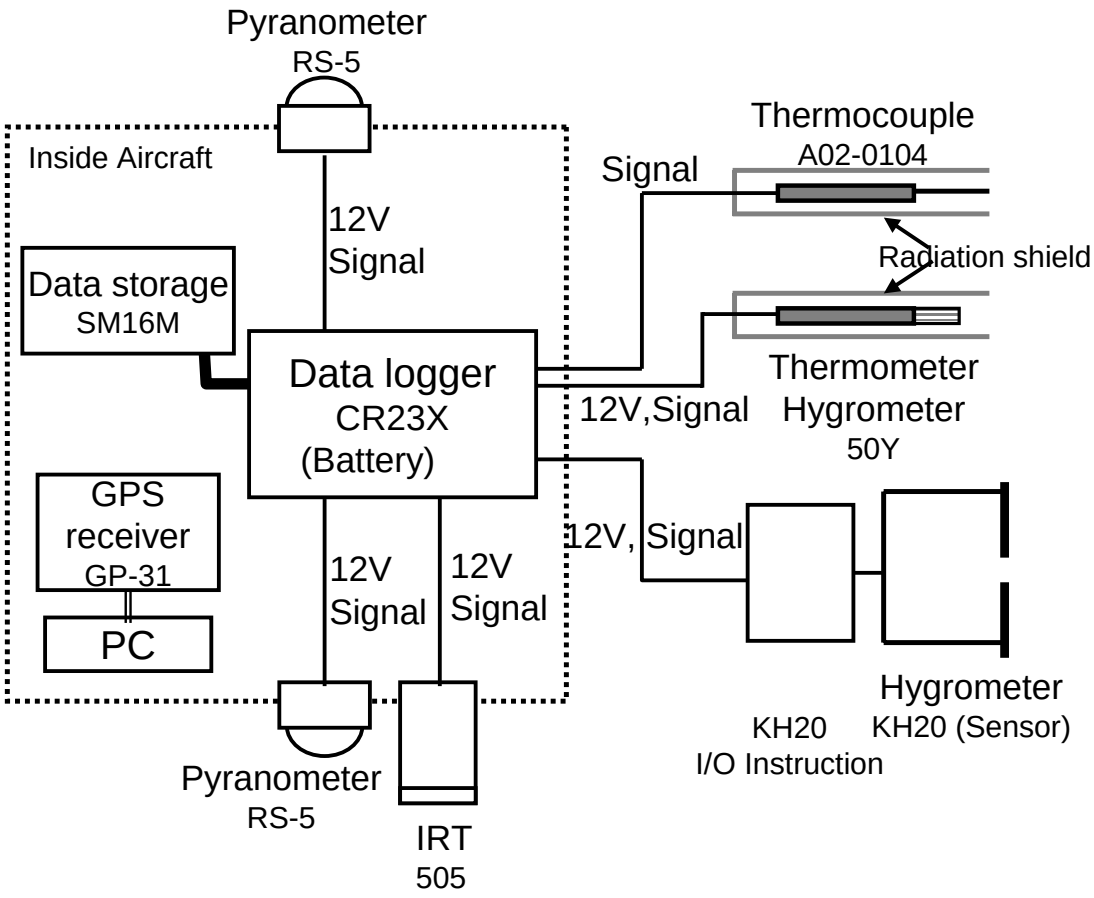

Fig. 2-6 Schematic diagram of the observation system aboard aircraft.
(power supply and measurement system)

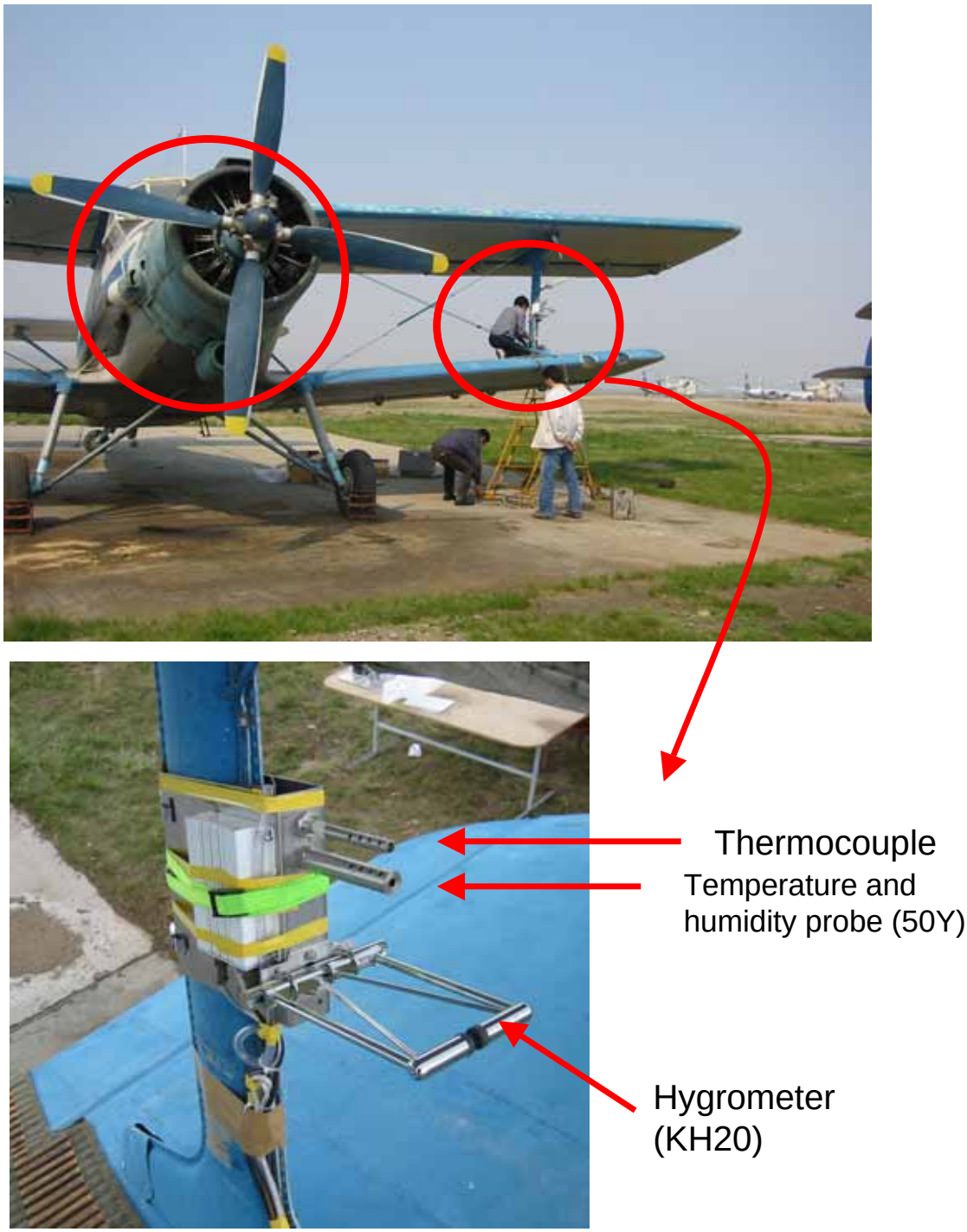

Fig. 2-7 Photographs of the observation system aboard aircraft.

Table 2-2 Flight segments information above the KBU area.

Date (2003)	Segment name	Time (MST) (HHMM)	Segment length (km)	z (m)	h_i (m)	z / h_i	H_s (W m^{-2})	T_* (K)	w_* (m s^{-1})	U (m s^{-1})	WD (deg)	weather condition
July 19	200-KBU500	1541	9.31	437	900	0.49	139	0.088	1.6	7.2	265	clear
	200-KBU200	1549	8.80	180		0.20	139	0.088	1.6	7.2	265	
July 20	201-KBU200	1036	7.48	194	700	0.28	77	0.063	1.2	1.8	315	clear /cloudy
	201-KBU500a	1045	7.23	532		0.76	77	0.063	1.2	1.8	316	
	201-KBU500b	1053	7.84	523		0.75	77	0.063	1.2	1.7	316	
July 23	204-KBU1000	1236	11.21	914	900	1.02	123	0.085	1.6	6.6	85	clear
	204-KBU200	1254	10.13	187		0.21	123	0.085	1.6	6.5	85	
Aug. 21	233-KBU200a	1227	9.50	224	770	0.29	82	0.062	1.3	6.1	328	clear /cloudy
	233-KBU200b	1234	10.03	206		0.27	97	0.069	1.3	6.2	328	
	233-KBU300	1241	7.52	384		0.50	116	0.078	1.4	6.2	327	
Aug. 22	234-KBU1000	1233	7.68	1062	1075	0.99	134	0.078	1.6	3.1	24	generally clear
	234-KBU500b	1251	7.89	556		0.52	142	0.081	1.7	3.1	35	
	234-KBU200	1256	8.19	271		0.25	144	0.082	1.7	3.1	38	
Aug. 23	235-KBU1000	1225	7.56	1123	1200	0.94	148	0.080	1.8	1.7	16	generally clear
	235-KBU500a	1231	11.73	577		0.48	147	0.079	1.8	1.5	17	
	235-KBU500b	1239	11.98	599		0.50	148	0.080	1.8	1.2	18	
	235-KBU200	1253	5.24	260		0.22	150	0.080	1.8	0.7	22	

Table 2-2 (continued)

Date (2003)	Segment name	Time (MST) (HHMM)	Segment length (km)	z (m)	h_i (m)	z / h_i	H_s (W m^{-2})	T_* (K)	w_* (m s^{-1})	U (m s^{-1})	WD (deg)	weather condition
Oct. 2	276-KBU1000	1245	11.59	1113	1600	0.70	189	0.080	2.1	8.2	3	generally clear
	276-KBU500a	1255	11.01	662		0.41	194	0.081	2.1	8.1	3	
	276-KBU500c	1304	11.50	640		0.40	198	0.083	2.1	8.1	2	
Oct. 3	277-KBU1000	1255	19.87	1072	1300	0.82	184	0.085	1.9	2.5	302	generally clear
	277-KBU500a	1307	7.24	568		0.44	176	0.083	1.9	2.4	304	
	277-KBU500b	1309	12.66	639		0.49	176	0.083	1.9	2.4	305	
	277-KBU500c	1318	11.12	618		0.48	175	0.083	1.9	2.3	307	
	277-KBU200	1323	8.93	381		0.29	174	0.082	1.9	2.3	309	

MST: Mongolian Summer Time (= local solar time + 2 hours), z: flight height (m), h_i: mixed layer height (m), H_s: sensible heat flux observed at the KBU station (W m^{-2}), T_*: mixed layer temperature scale (K), w_*: mixed layer velocity scale (m s^{-1}), U: wind velocity (m s^{-1}), WD: wind direction (degree, 0º = northern wind), U and WD are the output of TERC-RAMS, at 800hPa (inside the CBL)

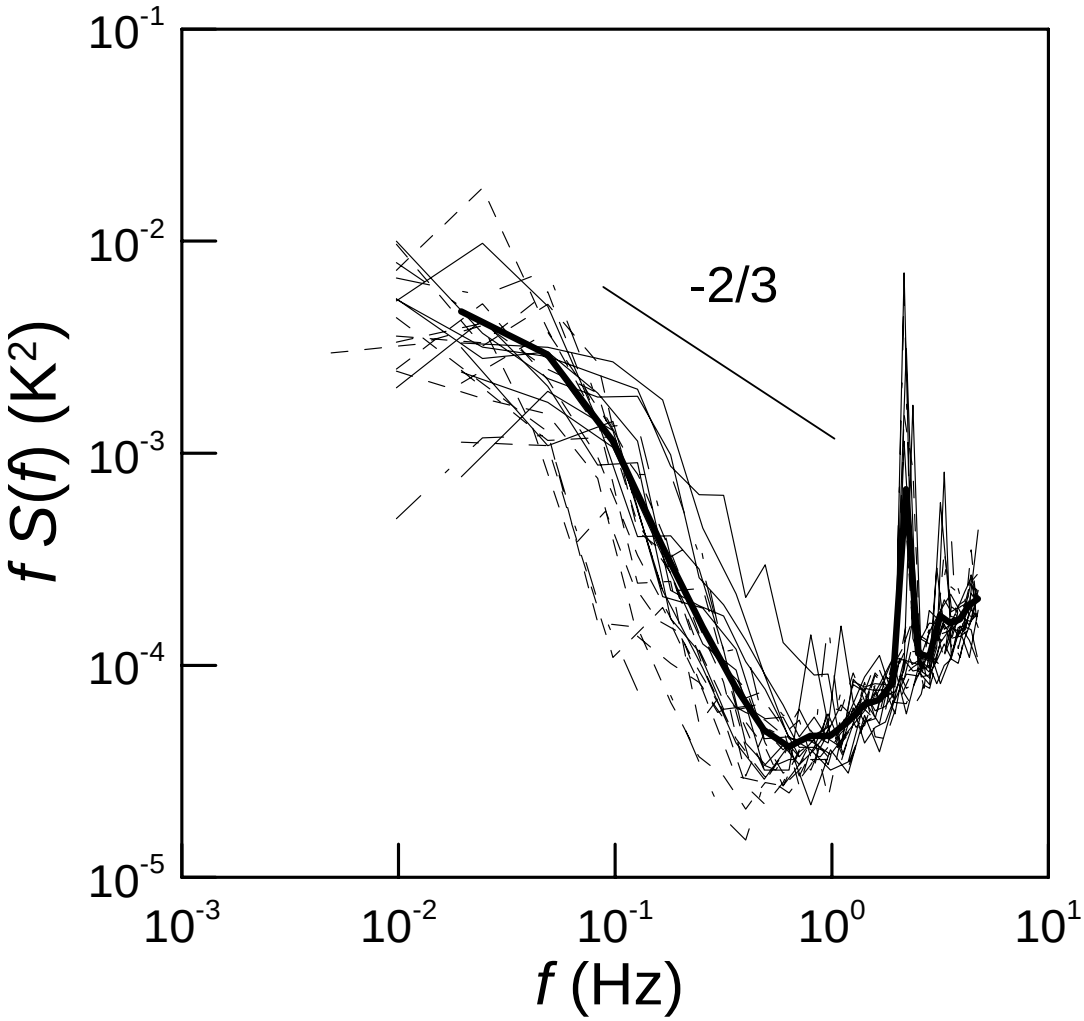

Fig. 2-8 Power spectra *fS* for temperature fluctuation as a function of cyclic frequency *f*.

due to the fact that the time constant of the temperature probe was not sufficiently small. Also, the power spectra exhibit a white noise in the higher frequency range above 1 Hz. A probable error in the evaluated variance due to this attenuation and to the white noise was estimated by evaluating the difference between the actual spectra curves and a hypothetical curve obtained by assuming the slope of -2/3 in the frequency range above f_p and of 1/1 below f_p. It was found that the difference due to the attenuation and to the white noise constitutes is 8% underestimation and 3% overestimation, respectively, of the total variance for all the segments average. In chapter 4, the influence of these under- or overestimations of temperature variance to the flux estimation with variance formulations will be investigated in detail.

For each flight segment, the data were first visually checked by plotting them as time series. They were then further processed to remove a trend before the analysis by applying a linear regression method (Kaimal and Finnigan, 1994); in brief, a linear equation $y = ax + b$ was fitted to the measured temperature time series, and all data were corrected by subtracting $y - \overline{y}$ where $\overline{y}$ is the mean over the flight segment (Fig. 2-9). In most cases, the correction was very small with the coefficient a in the range of -5×10^{-4} to 5×10^{-4} (K / 0.1s).

The scale of the upwind surface source distribution of the observed temperature variances was evaluated with the expression for scalar fluxes of Weil and Horst (1992), which was derived based on a CBL Lagrangian stochastic dispersion model. For an assumed mean wind speed U = 10 m s^{-1}, a CBL height h_i = 1000 m, and a typical mixed layer velocity scale (see below) w_* = 1.5 m s^{-1}, this scale was found to be 0.6 km, 4.4 km, and 6.7 km, respectively for measurement heights of z = 200, 500, and 1000 m.

2-3 Ground Based Observations

During the aircraft observations, the flux station at KBU site was in continuous operation. The details of the flux station have been presented in Li et al. (2005) and Sugita et al. (2006), and the measurement components and outline of the system are shown in Table 2-3 and Figs. 2-10 and 2-11. For the purpose of the present study, however, use was made of the air temperature and wind velocity components measured at 10 Hz, and the surface flux of the sensible heat H and the

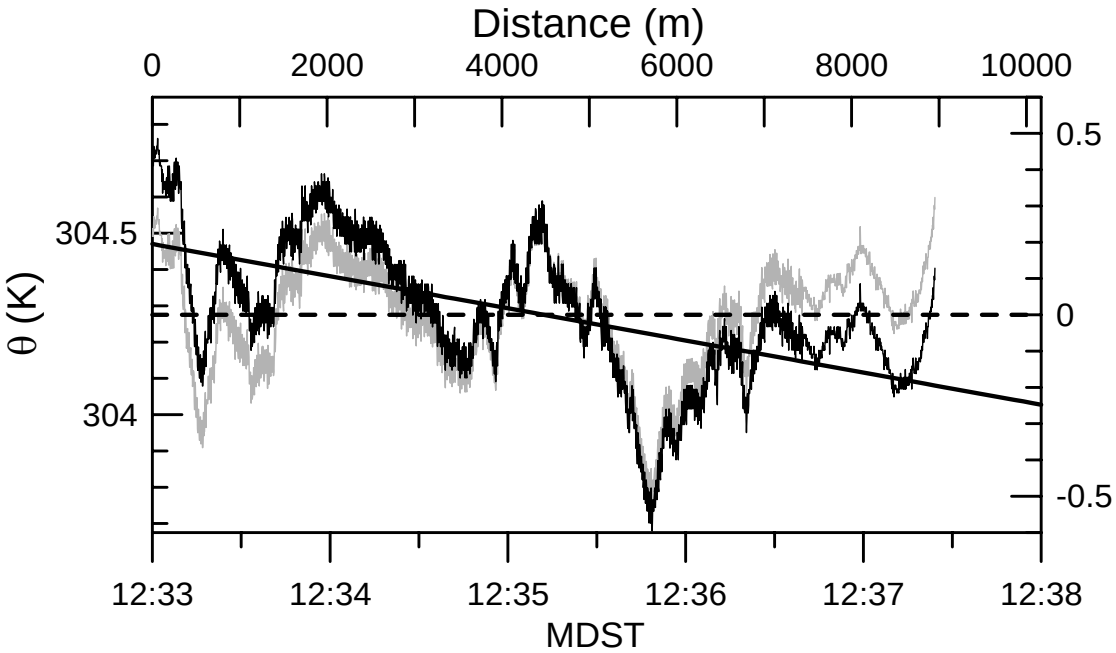

Fig. 2-9 Trend removal procedure applied to temperature time series. Black and gray fluctuation lines are measured and trend removed time series, and solid and broken straight lines are fitted line $y=ax+b$ and segment average y, respectively. MDST means Mongolian Daytime Saving Time.

Table 2-3 Instruments for the observation at the KBU flux station.

Component	Instrument	Model / Manufacturer (location)	Height / depth
Relative humidity / Air temperature	Capacitance hygrometer	HMP45A / Vaisala Oy. (Helsinki, Finland)	2.5 m
	Platinum resistance thermometer in ventilation shelter	PVC-02-AC / Prede Co. Ltd. (Tokyo, Japan)	
Surface temperature	Infrared thermometer	303F / Konica Minolta Holdings, Inc. (Tokyo, Japan)	2.5 m
Sensible / latent heat flux	Sonic aemometer-thermometer	SAT540/ Kaijo Sonic Co. (Tokyo, Japan)	3.0 m
	CO_2/H_2O Infrared gas analyser	Li7500 / Li-cor Inc. (Lincoln, U.S.)	
Short-wave radiation	Pyranometers*1	CM3 / Kipp and Zonen B.V. (Delft, Netherlands)	2.5 m
Long-wave radiation	Pygrometers*1	CG3 / Kipp and Zonen B.V. (Delft, Netherlands	2.5 m
Air pressure	Barometer	PTB210 / Vaisala Oy. (Helsinki, Finland)	1.3 m
Precipitation	Tipping bucket rain gauge	52202 / R. M. Young Inc. (Traverse, U.S.)	
Soil heat flux	Heat flux plate	HFT1.1 / REBS*2 Inc. (Seattle, U.S.)	-0.02, -0.1m
Soil temperature	Platinum resistance thermometer	C-PTG / Climatec Inc. (Tokyo, Japan)	-0.05, -0.1, -0.2, -0.3, -0.5, -0.7, -1.0, -1.5m
Volumetric water content	TDR*3 sensor	CS616 / Cambel Scientific Inc. (Logan, U.S.)	-0.1, -0.2, -0.3, -0.7, -1.0, -1.5m

*1: Included in Net-radiometer (CNR1, Kipp and Zonen, B.V.)

*2: Radiation and Energy Balance Systems

*3: Time Domain Reflectometry

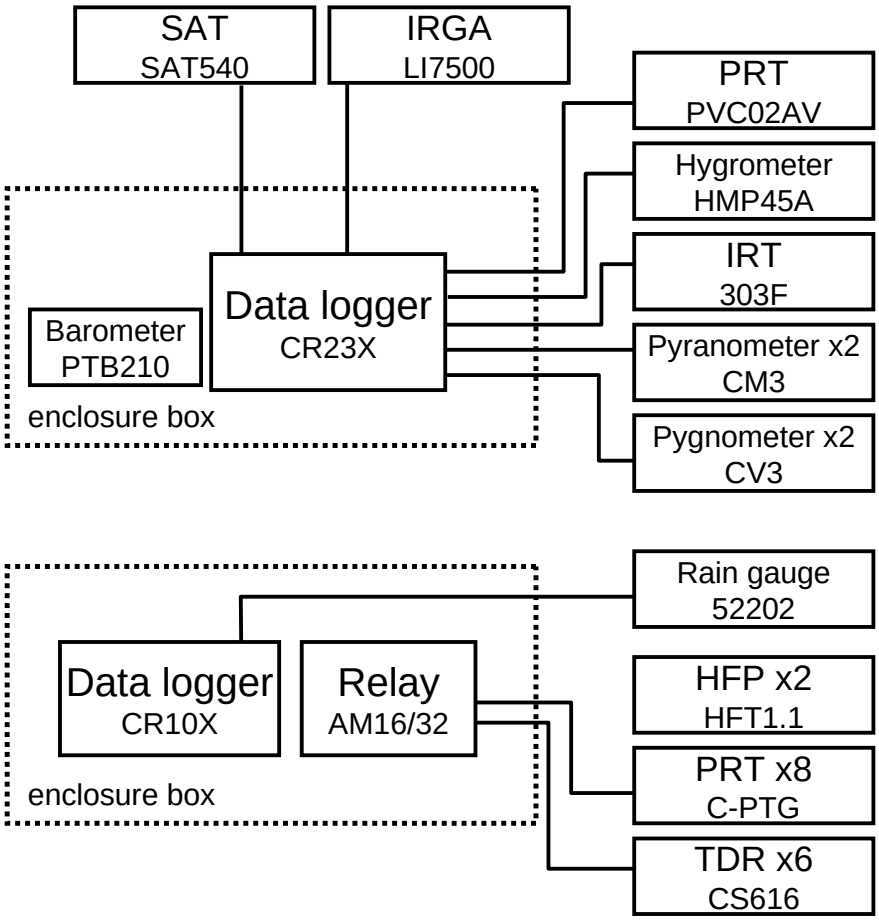

Fig. 2-10 Schematic diagram of the observation system of the KBU flux station.

(measurement system only) SAT: sonic anemometer-thermometer, IRGA: infrared gas analyzer, PRT: platinum resistance thermometer, IRT infrared thermometer, HFP: heat flux plate, TDR: time domain reflectmetry

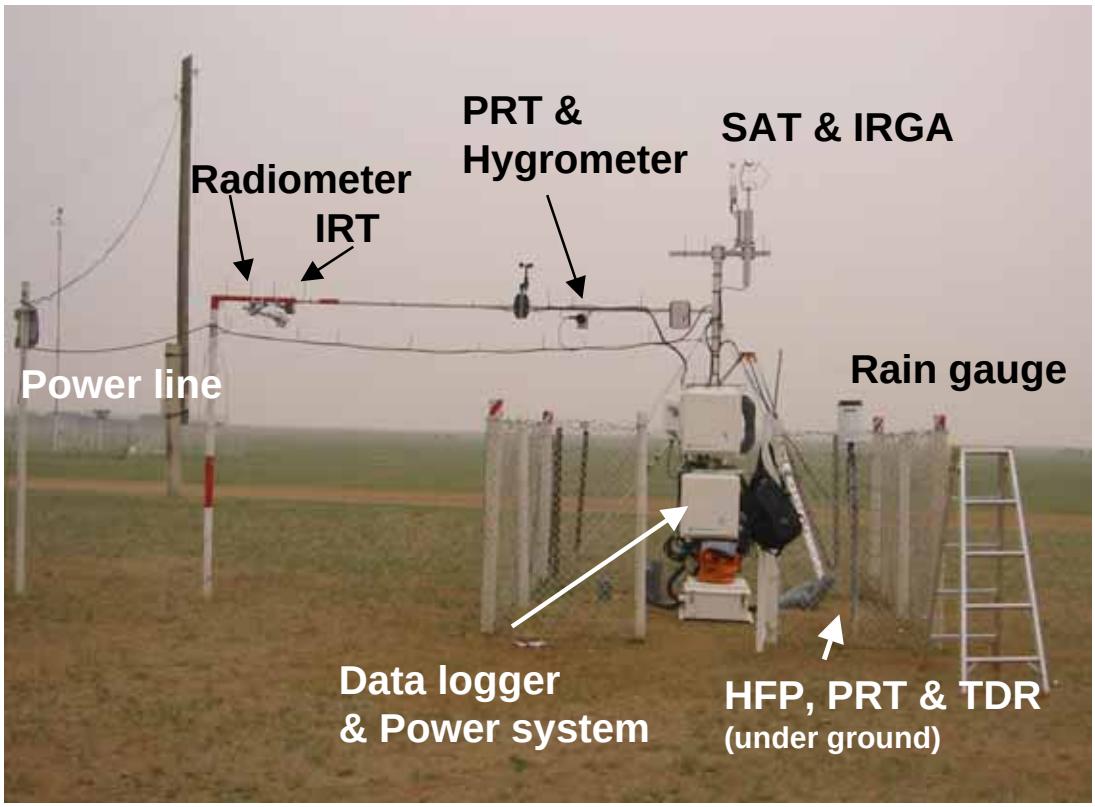

Fig. 2-11 Photograph of the observation system of the KBU flux station. SAT: sonic anemometer-thermometer, IRGA: infrared gas analyzer, PRT: platinum resistance thermometer, IRT infrared thermometer, HFP: heat flux plate, TDR: time domain reflectmetry

latent heat *LE* calculated by the eddy covariance method for 30 minutes. Since the sums of *H* and *LE* were found to exhibit on energy imbalance in comparison with the net radiation R_n and soil heat flux *G*, the energy shortage was distributed into the turbulence energy fluxes of *H* and *LE* by keeping the Bowen ratio as suggested by Twine et al. (2000). During the flight times, the average energy-balance closure, $(H+LE)/(R_n+G)$ was 0.67, and the corrected *H* values ranged from 80 to 200 Wm^{-2}. These corrected values were used as the reference surface fluxes,

2-4 Large Scale Atmospheric Data

The outputs of a regional climate model (TERC- RAMS, Sato and Kimura, 2005) were used to evaluate the mesoscale influence on the mixed layer variances through baroclinicity and advection (see below). The 6-hourly NCEP/ NCAR reanalysis data set, which was produced for 2003 by essentially the same method described in Kalnay et al. (1996), was used as the model forcing data to produce the downscaled (in time and space) data set that includes the area and the intensive observation periods of the RAISE project (Sato et al., 2006). This downscaled data set has a horizontal resolution of 30 km and a time interval of one hour.

However, in this procedure, the atmospheric field within one grid of the 2.5° × 2.5° reanalysis data set is simulated by the model without the inputs from observations and thus it is possible that a slight different in the cloud formation or in the course of fronts and low pressure system could result in vastly different atmospheric and surface condition at short time intervals. For this reason, it is not appropriate to use instantaneous values of these products at specific time and space. Rather, they should be used as the time or space averages. For the baroclinicity evaluation, the area of the size of 450×450 km^2 was adopted for space averaging, which is rather smaller than synoptic scale features of the pressure and temperature field, considering the effects of mesoscale circulation. In contrast, for the evaluation of the local horizontal advection, the 16 grids around the KBU site that cover an area of about 120×120 km^2 were used, which scale was influenced by local topographic circulation. These averaging domains are illustrated in Fig. 2-12. Both of them were further averaged in time over six hours, namely from 9 to 15 in Mongolian Daylight Saving Time (MDST = UT -9 hours). Since aircraft observations were in

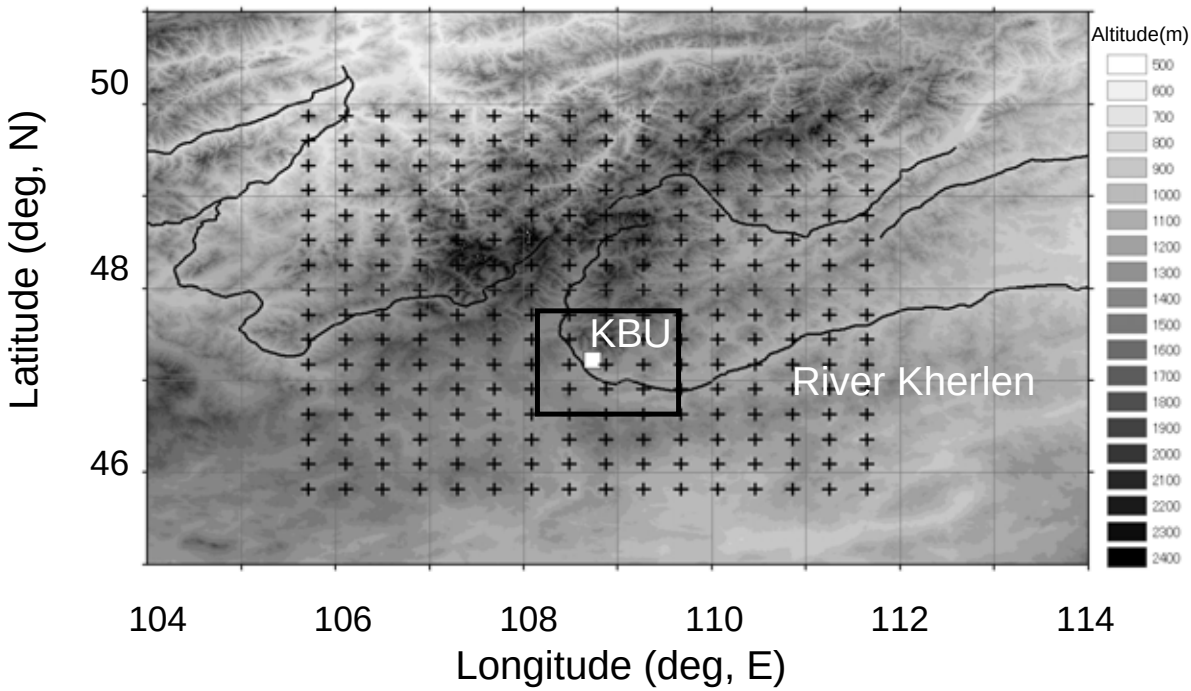

Fig. 2-12 Distribution of TERC-RAMS grid points.
16×16 grid points are used for evaluation of baroclinicity parameters, and 5×5 of closed area is for local advection evaluation. Topographic map is based on USGS/GTOPO30 dataset

general carried out in clear sky condition without atmospheric disturbance such as the passage of the atmospheric low system, the above averaging procedure should reduce or eliminate possible mismatch of the products with actual conditions.

3 Scalar Variance Relationships in the Mixed Layer

3-1 Vertical Structure of Scalar Admixture in the Observed Mixed Layer

The aircraft observations in July through October in Kherlen river basin provide the seasonal variation of mixed layer properties. Before investigating the scalar variance formulations in the mixed layer, the observation results are presented in this section. To see the vertical structure of the mixed layer, a height of the entire CBL, h_i, is required. The values of h_i were estimated by a method of Liu and Ohtaki (1997) and the procedure is described in Appendix A-1. It was found that h_i was around 700 – 1600 m during the flight observation periods (Table 2-2). Vertical profiles of daytime mixed layer were obtained, although there is no data near the upper boundary at h_i. Note, however, that the actual boundary layer top or entrainment layer varies in time and space (e.g., Hägeli et al., 2000), and the above method uses similarity argument and provide mean (in time and space) values.

Vertical distribution of segment-averaged potential temperature θ and specific humidity q of the air is shown in Figs. 3-1 and 3-2, and those plots with observation height z normalized with mixed layer height h_i ($\xi = zh_i^{-1}$) are shown in Figs. 3-3 and 3-4. It is noted that there is a subtle decrease of humidity with height in July and August data observed in daytime and reflects the evapotranspiration from soil or vegetated surface and entrainment of drier air from above (e.g., Mahrt, 1976). The Bowen ratio (ratio of sensible heat flux to latent heat flux) observed at the KBU station was varied in the range from 0.7 in August to 3.2 in October, which indicates generally dry condition, and therefore the vertical gradient of the humidity was not very clear especially in October.

Figures 3-5 and 3-6 show the vertical profile of temperature variance σ_θ^2 and correlation coefficients $r_{\theta q}$ between potential temperature θ and specific humidity q. In addition the same data with normalized height ξ are shown in Figs. 3-7 and 3-8. In the lower half of the mixed layer, positive correlation was observed and it indicates that source of temperature and humidity is the same at the surface. Large temperature variance near the surface also shows presence of

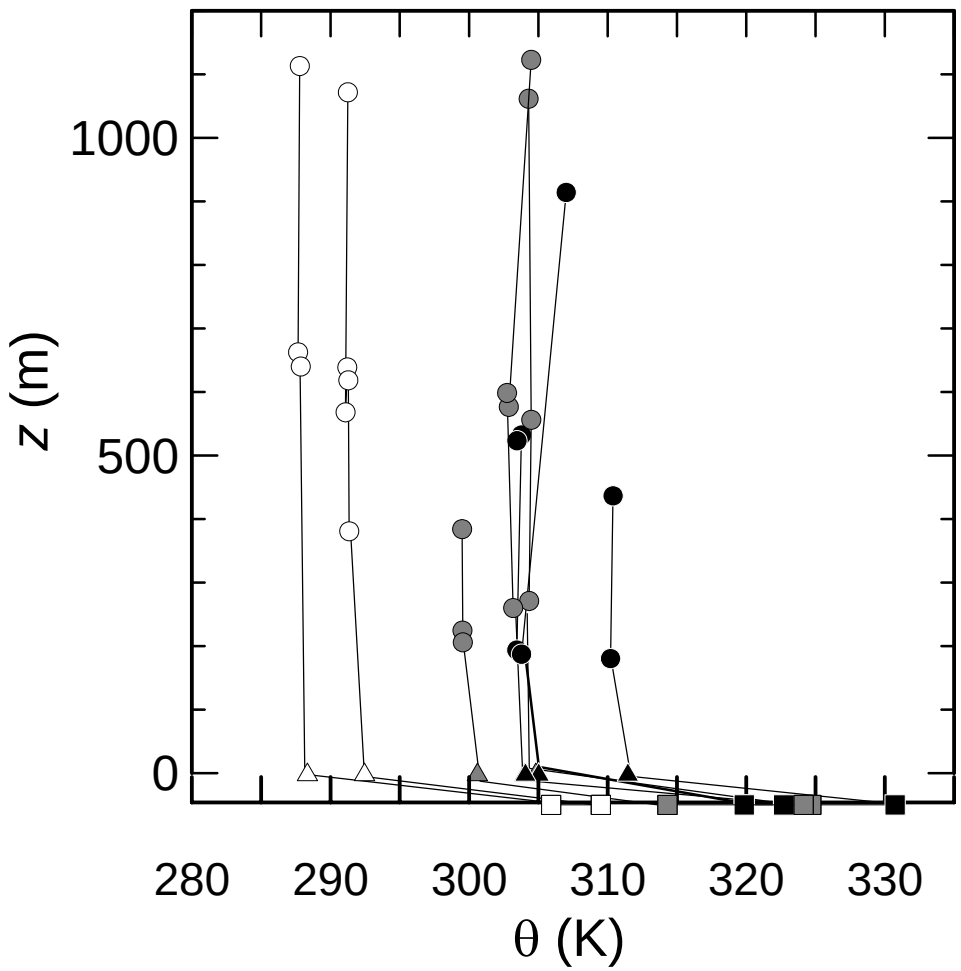

Fig. 3-1 Vertical profiles of mean potential temperature θ observed above the KBU area.

Solid, shaded and open symbols indicate the data for July, August and September, respectively, while circle and triangle symbols show aircraft and ground observation, respectively. Square symbols show surface radiative temperature.

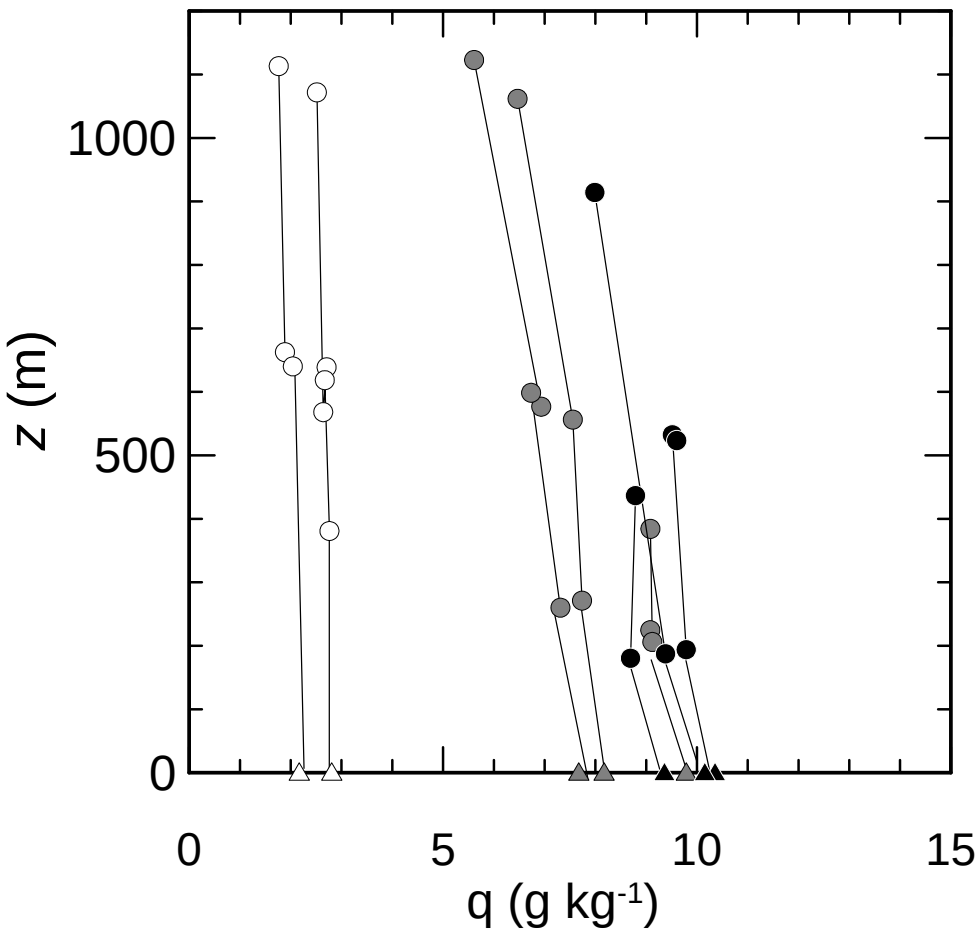

Fig. 3-2 Same as 3-1 but for mean specific humidity *q*.

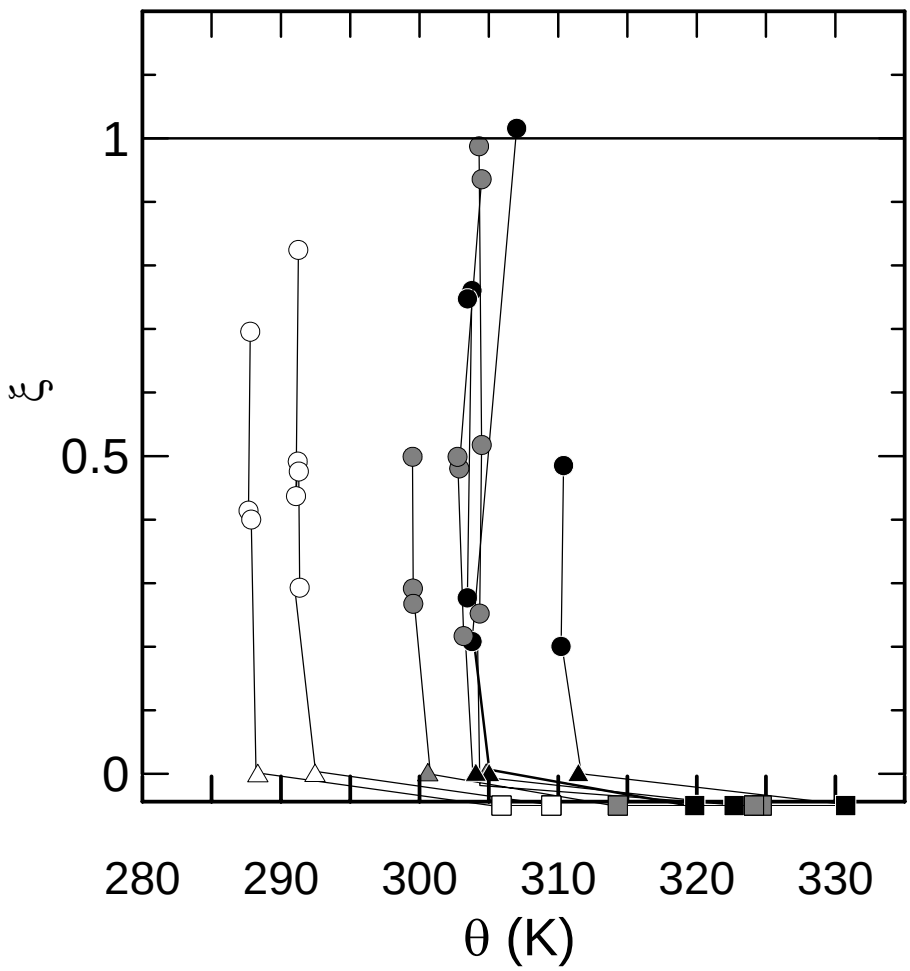

Fig. 3-3 Same as 3-1 but wth y-axis normalized height ξ.

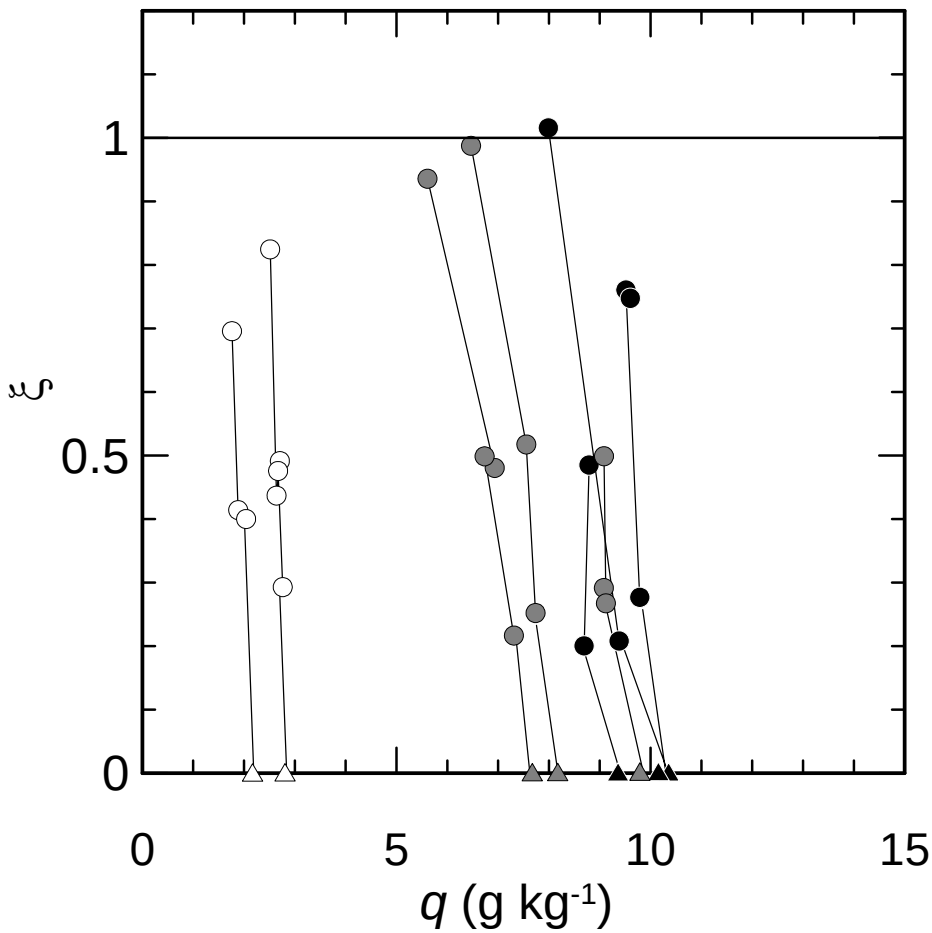

Fig. 3-4 Same as 3-1 but for mean specific humidity *q* and with y-axis normalized height ξ.

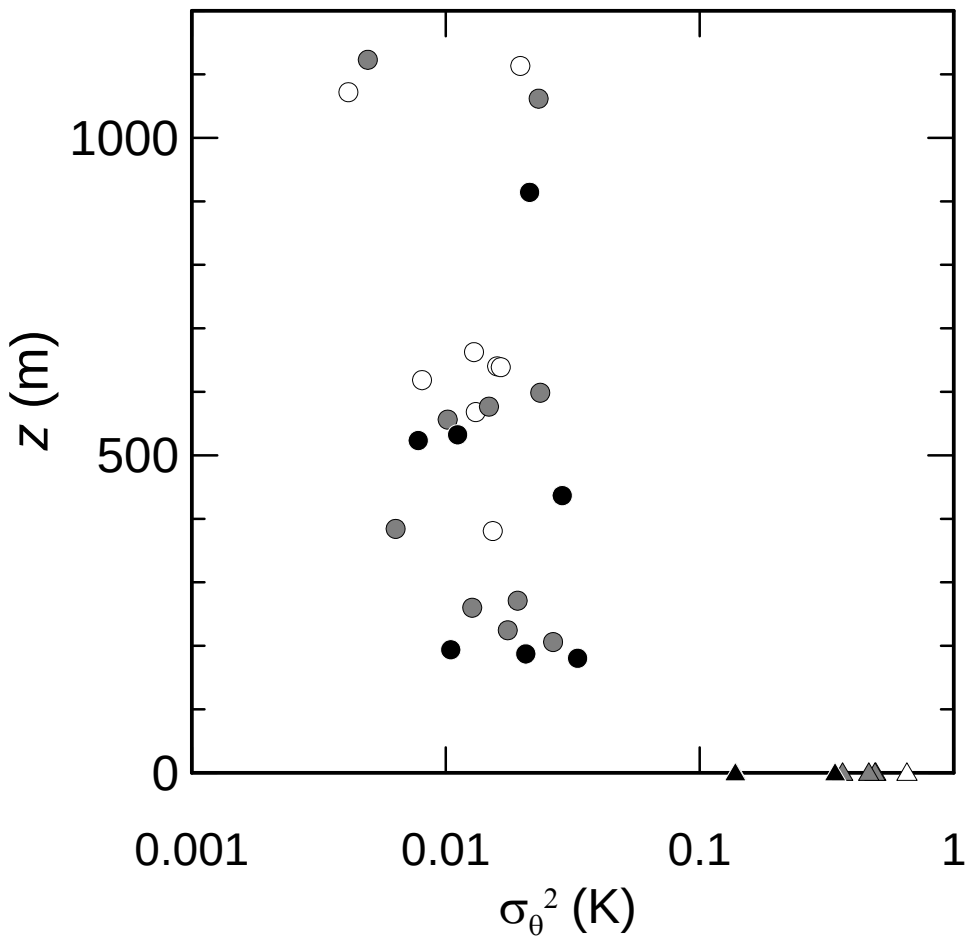

Fig. 3-5 Same as 3-1 but for variance of potential temperature σ_θ^2.

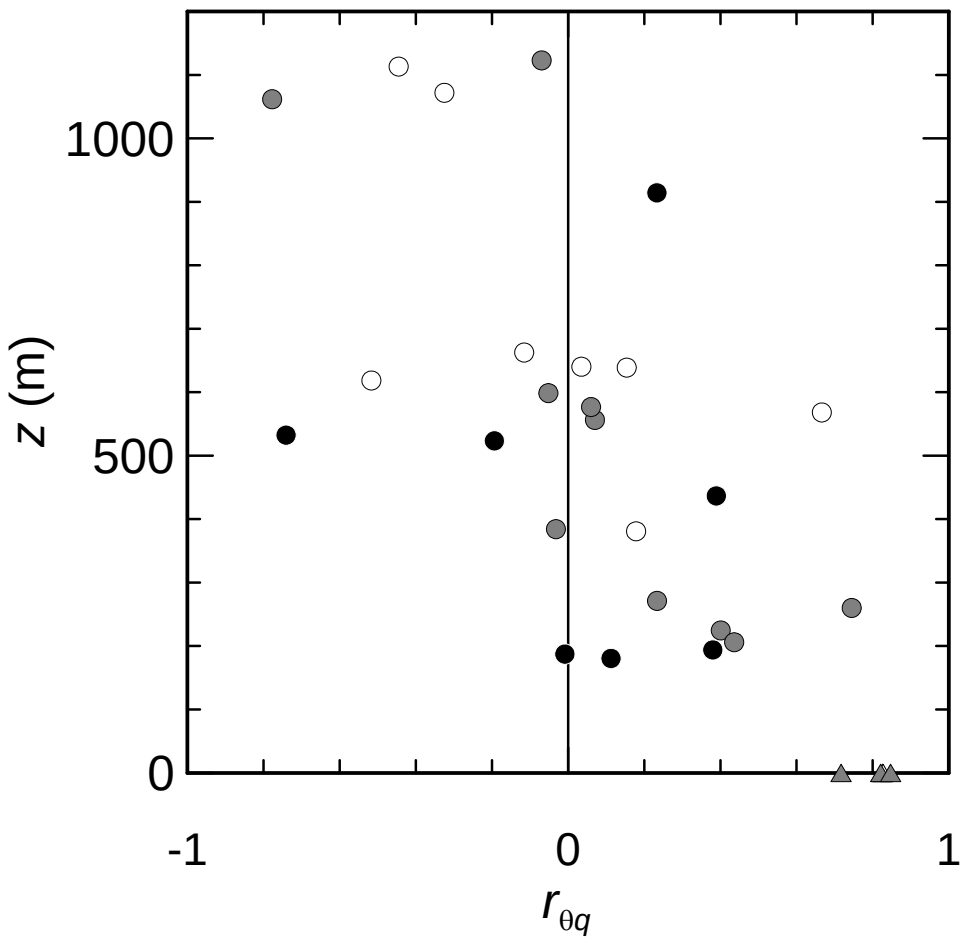

Fig. 3-6 Same as 3-1 but for correlation coefficient of potential temperature θ and specific humidity q.

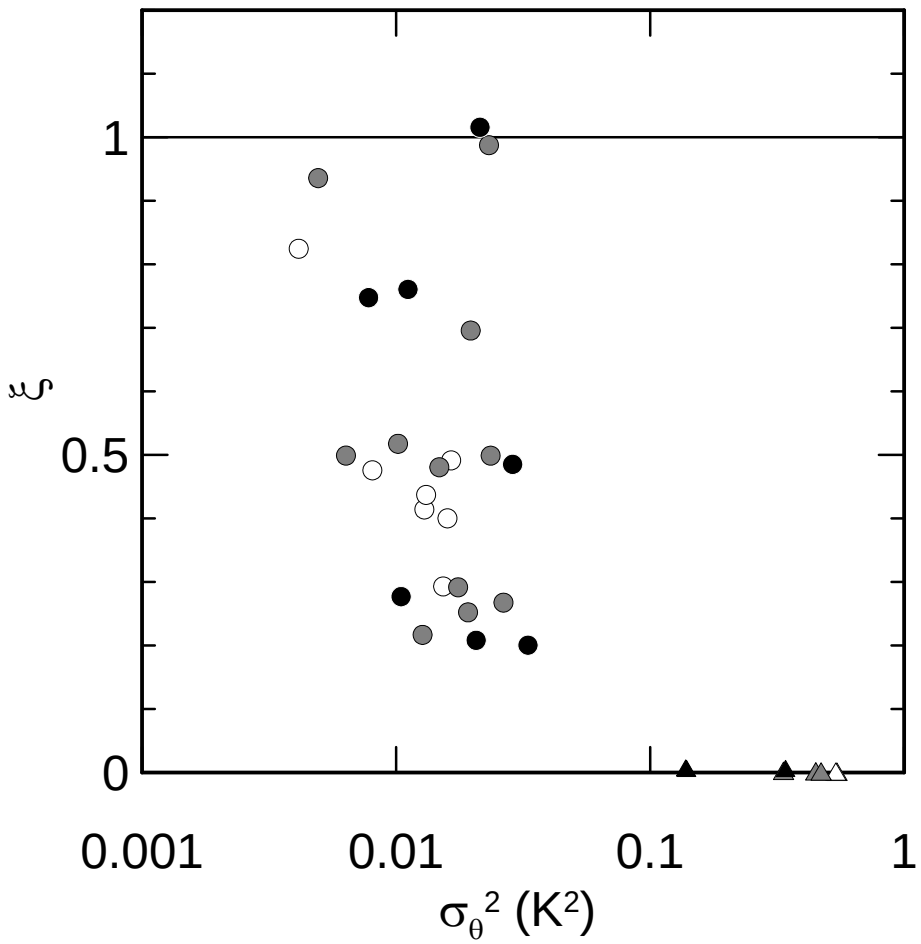

Fig. 3-7 Same as 3-5 but with y-axis normalized height ξ.

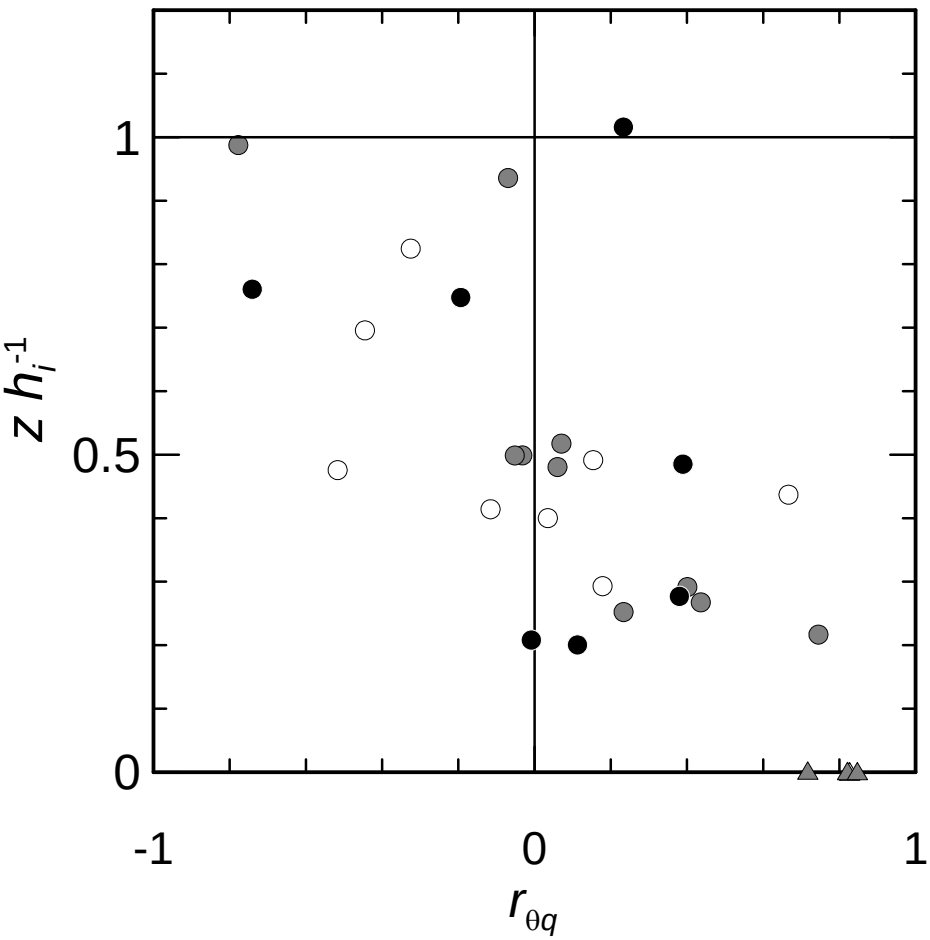

Fig. 3-8 Same as 3-6 but with y-axis normalized height ξ.

sensible heat flux from the surface. This is more clearly displayed when the variance values are normalized with appropriate scaling parameters as shown in Fig. 3-9. As a whole, scatter of $\sigma_\theta^2 T_*^{-2}$ is larger in a relatively wet period, i.e., July and August, as compared to in dry October, which might be due to relatively variable heat source distribution under coexistence of sensible heat and water vapor source during the wet period. On the other hand, in the upper half of mixed layer, any clear tendency is not evident; both case of decreasing and constant (or slightly increasing) correlation of θ and q, and σ_θ^2 with height were observed, which might reflect the effect of entrainment flux from the top of the mixed layer, where a sharp increase of θ and a sharp decrease of q with height make their correlation $r_{\theta q}$ large negative (Wyngaard et al., 1978). The scatter is caused partly by the uneven distribution of overshooting thermals in the entrainment layer (Lenschow and Stephens, 1980) or spatial variability of the height and depth of entrainment layer itself (Hägeli et al., 2000).

3-2 Formulations of Scalar Variance in the Mixed Layer

3-2-1 Validity of Similarity Arguments and Scaling Scheme in the Mixed Layer

In order to assess the nature of the temperature variances obtained in the mixed layer over the experimental area, the observed variables are analysed based on a similarity theory. In the mixed layer, the governing variables are mainly the mixed layer height h_i, buoyancy parameter g/θ with the gravity acceleration g and potential temperature θ, and surface heat flux $\overline{w'\theta'}_0 = H/(\rho c_p)$, namely, the covariance of the vertical wind speed w and θ at the surface with ρ being the density of the air and c_p the specific heat at constant pressure. With these variables the convective scales can be organized. The first such proposal was made by Deardorff (1970a, 1970b), and the velocity scale w_* and the temperature scale T_* can be expressed as follows;

$$w_* = \left[\overline{w'\theta'}_0 \left(g/\theta\right) h_i\right]^{1/3}, T_* = \frac{\overline{w'\theta'}_0}{w_*} = \left[\left(\overline{w'\theta'}_0\right)^2 \left(g/\theta\right)^{-1} h_i^{-1}\right]^{1/3} \tag{3.1}$$

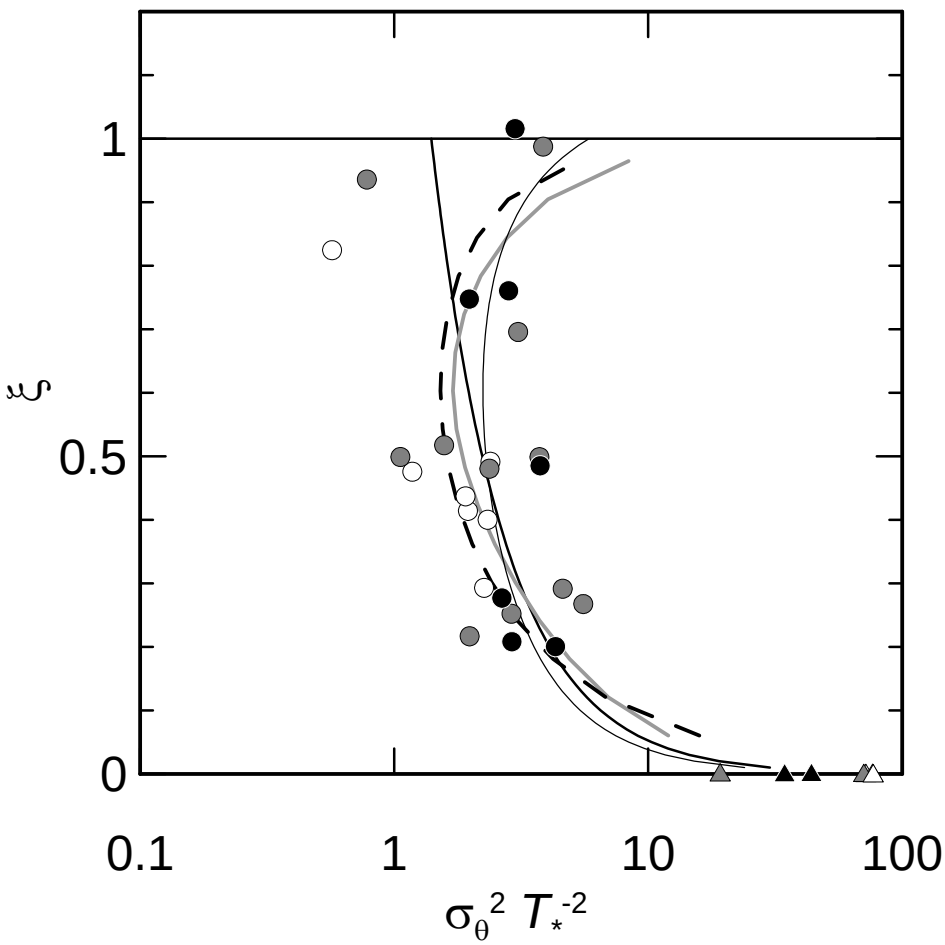

Fig. 3-9 Same as 3-7 but for normalized potential temperature variance $\sigma_\theta^2 T_*^{-2}$ with y-axis normalized height ξ, with previously proposed profile equations.

Solid line for Kaimal et al. (1976), gray line for Sorbjan (1989) and dashed line for Moeng and Wyngaard (1984). Thin solid line is proposed in this study.

The convective scaling can usually be applied when the buoyancy-driven turbulences are more dominate than the shear-driven (i.e., mechanical) turbulences. One of the indices to indicate whether or not the convective scaling is applicable is $\mu = h_i / L$, where L is the Obukhov length, although the actual threshold value where the shear contribution becomes negligible depends on several factors such as surface roughness (Asanuma, 1996). The range of μ in this study was $16 \le |\mu| \le 550$ as will be shown below, and this range in general indicates the dominance of the buoyant convection according to the previous studies (e.g., Wyngaard, 1985). However, since the judgement based on μ value has some ambiguity, there might still be a need for considering the surface shear effects. This can be accomplished by considering appropriate velocity scale, and possible choices are the friction velocity u_* and the convective velocity w_* for mechanical and convective scaling, respectively, and their combination such as $v_* = (w_*^3 + 8u_*^3)^{1/3}$ (Driedonks, 1982). Asanuma (1996) investigated the effects of the choice of the velocity scales on the variance formulation, and his results indicated that except for the u_* scaling, the choice had only a minor influence. Thus, in this study, the convective scaling (i.e., w_* and T_*) was mainly considered, while the v_* scaling was additionally investigated. The dimensionless values $\sigma_\theta^2 T_*^{-2}$ were then plotted against $\xi = zh_i^{-1}$, where z is the sensor, i.e., aircraft height, as shown in Fig. 3-9.

3-2-2 Profile Equations of Variance Statistics

In the past, several formulations have been proposed for the relationship between the scaled scalar variance and ξ. Here three of the formulations proposed in previous studies are presented.

(1) Free Convective Formulation

First, functions based on the free convection argument, in which the convective scaling is relevant, were applied. Among the first was Kaimal et al. (1976) who proposed the following

equation as a simple extension of the surface layer variance equation under the free convective condition derived by Wyngaard et al. (1971), to the mixed layer by replacing L with h_i and θ_* $(= -\overline{w'\theta'}_0 / u_*)$ with T_*;

$$\frac{\sigma_\theta^{\ 2}}{T_*^2} = a\xi^{-2/3} \tag{3.2}$$

and they found (3.2) with a = 1.8 predicted the measurements made by a tethered balloon in Minnesota well up to the height of $0.1 \le \xi$. Lenshow et al. (1980) also compared (3.2) with a = 1.8 with the aircraft measurements made over the East China Sea; Kaimal and Finnigan (1994) have noted that the observations followed (3.2) in the range $0.1 \le \xi \le 0.5$, namely, the lower half of the mixed layer.

(2) Formulation by Sorbjan (1989)

Based also on a convective scaling, a functional form (3.3) was proposed by Sorbjan (1989). The major difference from (3.2) is that he proposed to decompose the statistical variables in the mixed layer under the influence of entrainment at the top of the mixed layer into a non-penetrative part (i.e., without the influence of entrainment) and a residual part. The non-penetrative part represents the diffusion from the ground surface, while the residual part should take care of the entrainment flux. His proposal applied to the temperature variance can be written as

$$\frac{\sigma_\theta^{\ 2}}{T_*^2} = C_{M\theta_0} \frac{(1-\xi)^{4/3}}{\xi^{2/3}} + C_{M\theta_i} A_\theta^{4/3} \frac{\xi^{4/3}}{(1-\xi+D)^{2/3}} \tag{3.3}$$

where A_θ is the entrainment constant for heat flux defined as

$$\overline{w'\theta'}_h = -A_\theta \overline{w'\theta'}_0 \tag{3.4}$$

where $\overline{w'\theta'}_h$ represents the flux at the mixed layer top, and A_θ has been found to take value in the range of 0.2-0.3 (e.g., Stull, 1976). The constants $C_{M\theta_0}$ and $C_{M\theta_i}$ were determined for A_θ = 0.2 by Sorbjan (1989) by fitting (3.3) to the observations of Kaimal et al. (1976) and Caughey and Palmer (1979) although the exact procedure of the curve fitting was not explicitly stated. The symbol D presents the ratio Δ / h_i with Δ being the depth of the interfacial layer above the mixed layer, and its value was taken as zero in the present analysis partly because Sugita and Kawakubo (2003) have demonstrated that an introduction of D did not improve the estimation of fluxes, and mainly because D was not available for the present study. A_θ = 0.2 was also assumed in the following analysis.

(3) Top-down and Bottom-up Diffusion Model

André et al. (1979) analysed the specific humidity gradient in the mixed layer with the idea to treat the turbulence statistics of a passive scalar in the mixed layer as a result of two independent diffusion processes, one originating up from the surface and another down from the capping inversion. This idea was further extended by Wyngaard and Brost (1984) as the so-called top-down and bottom-up (TDBU) model, and a version of the TDBU model for the scalar variance was derived by Moeng and Wyngaard (1984) and can be written as (3.5)

$$\sigma_\theta^{\ 2} = \left(\frac{\overline{w'\theta'}_h}{w_*}\right)^2 f_t(\xi) + 2\left(\frac{\overline{w'\theta'}_h \overline{w'\theta'}_0}{w_*^{\ 2}}\right) f_{tb}(\xi) + \left(\frac{\overline{w'\theta'}_0}{w_*}\right)^2 f_b(\xi) \tag{3.5}$$

The symbols f_t, f_{tb} and f_b represent universal functions of ξ, which can be written as follows,

$$f_t = a_1(1-\xi)^{a_2}, \quad f_{tb} = a_3(1-\xi)^{a_4}\xi^{a_5}, \quad f_b = a_6\xi^{a_7} \tag{3.6}$$

in which a_1 through a_7 are the constants determined empirically in Moeng and Wyngaard (1984) by fitting to the results obtained from the large eddy simulation and to the observations of

Kaimal et al. (1976). Asanuma (1996) generalizes (3.5) by allowing the adaptation of different velocity scales at the inversion base v_h and at the surface v_0 as follows;

$$\sigma_\theta^{\ 2} = \left(\frac{\overline{w'\theta'}_h}{v_h} \right)^2 f_t(\xi) + 2\left(\frac{\overline{w'\theta'}_h}{v_h} \frac{\overline{w'\theta'}_0}{v_0} \right) f_{tb}(\xi) + \left(\frac{\overline{w'\theta'}_0}{v_0} \right)^2 f_b(\xi) \tag{3.7}$$

In this formulation, (3.5) can be seen as a special case of $v_h = v_0 = w_*$. As mentioned above, these scales could include the effects of the surface shear and the convective forcing (i.e., buoyancy), and thus some combinations including w_* and v_* were considered for v_h and v_0 in the following analysis. Since the velocity was not directly measured by the aircraft in the present study, u_* was estimated by Rossby-number similarity which utilizes the geostrophic wind and the surface roughness z_0 as inputs. The detailed procedure to derive z_0 and u_* values is described in the Appendix A-2, but, briefly, z_0 around the target area was determined from the topographic analysis as z_0 = 0.054 m and z_0 = 0.430 m for NW and SE directions from the KBU station as the origin, respectively. A preliminary analysis has shown that the estimates of the sensible heat flux were not different by more than 1% for both cases of z_0, only the results obtained with z_0 = 0.430 m are presented in what follows.

For the application of (3.7), the entrainment flux $\overline{w'\theta'}_h$ must also be expressed in terms of other variables, since $\overline{w'\theta'}_h$ was not measured directly. In addition to (3.4), another model proposed by Tennekes (1973) that includes both buoyancy (i.e., surface flux) driven and shear driven entrainment was considered.

$$\overline{w'\theta'}_h = -A\overline{w'\theta'}_0 + BT_a u_*^{\ 3}(gh_i)^{-1} \tag{3.8}$$

Here A and B are constants and T_a is the air temperature. Eq. (3.8) can be rewritten as the similar form as (3.4),

$$\overline{w'\theta'}_h = -A_\theta \overline{w'\theta'}_0 = \left[-A + BT_a u_* \left(gh_i \overline{w'\theta'}_0 \right)^{-1} \right] \overline{w'\theta'}_0 \tag{3.9}$$

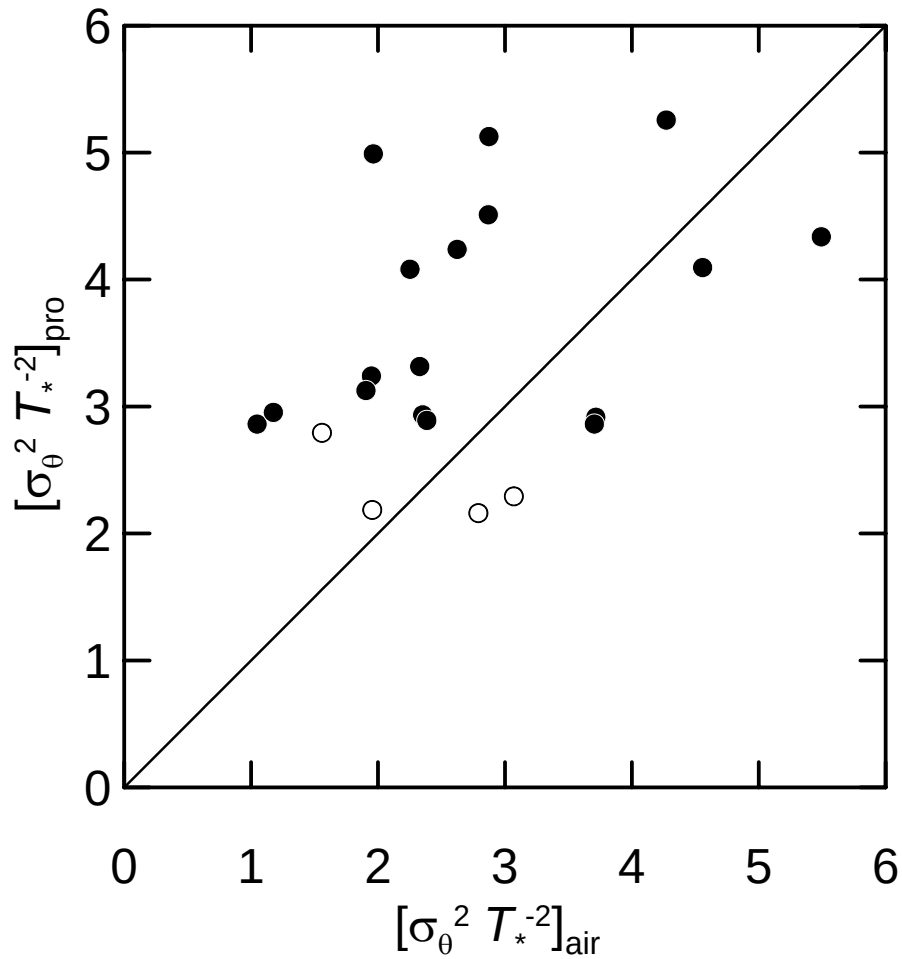

Fig. 3-10a Comparison between the normalized variance of potential temperature $[\sigma_\theta^2 T_*^{-2}]_{pro}$ estimated with Eq.(3.2) and $[\sigma_\theta^2 T_*^{-2}]_{air}$ that of observed above the KBU area.

Solid and open circle show the data for normalized height ξ<0.5 and ξ < 0.8 respectively.

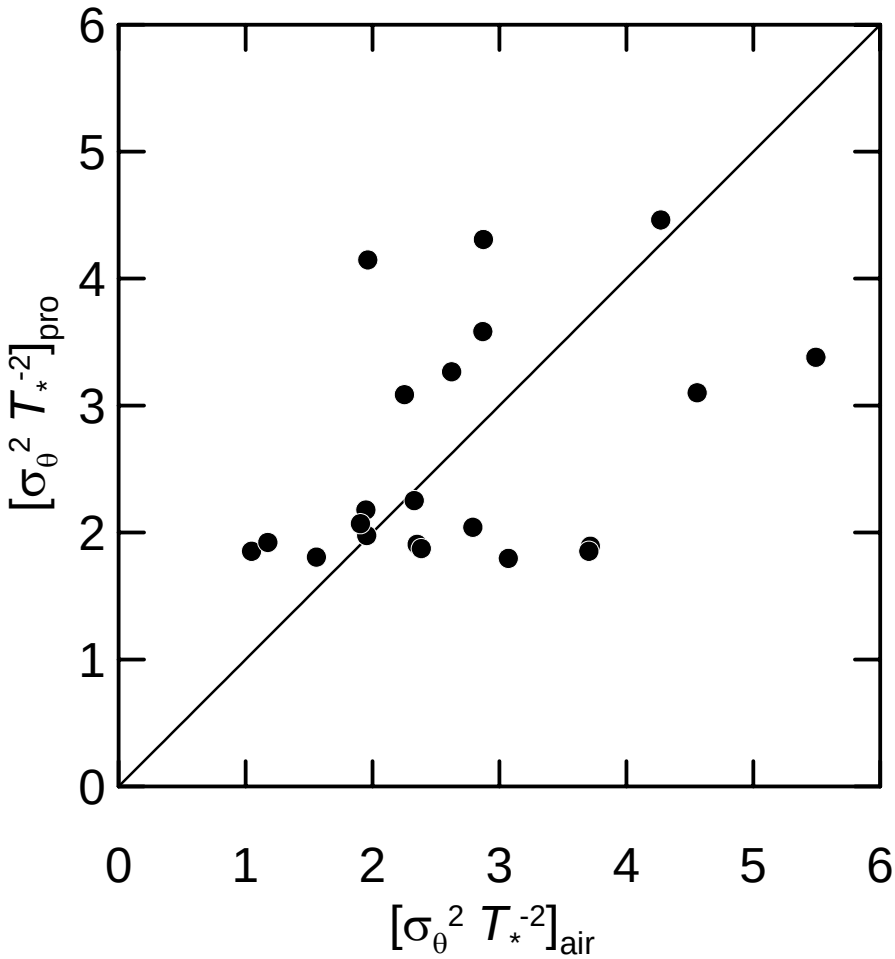

Fig. 3-10b Same as 3-10a but for Eq.(3.3) and the data of normalized height $\xi < 0.8$.

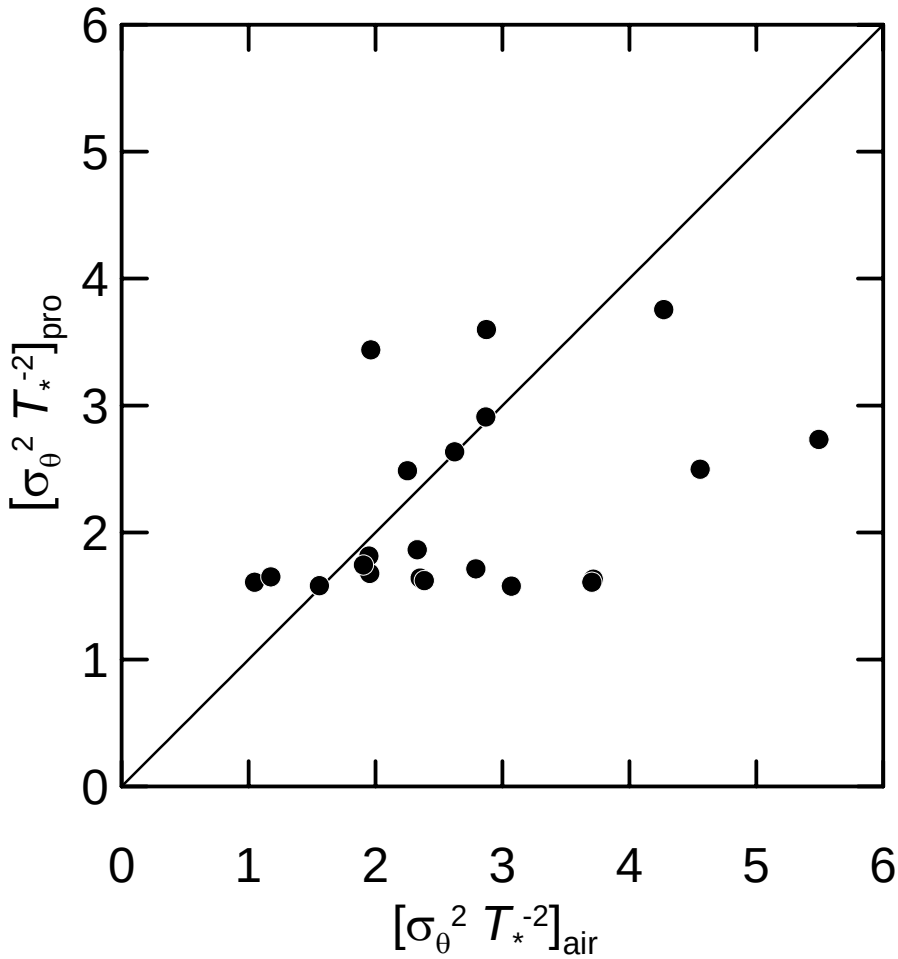

Fig. 3-10c Same as 3-10a but for Eq.(3.5) and the data of normalized height $\xi < 0.8$.

more complex with variables difficult or even practically impossible to obtain, it is of some interest to make a simpler equation such as (3.2) but that allows prediction of the increase of σ_θ^2 at higher levels in the mixed layer near $z = h_i$. One of such simple functions can be expressed as

$$\frac{\sigma_\theta^{\ 2}}{T_*^{\ 2}} = b_1 \xi^{-2/3} + b_2 \left(b_3 - \xi \right)^{b_4} \tag{3.11}$$

This formulation is based on a similar idea to the TDBU and that of Sorbjan's with the superposition of the two diffusion processes, one from the surface and one from the mixed layer top, but unlike their formulations, the relevant variable is ξ only, though, actually, Sorbjan's parameter D may be considered in constant b_3. The constants b_1 through b_4 are also determined as follows; some combinations of these constants that produced the local smallest rms difference between the calculated and observed dimensionless variance $\sigma_\theta^2 T_*^{-2}$ were found by changing the constants in small steps. Simultaneously, the combination that allow prediction of $\sigma_\theta^2 T_*^{-2}$ which agrees with that by (3.5) at $z > 0.8h_i$ was finally selected. In another word, constants were selected in such a way that allows (3.11) simulating the effect of the entrainment as expressed by (3.5). Comparison of $\sigma_\theta^2 T_*^{-2}$ between observed and estimated with (3.11) is shown in Fig. 3-10d, and its rms difference is 1.00, which is the same level of the other formulations.

With those two models and velocity scales, (3.7) was tested for three cases of i) $v_0 = v_h = w_*$ with (3.4), ii) $v_0 = v_*$, $v_h = w_*$ with (3.4), and iii) $v_0 = v_h = v_*$ with (3.9). The first case corresponds to the pure convective scaling, and (3.7) can be rewritten with (3.4) in a similar format as (3.2)-(3.3) as follows and its functional form with the constants in (3.6) proposed by Moeng and Wyngaard (1984) is shown in Fig. 3-9.

$$\frac{\sigma_\theta^{\ 2}}{T_*^2} = A_\theta^{\ 2} f_t(\xi) + 2A_\theta f_{tb}(\xi) + f_b(\xi) \tag{3.10}$$

For other two cases, Asanuma (1996) derived the constants in (3.6) with data from the aircraft observation. Sugita and Kawakubo (2003) also determined these constants with the data obtained from the tower observation by optimising the constants to minimize the error of flux evaluation. These coefficients are listed in Table 4-1 for each case.

3-2-3 Comparisons with Observed Data

Figure 3-9 indicates that the observed variance values follow roughly the proposed functional forms, except in the upper parts of the mixed layer, where the scatter becomes larger. This is partly because the entrainment flux is dominant near the inversion layer. Since the depth of the inversion layer can be as large as about 40% of that of the mixed layer (Stull, 1988) and there are some uncertainties remaining in the estimated values of h_i, the values registered as just below h_i could actually have been above the mixed layer or within the inversion layer. Thus, it was decided not to use the four data sets obtained at heights above $0.8h_i$ for the purpose of estimating fluxes.

Normalized variance calculated with Eqs. (3.2), (3.3) and (3.5) with (3.4) are compared to that observed by aircraft and normalized with the surface flux observed on the ground in Figs. 3-10a to 3-10c, and the root mean square (rms) difference between them is 1.49, 1.11 and 1.17, for Eqs. (3.2), (3.3) and (3.5), respectively, which is almost the same among the formulations.

Since it is the treatment of the entrainment that makes relevant equations (3.3) and (3.5)

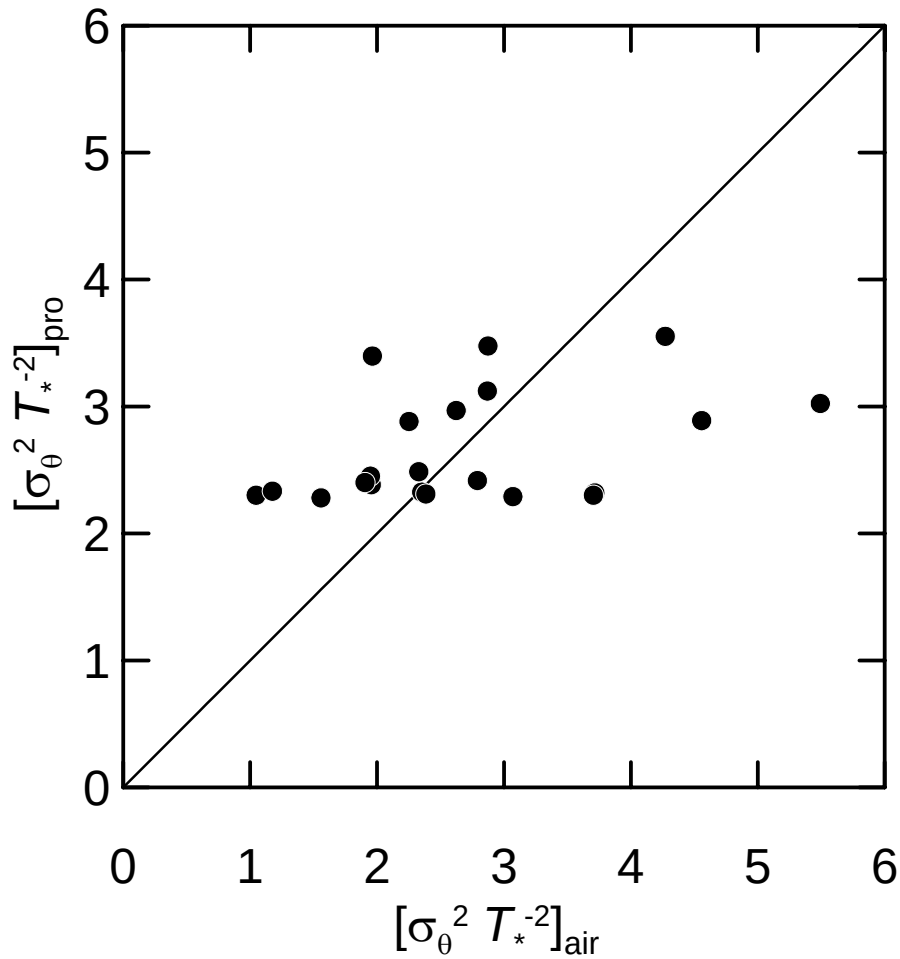

Fig. 3-10d Same as 3-10a but for Eq.(3.10) and the data of normalized height $\xi < 0.8$.

4-1 Derivation of Flux-Variance Formulations

Equations (3.2), (3.3) with $D = 0$, and (3.11) can be recast to obtain the surface flux $\overline{w'\theta'}_0$ as

$$\overline{w'\theta'}_0 = \sigma_\theta^{3/2}\left[\frac{gh_i}{\theta}\right]^{1/2}\left(a\xi^{-2/3}\right)^{-3/4} = \sigma_\theta^{3/2}\left[\frac{gz}{\theta}\right]^{1/2} a^{-3/4}, \tag{4.1}$$

$$\overline{w'\theta'}_0 = \sigma_\theta^{3/2}\left[\frac{gh_i}{\theta}\right]^{1/2}\left[C_{M\theta_0}\frac{(1-\xi)^{4/3}}{\xi^{2/3}} + C_{M\theta_i}A_\theta^{4/3}\frac{\xi^{4/3}}{(1-\xi)^{2/3}}\right]^{-3/4} \tag{4.2}$$

and

$$\overline{w'\theta'}_0 = \sigma_\theta^{3/2}\left[\frac{gh_i}{\theta}\right]^{1/2}\left[b_1\xi^{-2/3} + b_2\left(b_3-\xi\right)^{b_4}\right]^{-3/4}, \tag{4.3}$$

respectively. The values of constant coefficients are listed in Table 4-1. Similarly, the generalized TDBU formulation (3.7) can be rewritten as follows,

$$\overline{w'\theta'}_0 = \sigma_\theta\left[\frac{A_\theta^{\,2}}{v_h^{\,2}}f_t(\xi) - 2\frac{A_\theta}{v_h v_0}f_{tb}(\xi) + \frac{1}{v_0^{\,2}}f_b(\xi)\right]^{-1/2} \tag{4.4}$$

For case i) $v_0 = v_h = w_*$ with (3.4), this can easily be solved to obtain $\overline{w'\theta'}_0$ from σ_θ. However, for the case ii) $v_0 = v_*$ and $v_h = w_*$ with (3.4) and case iii) $v_0 = v_h = v_*$ with (3.9), (4.4) becomes an implicit function for $\overline{w'\theta'}_0$. Thus, an iteration procedure is required to solve (4.4). This was carried out as follows; first, $\overline{w'\theta'}_0 = \overline{w'\theta'}_s$ was assumed in the right hand side (RHS) of (4.4), and this produced the first estimate of $\overline{w'\theta'}_0$. Then this value was inserted in the RHS of (4.4) and the second estimate was derived. This process was repeated until $\overline{w'\theta'}_0$ value had converged sufficiently. Note that the choice of the first estimate is not really relevant since the

Table 4-1 List of constants in variance formulations.

(a) Eqs. (3.2) / (4.1)

variance formulation	z/h_i	a
Kaimal et al. (1976)		1.8
C/C	< 0.5	1.4
C/C	< 0.8	1.5

(b) Eqs. (3.3) / (4.2)

variance formulation	A_θ	D	$C_{M\theta 0}$	$C_{M\theta i}$
Sorbjan (1989)	0.2	0	2	8
C/C	0.2	0	1.6	18.0

(c) Eqs. (3.7) / (4.4)

variance formulation				a_1	a_2	a_3	a_4	a_5	a_6	a_7
	v_0	v_h								
MW84	w_*	w_*	(3.4) with $A_\theta = 0.2$	14	-2/3	1	–	–	0.47	-5/4
SK03	w_*	w_*	(3.4) with $A_\theta = 0.2$	25.0	-2/3	0.91	–	–	0.53	-5/4
C/C	w_*	w_*	(3.4) with $A_\theta = 0.2$	28.0	-2/3	0.31	-1/3	-5/8	0.33	-5/4
A96	v_*	w_*	(3.4) with $A_\theta = 0.2$	38.3	-3/2	8.01	-3/4	-5/8	2.04	-5/4
SK03	v_*	w_*	(3.4) with $A_\theta = 0.2$	45.0	-2/3	6.00	-1/3	-5/8	1.89	-5/4
C/C	v_*	w_*	(3.4) with $A_\theta = 0.2$	11.2	-2/3	0	-3/4	-5/8	0.45	-5/4
A96	v_*	v_*	(3.8) with $A = 0.2$, B=5	2.58	-3/2	3.3	0	0	1.04	-5/4
SK03	v_*	v_*	(3.8) with $A = 0.2$, B=5	10.71	-2/3	0	-1/3	-5/8	1.05	-5/4
C/C	v_*	v_*	(3.8) with $A = 0.2$, B=5	5.8	-2/3	3.0	-1/3	-5/8	0.29	-5/4

(d) Eq. (3.11) / (4.3)

variance formulation	b_1	b_2	b_3	b_4
optimizing variance	1.1	0.3	1.1	-1.2
optimizing flux	0.9	0.7	1.2	-1.2

Table 4-1 (continued)

(e) Eq. (4.11) / (4.12)

$F(\xi)$	variance formulation v_0	v_h		c_1	c_2	c_3	c_4	c_5	c_6	c_7	c_8	c_9
(3.2)	–	–	z/h_i <0.5	27.2	-2	-1.2	-3	765.3	-2	-8.1	-1	0.0
(3.2)	–	–	z/h_i <0.8	549.3	-1	-1.8	-3	41.0	-1	176.4	-3	0.0
(3.3)	–	–	–	18.7	-1	-0.9	-3	704.6	-2	-4.0	-1	-0.1
(3.7)	w_*	w_*	(3.4) with $A_\theta = 0.2$	16.3	-1	-0.8	-3	688.2	-2	-15.9	-2	-0.1
(3.11)	–	–	–	305.9	-2	-0.7	-3	661.3	-2	-40.2	-3	-0.2

MW84: Moeng and Wyngaard (1984), SK03: Sugita and Kawakubo (2003),
A96: Asanuma (1996), C/C: Coefficients calibrated in this study

choice of the twice and 1/2 of the $\overline{w'\theta'}_s$ as $\overline{w'\theta'}_0$ resulted in the same final value. In what follows, surface fluxes derived from (4.1)-(4.4) will be denoted as $\overline{w'\theta'}_{vm}$. The comparison between $\overline{w'\theta'}_{vm}$ and $\overline{w'\theta'}_s$ are shown in Figs. 4-1a to 4-1f and statistics in Table 4-2 for each formulation. For Eq. (4.4) with the three cases of velocity scale (Figs. 4-1d, e and f), the results with constants of Sugita and Kawakubo (2003) are also shown, where all of three cases gave the smaller rms difference between $\overline{w'\theta'}_{vm}$ and $\overline{w'\theta'}_s$ than that with the original constants in Moeng and Wyngaard (1984) for case i) and Asanuma (1996) for case ii) and iii).

4-2 Calibrations of the Experimental Coefficients

As mentioned, the constants in these equations are still not well established. As such, in the present analysis, first the constants proposed in the previous studies were tested, and then they were calibrated with the current data sets. The calibration was performed in the same manner as in Sugita and Kawakubo (2003), where the constants were changed in small steps until the rms difference between $\overline{w'\theta'}_{vm}$ and $\overline{w'\theta'}_s$ reached a minimum. For the TDBU formulation, the powers of (3.6) were retained and only the others were changed because of rather insufficiency in number of data. It should be noted that a data set for evaluation of the variance methods is identical to that used for the constant calibration also due to insufficient number of data; ideally, independent data should be used in calibration and evaluation of output.

These results are shown graphically in Figs. 4-2a to 4-2g, and the calibrated constants and relevant statistics are listed in Table 4-1 and Table 4-2, respectively. Figures 4-2f and 4-2g indicate that the cases ii) and iii), in which v_* was assigned as the relevant velocity scale resulted in a large rms difference. Since it is possible that the uncertainty of u_*, which contributes in the velocity scale v_*, caused the outliers, a sensitivity test for flux estimation was carried out. Given a typical condition of θ = 300 K, u_* = 0.25 m s^{-1} and $\overline{w'\theta'}_s$=0.15 K m s^{-1}, standard deviation of temperature σ_θ was changed ±0.1 K from 0.15 K and the resulting changes of $\overline{w'\theta'}_{vm}$ were examined. The result is shown graphically in Figs. 4-3a and 4-3b for the cases i), ii) and iii) of (4.4) with constants proposed in the original literature and those calibrated with the current dataset, respectively. It can be seen that the estimated flux is sensitive to σ_θ at around

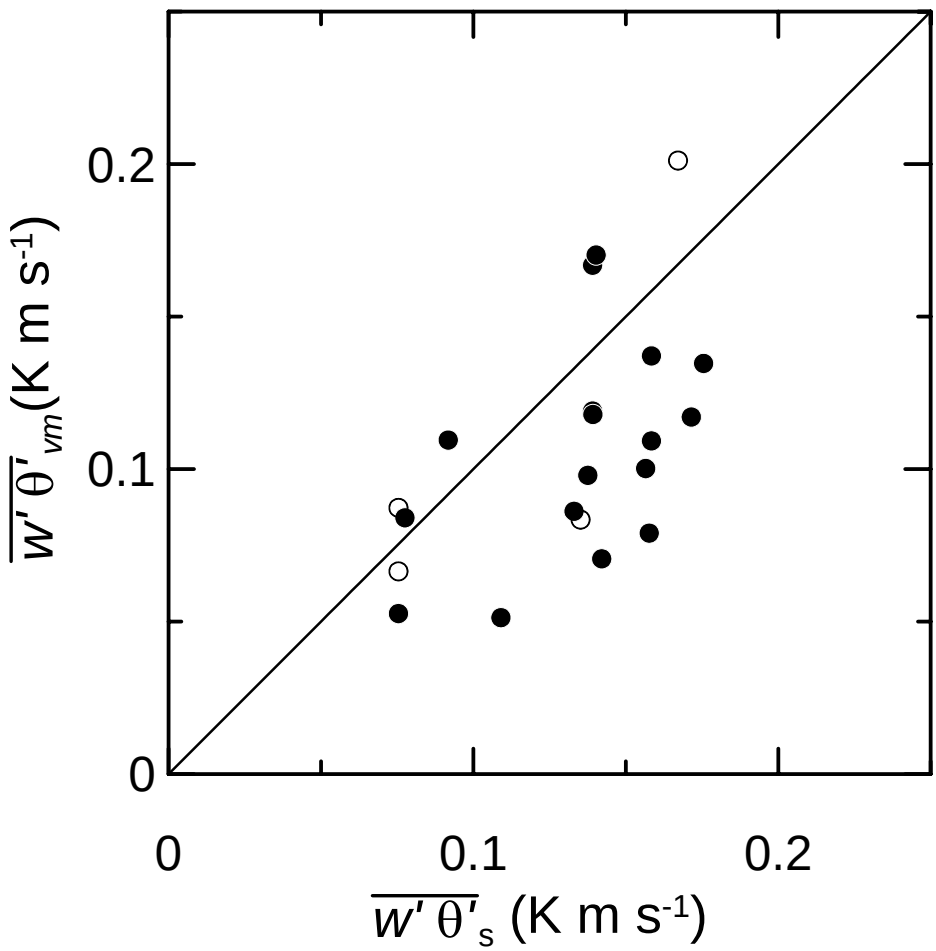

Fig. 4-1a Comparison between the sensible heat flux $\overline{w'\theta'}_{vm}$ estimated from Eq.(4.1) with the original constants in the literature and $\overline{w'\theta'}_s$ observed by eddy covariance method at the KBU flux station.

Solid and open circle show the data for normalized height $\xi < 0.5$ and $0.5 \leq \xi < 0.8$, respectively.

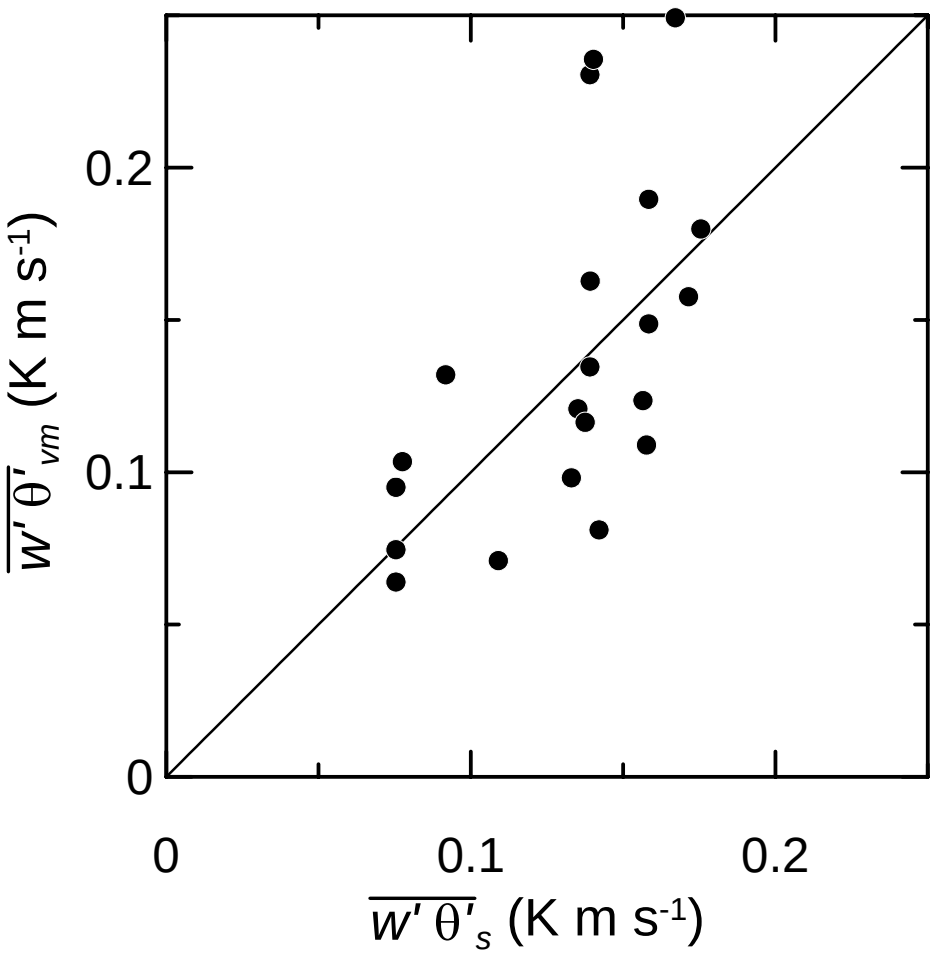

Fig. 4-1b Same as 4-1a but for Eq.(4.2) and the data of normalized height $\xi < 0.8$.

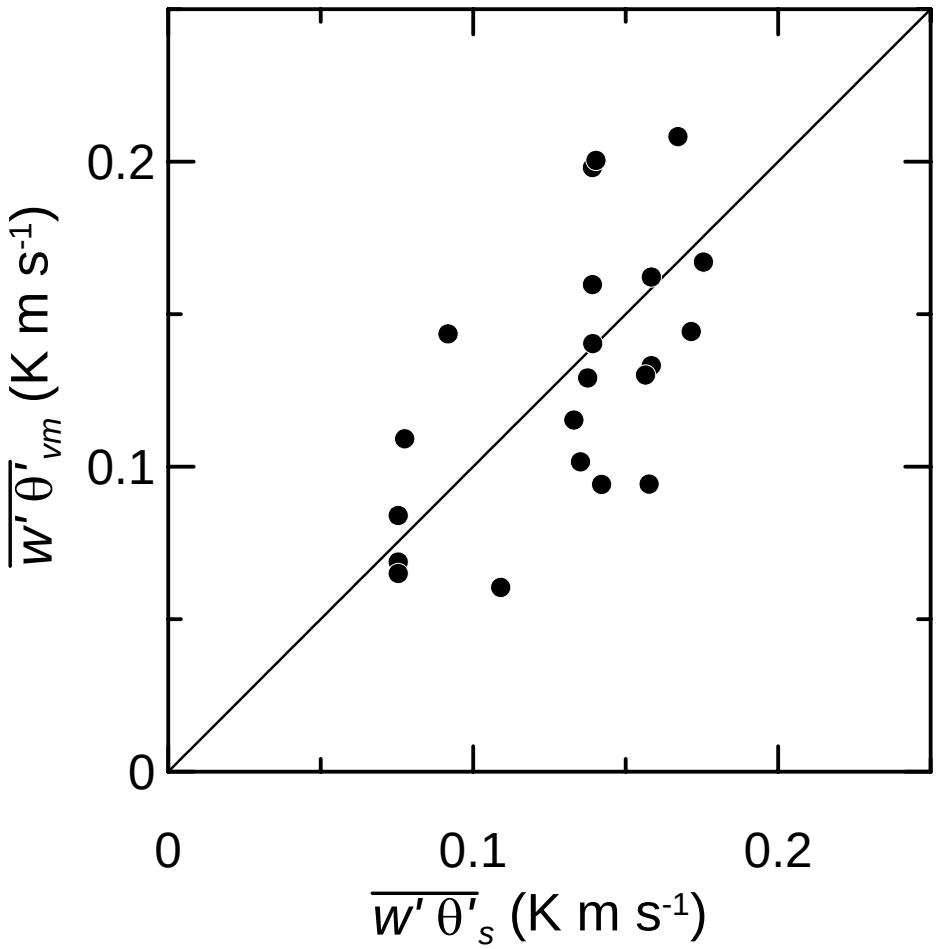

Fig. 4-1c Same as 4-1a but for Eq. (4.3) and the data of normalized height $\xi < 0.8$.

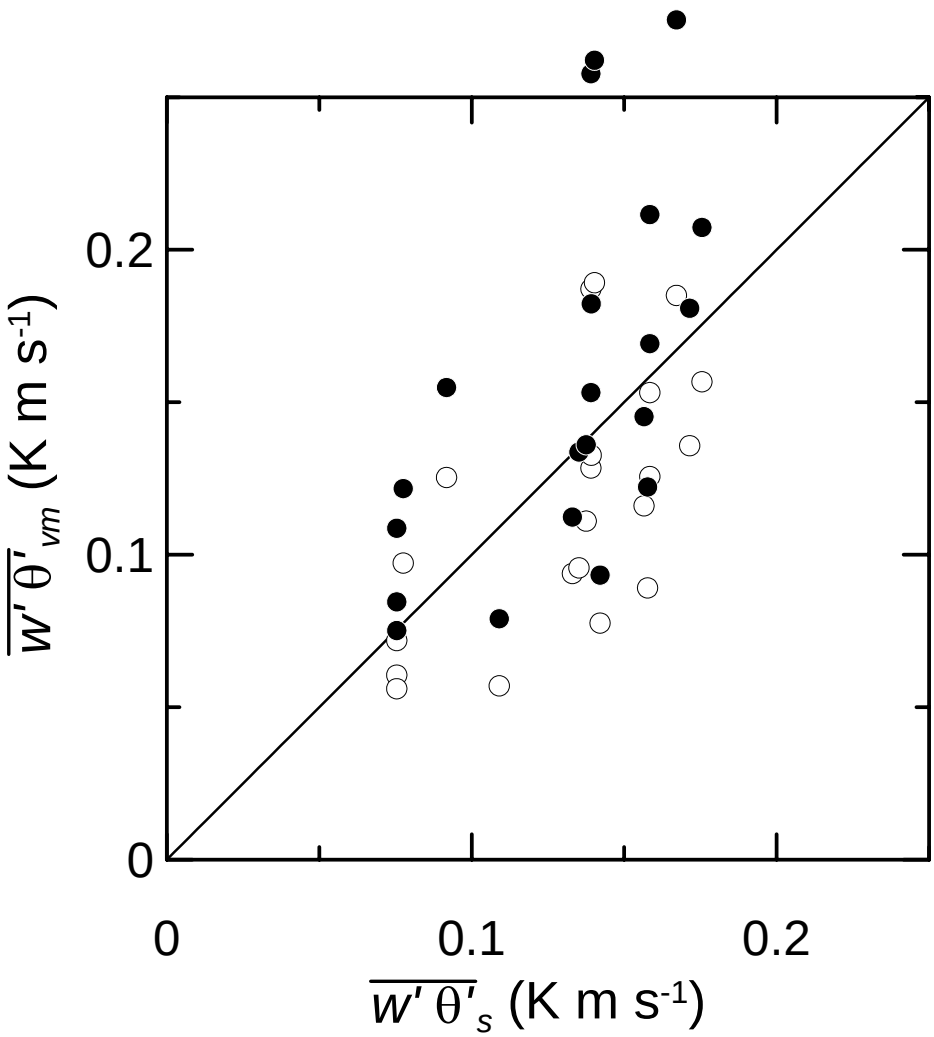

Fig. 4-1d Same as 4-1a but for Eq.(4.4) with velocity scale $v_0 = v_h = w_*$ and entrainment model (3.4), and the data of normalized height $\xi < 0.8$. Open circles represent the results of the same formulation but the coefficients of Sugita and Kawakubo(2003) were used.

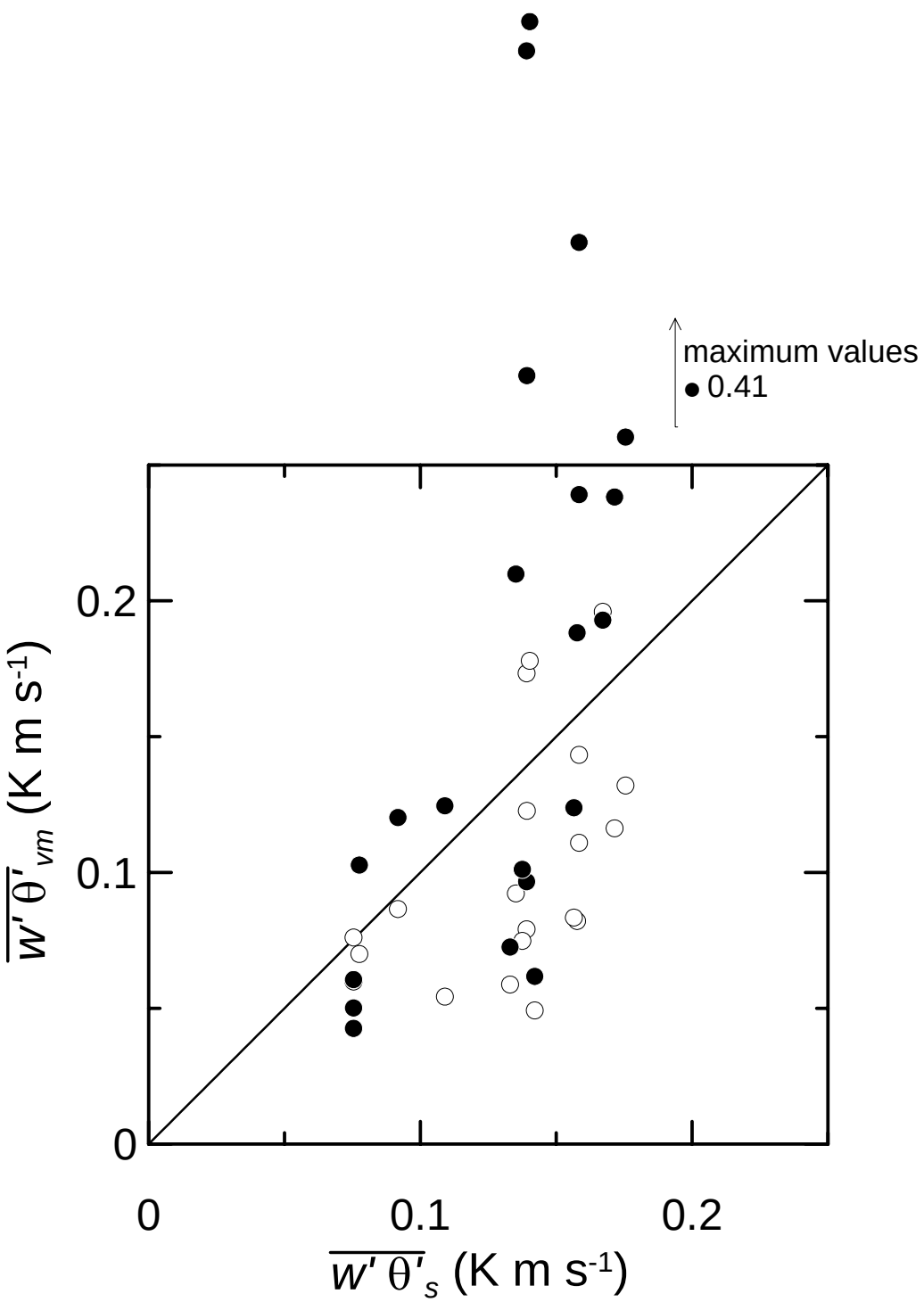

Fig. 4-1e Same as 4-1a but for Eq.(4.4) with velocity scale $v_0 = v_*$, $v_h = w_*$ and entrainment model (3.4), and the data of normalized height $\xi < 0.8$. Open circles represent the results of the same formulation but the coefficients of Sugita and Kawakubo(2003) were used.

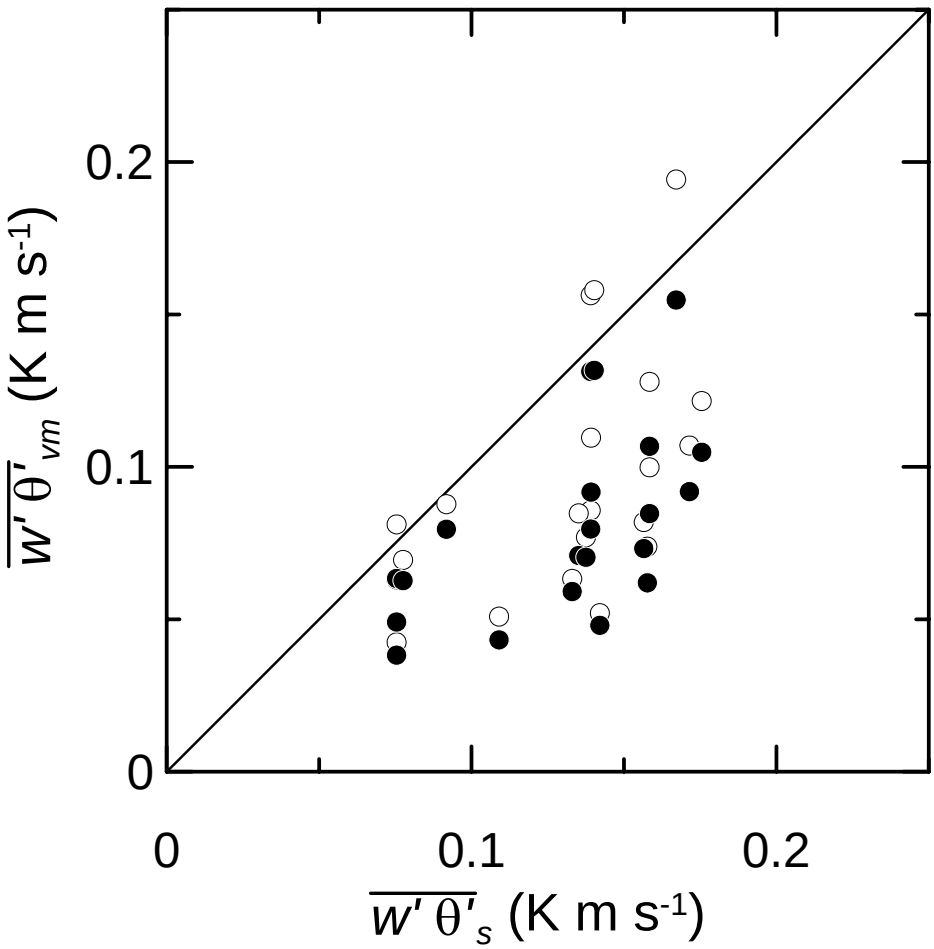

Fig. 4-1f Same as 4-1a but for Eq. (4.4) with velocity scale $v_0 = v_h = v_*$ and entrainment model (3.9), and the data of normalized height $\xi < 0.8$. Open circles represent the results of the same formulation but the coefficients of Sugita and Kawakubo(2003) were used.

Table 4-2 Statistics in the comparison of flux, $\overline{w'\theta'}_s$ derived form the eddy covariance method at the ground station, and $\overline{w'\theta'}_{vm}$ estimated by the variance methods.

(a) Eq. (4.1)

variance formulation	z/h_i	N	rms difference (K m s^{-1})	a	b	d	$\overline{w'\theta'}_s/\overline{w'\theta'}_{vm}$
Kaimal et al. (1976)	< 0.5	17	0.044	0.034	0.53	0.59	0.78
C/C	< 0.5	17	0.038	0.043	0.64	0.65	0.95
A/P	< 0.5	17	0.032	0.003	0.92	0.99	0.94
Kaimal et al. (1976)	< 0.8	21	0.042	0.024	0.64	0.67	0.82
C/C	< 0.8	21	0.039	0.028	0.73	0.70	0.94
A/P	< 0.8	21	0.034	0.023	0.78	0.74	0.96

(b) Eq. (4.2)

variance formulation	N	rms difference (K m s^{-1})	a	b	d	$\overline{w'\theta'}_s/\overline{w'\theta'}_{vm}$
Sorbjan (1989)	21	0.043	0.009	0.97	0.70	1.04
C/C	21	0.034	0.013	0.84	0.77	0.95
A/P	21	0.029	-0.01	1.02	0.84	0.95

(c) Eq. (4.3)

variance formulation	N	rms difference (K m s^{-1})	a	b	d	$\overline{w'\theta'}_s/\overline{w'\theta'}_{vm}$
optimizing variance	21	0.035	0.025	0.79	0.76	0.98
C/C (optimizing flux)	21	0.034	0.026	0.75	0.77	0.95
A/P	21	0.029	-0.001	0.97	0.83	0.96

Table 4-2 (continued)

(d) Eq. (4.4)

	variance formulation			N	rms difference (K m s^{-1})	a	b	d	$\overline{w'\theta'_s}/\overline{w'\theta'_{vm}}$
	v_0	v_h	entrainment model						
MW84	w_*	w_*	(3.4) with A_θ = 0.2	21	0.053	0.014	1.07	0.63	1.19
SK03	w_*	w_*	(3.4) with A_θ = 0.2	21	0.036	0.014	0.78	0.75	0.89
C/C	w_*	w_*	(3.4) with A_θ = 0.2	21	0.034	0.023	0.81	0.77	0.98
A/P	w_*	w_*	(3.4) with A_θ = 0.2	21	0.027	0.001	0.95	0.83	0.95
A96	v_*	w_*	(3.4) with A_θ = 0.2	21	0.107	-0.071	1.89	0.42	1.35
SK03	v_*	w_*	(3.4) with A_θ = 0.2	21	0.049	0.002	0.74	0.64	0.76
C/C	v_*	w_*	(3.4) with A_θ = 0.2	21	0.046	0.018	0.98	0.68	1.12
A96	v_*	v_*	(3.9) with A = 0.2,B=5	21	0.058	0.012	0.52	0.55	0.61
SK03	v_*	v_*	(3.9) with A = 0.2,B=5	21	0.050	0.013	0.62	0.61	0.72
C/C	v_*	v_*	(3.9) with A = 0.2,B=5	21	0.044	0.019	0.61	0.66	0.75

MW84: Moeng and Wyngaard (1984), SK03: Sugita and Kawakubo (2003), A96: Asanuma (1996), C/C: Coefficients calibrated to optimize flux estimation in this study, A/P: Coefficients calibrated in this study with additional parameters, *N*: number of data, rms: root mean square, *a*: intercept of regression line, *b*: slope of regression line ($\overline{w'\theta'_{vm}} = a + b\,\overline{w'\theta'_s}$), $\overline{w'\theta'_{vm}}$: estimated flux by variance methods, $\overline{w'\theta'_s}$: observed flux at the KBU station, *d*: index of agreement (Willmott, 1981), $\overline{w'\theta'_s}/\overline{w'\theta'_{vm}}$: ratio of the mean $\overline{w'\theta'_s}$ and $\overline{w'\theta'_{vm}}$

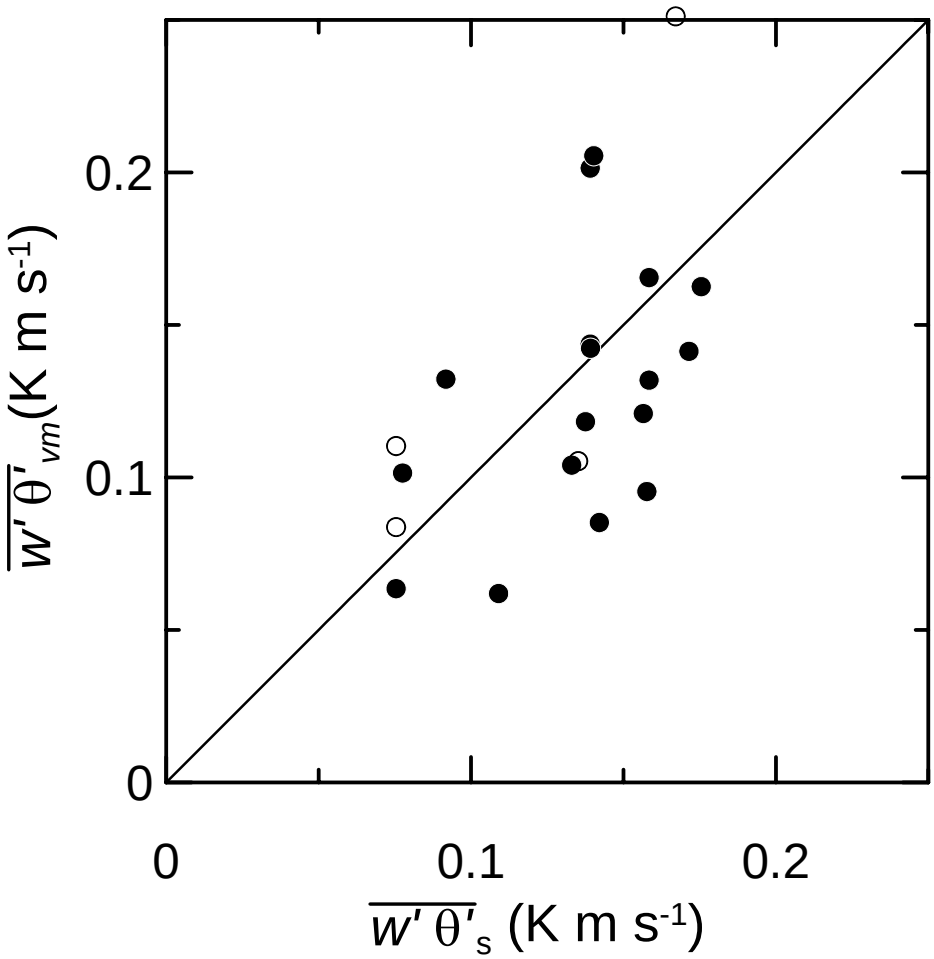

Fig. 4-2a Comparison between the sensible heat flux $\overline{w'\theta'}_{vm}$ estimated from Eq.(4.1) with calibrated constants and $\overline{w'\theta'}_s$ observed by eddy covariance method at the KBU flux station.

Solid and open circle show the data for normalized height $\xi < 0.5$ and $0.5 \leq \xi < 0.8$, respectively. (Calibration was carried out for the data of $\xi < 0.5$)

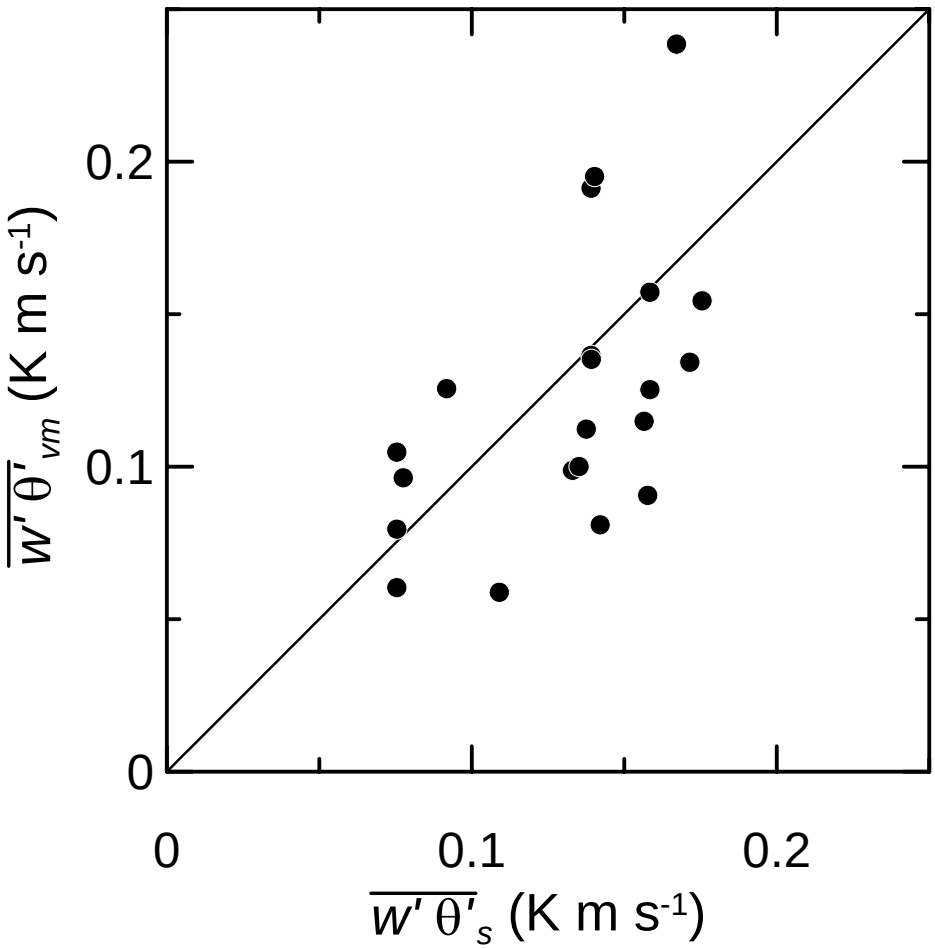

Fig. 4-2b Same as 4-2a but for Eq.(4.1) and the data of normalized height $\xi < 0.8$. (Calibration was carried out for the data of $\xi < 0.8$)

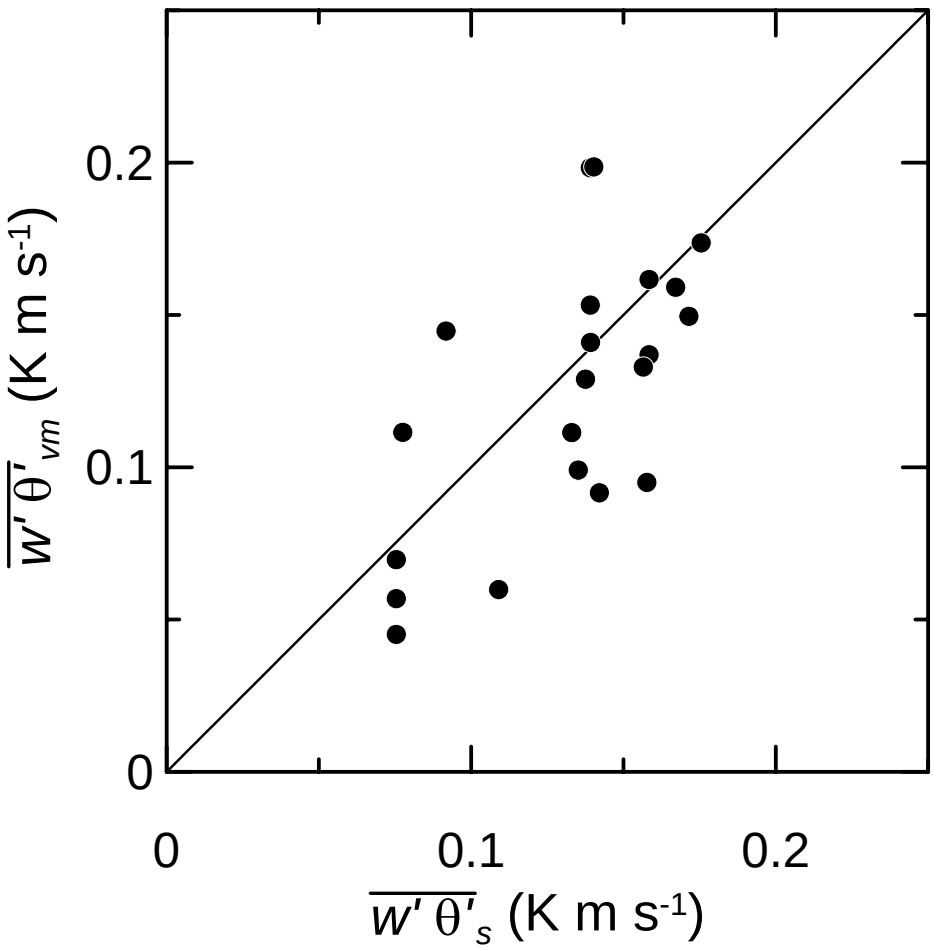

Fig. 4-2c Same as 4-2a but for Eq.(4.2) and the data of normalized height $\xi < 0.8$.

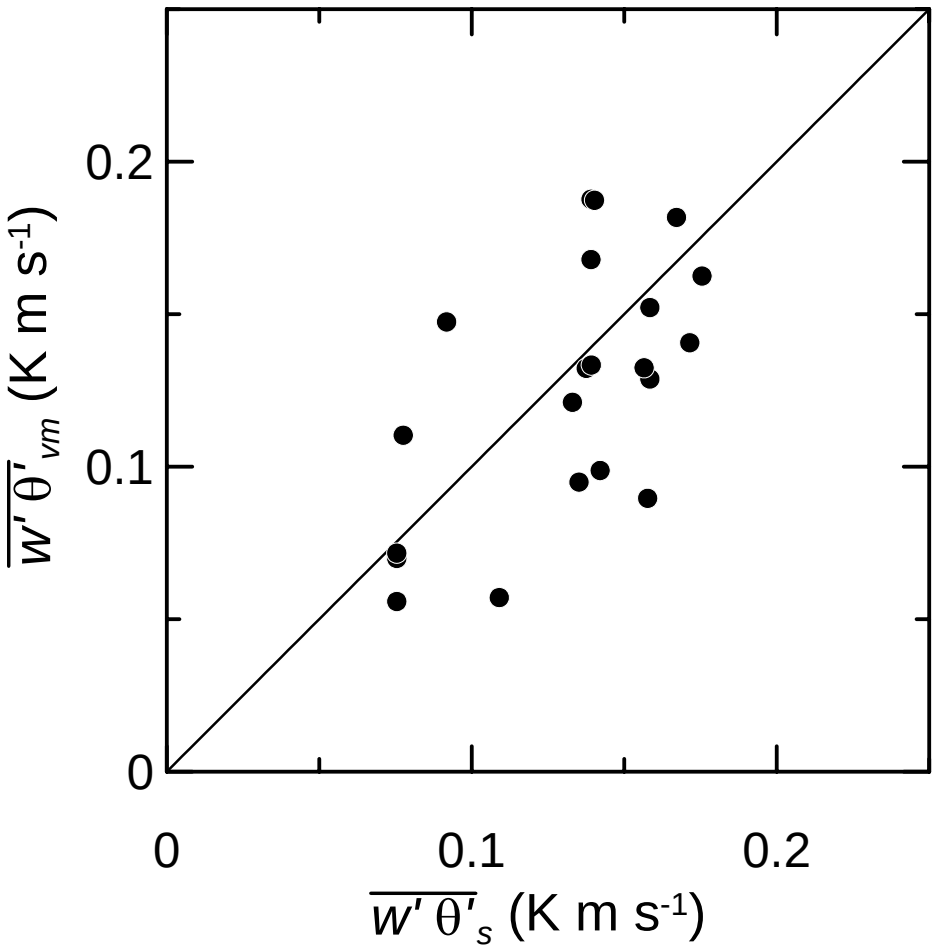

Fig. 4-2d Same as 4-2a but for Eq. (4.3) and the data of normalized height $\xi < 0.8$.

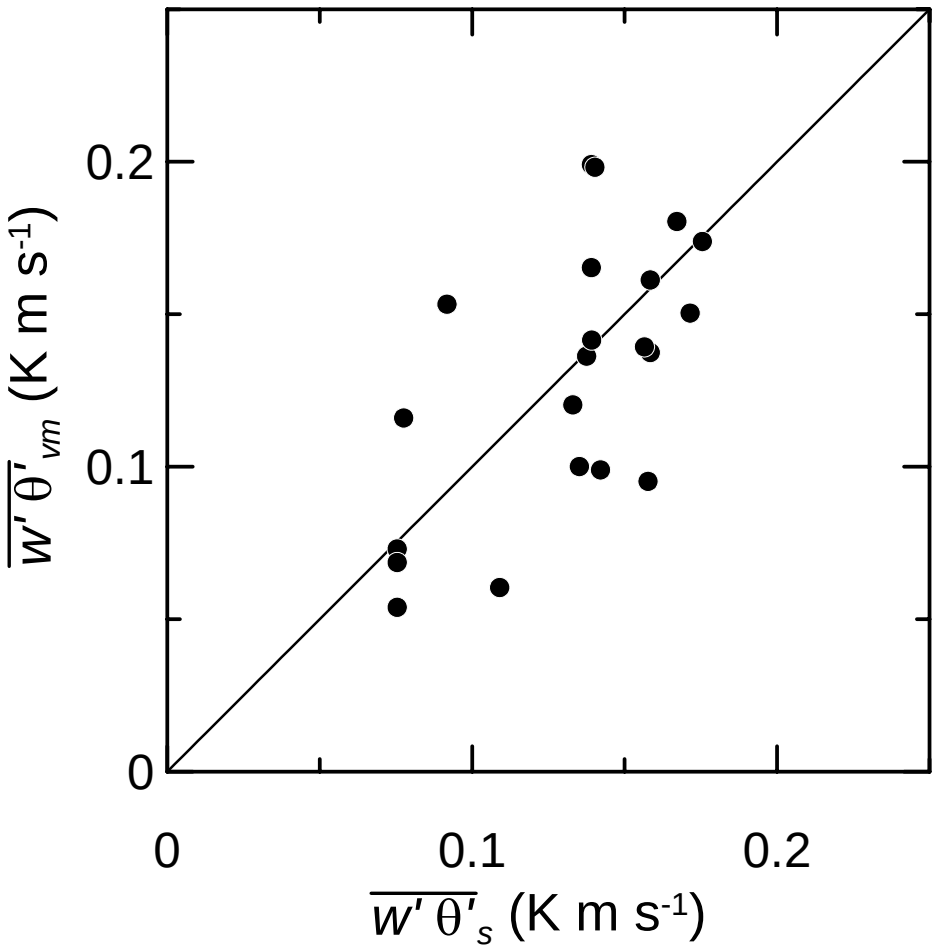

Fig. 4-2e Same as 4-2a but for Eq.(4.4) with velocity scale $v_0 = v_h = w_*$ and entrainment model (3.4), and the data of normalized height $\xi < 0.8$.

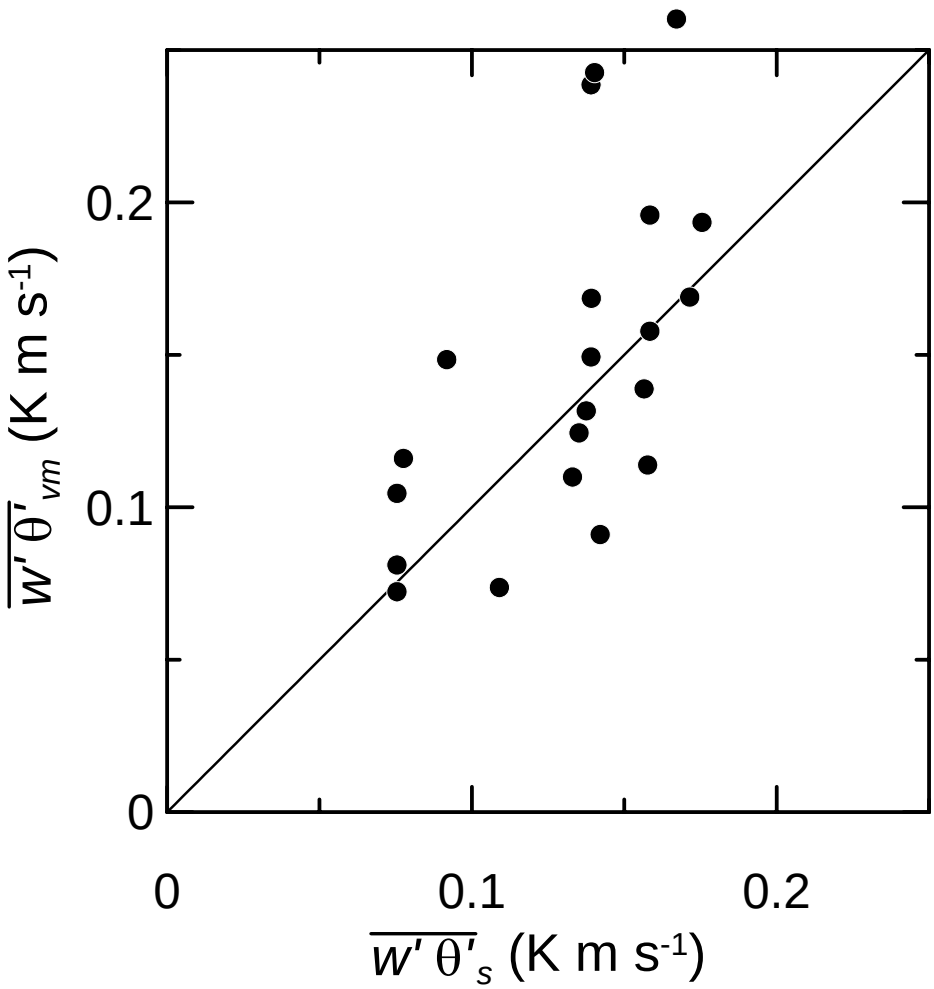

Fig. 4-2f Same as 4-2a but for Eq.(4.4) with velocity scale $v_0 = v_*$, $v_h = w_*$ and entrainment model (3.4), and the data of normalized height $\xi < 0.8$.

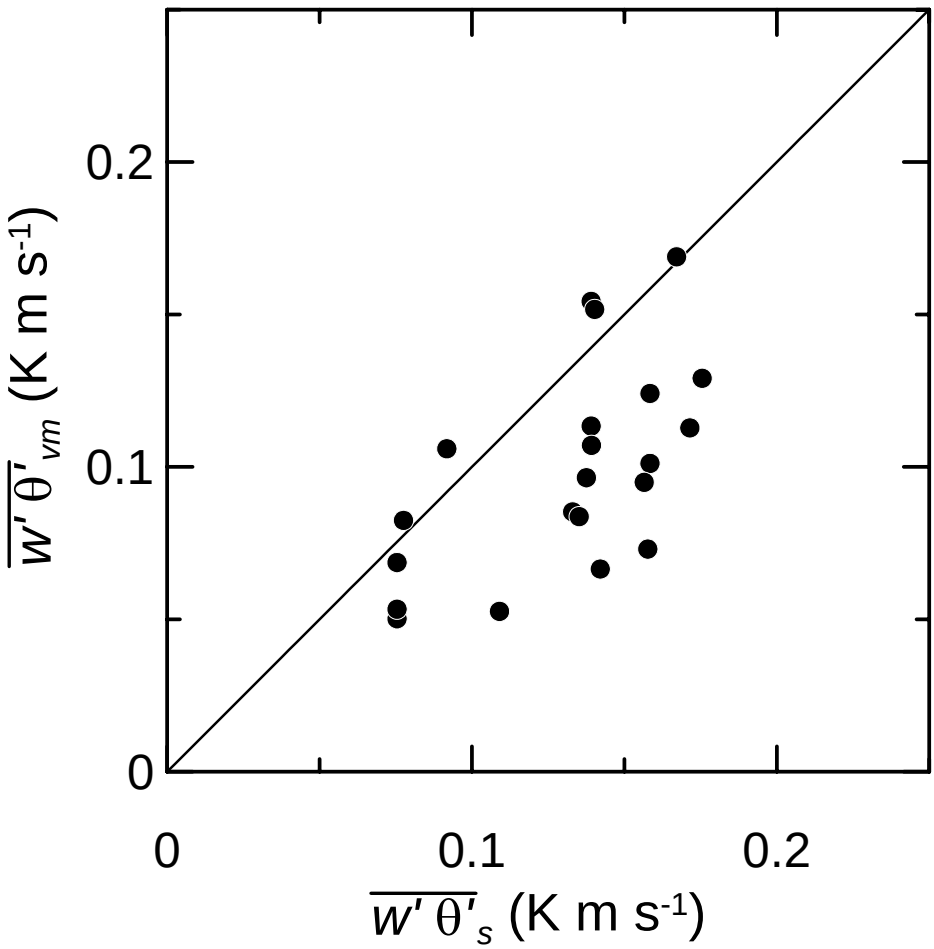

Fig. 4-2g Same as 4-2a but for Eq.(4.4) with velocity scale $v_0 = v_h = v_*$ and entrainment model (3.9), and the data of normalized height $\xi < 0.8$.

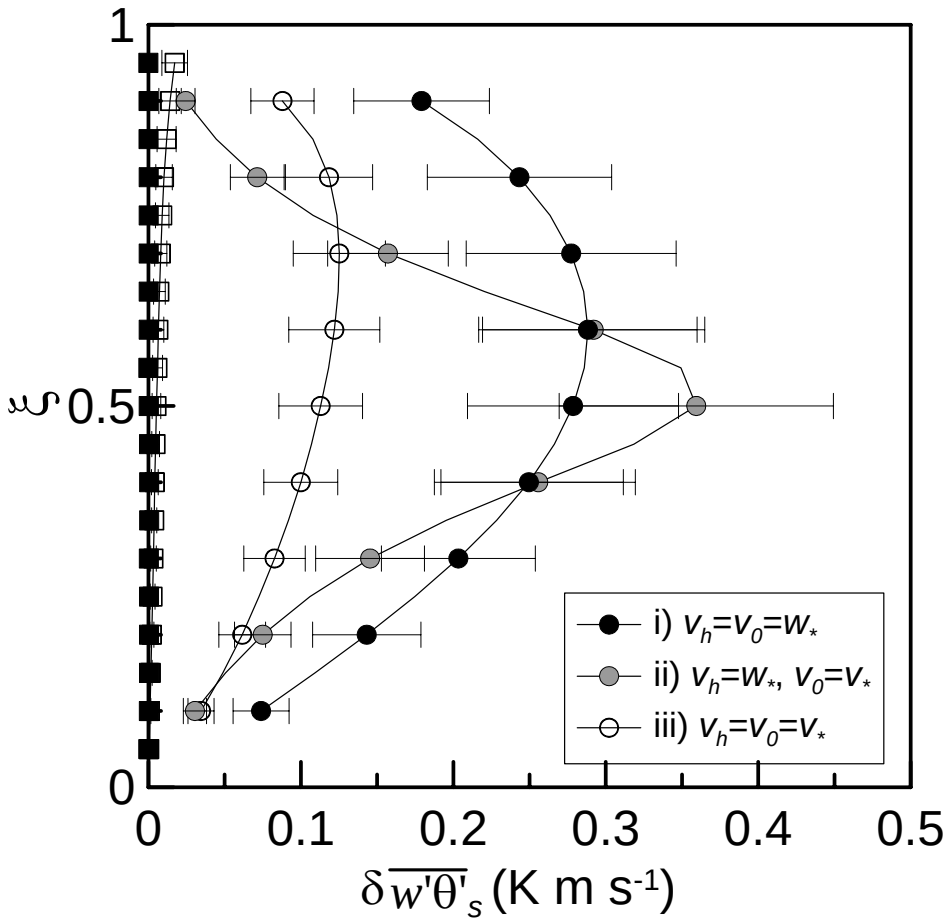

Fig. 4-3a Sensitivity test of the variance methods of Eq. (4.4) with the original constants in the literatures.

The means of absolute changes of $\overline{w'\theta'}_0$ for the σ_θ and u_* are indicated by circles and squares, respectively, with the error bars showing the value of the two cases. The values used in this test is described in the text.

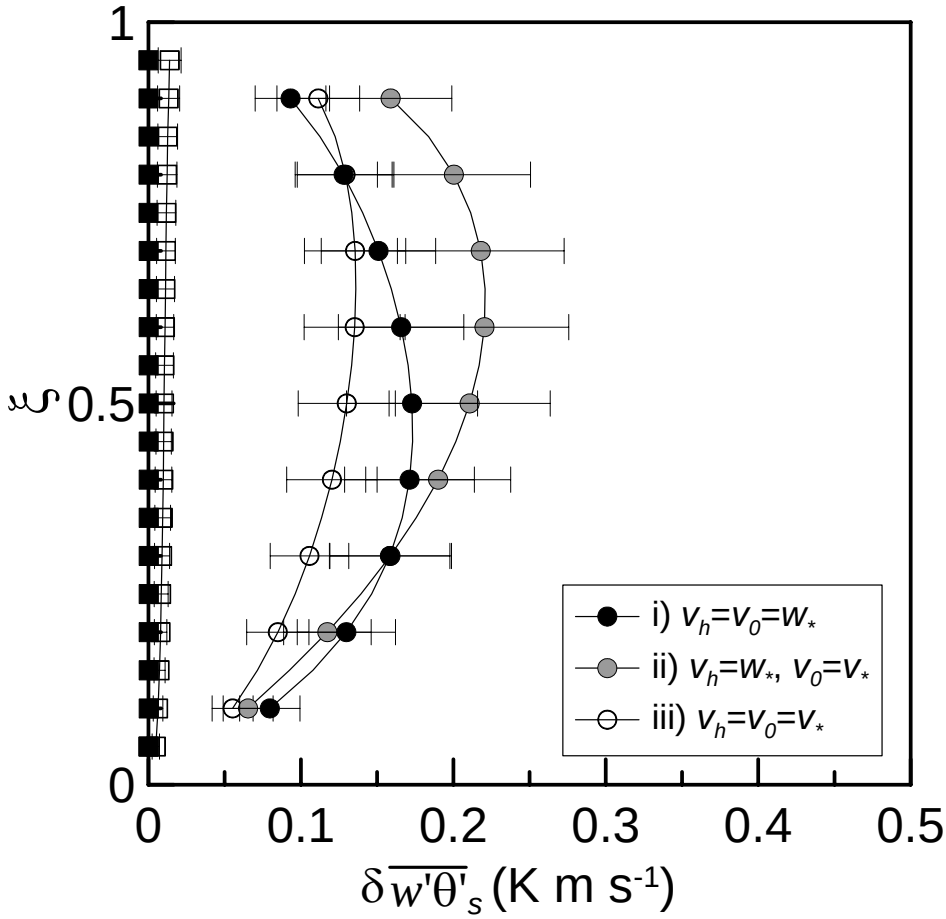

Fig. 4-3b Same as 4-3a but for (4.4) with the calibrated constants.

middle parts of the mixed layer level for the cases ii), while weaker sensitivity for the whole height in the case iii). It is consistent with a tendency of the vertical distributions of rms difference between $\overline{w'\theta'}_{vm}$ and $\overline{w'\theta'}_s$ shown in Fig. 4-4. Under the same conditions, the sensitivity of $\overline{w'\theta'}_{vm}$ to the change of u_* ±0.1 m s^{-1} from 0.25 m s^{-1} was also shown in Figs. 4-3a and 4-3b, in which the effect of changing u_* was smaller in one-order as regarding $\overline{w'\theta'}_s$ than that of σ_θ, and therefore it should be concluded that some large scatter of $\overline{w'\theta'}_{vm}$ was caused mainly not by u_* uncertainty but by the nature of the functional forms themselves.

As can be seen from the figures and Table 4-2, the rms difference was reduced from more than 4×10^{-2} K m s^{-1} to 3-4×10^{-2} K m s^{-1} by adjusting the constants through the calibration. This implies that these experimental constants still contain uncertainty as mentioned above. However, this need for the calibration may have arisen from the 8% underestimation and 3% overestimation of the variance that were caused by the slow response sensor and the white noise, respectively, as mentioned in chapter 2. However, this is not clearly the case as can easily be shown from a simple error analysis of the variance and the flux as follows. The rms difference between σ_θ^2 values from the observations and those predicted by (3.2), (3.3) and (3.10) with the original constants is 1.1-1.9×10^{-2} K^2 with mean value 1.6×10^{-2} K^2. This is order of magnitude larger than that can be accounted for by the measurement error alone, as the 8% underestimation of σ_θ^2 can be translated into the underestimation of 1.0×10^{-3} K^2 and the 3% overestimation of σ_θ^2 into that of 0.5×10^{-3} K^2. Similarly, from the view point of flux evaluation, since $\overline{w'\theta'}_0$ is proportional to $\sigma_\theta^{3/2} = (\sigma_\theta^2)^{3/4}$, the 5% underestimation of σ_θ^2 corresponds to 4% underestimation in flux; this is an order of magnitude smaller than the reduced rms difference of around 30% by the calibration. Thus the measurements error is probably of lesser importance to the fact that the local calibration was necessary.

The data with $z > 0.5h_i$ were also drawn in Figs. 4-1a and 4-2a for Eq. (4.1), even though (4.1) was derived originally only for the lower half of mixed layer. As mentioned, in the calibration and the calculation of the statistics and for the later analyses, only the data obtained below $0.5h_i$ were used. Thus, it is not surprising that even after the calibration of the empirical constants, the outlier points remained. In order to further investigate the outliers, additional calibration with all data for $z < 0.8h_i$ was carried out. It was found that the result is not markedly different from the case with data for $z < 0.5h_i$ (Fig. 4-2b). This tends to indicate

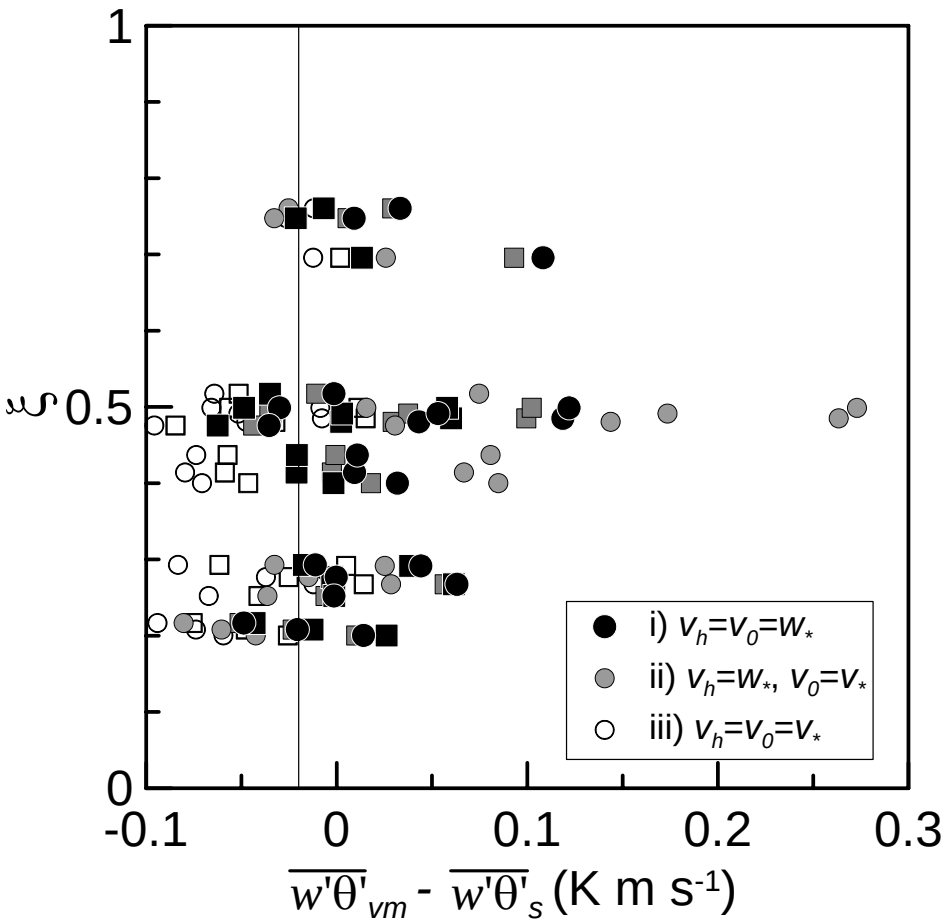

Fig. 4-4 Vertical distribution of difference between estimation by means of (4.4) with different velocity scale and observed flux. $\overline{w'\theta'}_{vm} - \overline{w'\theta'}_s$. Circle and square show usage of original constants and calibrated constants, respectively.

that the estimated flux is not very sensitive to the exact value of σ_θ at higher levels in the mixed layer. However, simple error propagation analysis (see below) has indicated that the sensitivity of fluxes estimated from (4.1) to the error of σ_θ measurement is the lower near the surface and increases as z increases toward h_i. Thus the agreement found for the current data set, and, in general, (4.1) may still be better used for $z < 0.5h_i$.

4-3 Addition of Large Scale Atmospheric Parameters

The scatter that still exists might possibly be reduced by introducing additional parameters. As mentioned before, up to now it has been assumed that the relevant variables for the mixed layer variances are z, h_i and $\overline{w'\theta'}_0$. However, it is quite possible that other variables may play a role. For example, for the study of profiles or bulk formulation for mainly wind speed in the mixed layer, several variables whose effect is not negligible have been identified (e.g., Brutsaert and Mawdsley, 1976). In the same way as them, the variables relevant to temperature profiles can be listed as follows; the Coriolis parameter f, the Ekman height scale $h_r = \kappa u_* f^{-1}$ where κ is a constant, the vertical gradient of geostrophic wind i.e., baroclinicity, $\partial U_g/\partial z$, $\partial V_g/\partial z$, and the horizontal temperature advection $\partial \overline{u}\overline{\theta}/\partial x$, $\partial \overline{v}\overline{\theta}/\partial y$ in which $\overline{u}$ and $\overline{v}$ are wind speed components in the eastward and northward direction, respectively. The vertical gradients of U_g and V_g can be expressed in terms of horizontal gradients of temperature. That is known as the thermal wind relation in a good approximation,

$$\frac{\partial U_g}{\partial z} = -\frac{g}{fT}\frac{\partial T}{\partial y}, \quad \frac{\partial V_g}{\partial z} = \frac{g}{fT}\frac{\partial T}{\partial x} \tag{4.5}$$

These additional variables were evaluated with the outputs of the regional climate model as mentioned before, and detailed procedure is described in Appendix A-3.

These variables can be organized to form several non-dimensional parameters. With three basic dimensions of length, time and temperature and nine independent variables, six independent dimensionless parameters can be created. First one of them is dimensionless

variance $\sigma_\theta^2 T_*^{-2} = \sigma_\theta^2 \left(\overline{w'\theta'}_0\right)^{-2} h_r f\left(h_i L^{-1}\right)^{1/3}$. The others are those by following Brutsaert and Mawdsley (1976), who discussed the variables in relation to the mean profiles of the mixed layer,

$$\xi = z / h_i \tag{4.6}$$

$$\mu = h_i / L \tag{4.7}$$

$$\nu = h_i / h_r \tag{4.8}$$

$$\beta_x = \frac{\partial u_g}{\partial z}\left(\frac{h_i}{h_r}\right)^2 \frac{1}{|f|}, \beta_y = \frac{\partial v_g}{\partial z}\left(\frac{h_i}{h_r}\right)^2 \frac{1}{|f|}, \beta = \left(\beta_x^{\,2} + \beta_y^{\,2}\right)^{1/2} \tag{4.9}$$

In a similar manner, the advection term can be made dimensionless as follows:

$$\gamma_x = \frac{\partial \overline{u}\overline{\theta}}{\partial x}\frac{h_i}{\overline{w'\theta'}_0}, \gamma_y = \frac{\partial \overline{v}\overline{\theta}}{\partial y}\frac{h_i}{\overline{w'\theta'}_0}, \gamma = \left(\gamma_x^{\,2} + \gamma_y^{\,2}\right)^{1/2} \tag{4.10}$$

The dimensionless variables γ and β include two horizontal components, and thus it is possible to treat them either as the combined variable or as independent variables, and both cases were tested in what follows. The actual values of each dimensionless parameter determined for the study area are listed in Table 4-3. For the TDBU formulation, since the inclusion of v_* as scaling parameter resulted in less accurate result as shown above, only the case with w_* scaling, i.e., (3.10), was considered hereafter.

Among those dimensionless variables, ξ had already been included in the variance profile formulations (3.2), (3.3), (3.10) and (3.11). Therefore other four were added in the following equation,

$$\left(\frac{\sigma_\theta}{T_*}\right)^2 = F\left(z / h_i\right) + c_1\mu^{c_2} + c_3\nu^{c_4} + c_5\beta^{c_6} + c_7\gamma^{c_8} + c_9 \tag{4.11}$$

where F is a function of $\xi = z / h_i$, which can be taken as the RHS of one of (3.2), (3.3), (3.10) or

Table 4-3 List of parameters added to variance formulations.

Date (2003)	Segment name	ξ	$\lvert\mu\rvert$	ν	β	β_x	β_y	γ	γ_x	γ_y
July 19	200-KBU500	0.49	529.4	1.1	22.9	22.4	4.4	64.3	28.1	-57.8
	200-KBU200	0.20	552.4	1.1	23.7	23.3	4.6	64.3	28.1	-57.8
July 20	201-KBU200	0.28	218.9	1.3	42.8	33.1	-27.1	38.9	29.3	-25.6
	201-KBU500a	0.76	218.8	1.3	42.8	33.1	-27.1	38.9	29.3	-25.6
	201-KBU500b	0.75	219.0	1.2	42.2	32.7	-26.8	38.9	29.3	-25.6
July 23	204-KBU1000	1.02	109.6	1.0	57.6	45.1	-35.8	122.9	-120.8	-22.8
	204-KBU200	0.21	111.8	1.0	59.4	46.6	-36.9	122.9	-120.8	-22.8
Aug. 23	233-KBU200a	0.29	16.7	0.8	18.3	10.5	14.9	18.7	-18.7	-0.3
	233-KBU200b	0.27	18.7	0.8	17.2	9.9	14.0	15.8	-15.8	-0.3
	233-KBU300	0.50	21.2	0.8	17.0	9.8	13.9	13.3	-13.3	-0.2
Aug. 24	234-KBU1000	0.99	18.9	0.9	50.4	30.1	-40.4	68.8	1.3	-68.7
	234-KBU500b	0.52	19.7	0.9	49.2	29.4	-39.5	65.0	1.3	-65.0
	234-KBU200	0.25	19.9	0.8	48.6	29.1	-39.0	63.9	1.2	-63.8
Aug. 25	235-KBU1000	0.94	28.8	1.2	141.3	125.2	-65.7	63.1	-42.1	46.9
	235-KBU500a	0.48	28.8	1.2	142.1	125.8	-66.0	63.4	-42.4	47.2
	235-KBU500b	0.50	28.8	1.2	140.9	124.8	-65.4	62.9	-42.0	46.8
	235-KBU200	0.22	29.1	1.2	139.8	123.8	-64.9	62.1	-41.5	46.2
Oct. 2	276-KBU1000	0.70	62.9	1.4	37.6	25.9	-27.2	15.1	14.9	-2.6
	276-KBU500a	0.41	64.0	1.4	37.3	25.7	-27.0	14.7	14.5	-2.5
	276-KBU500c	0.40	65.5	1.4	37.0	25.6	-26.8	14.4	14.2	-2.4
Oct. 3	277-KBU1000	0.82	62.4	1.1	89.6	76.9	-46.0	46.0	-19.5	-41.6
	277-KBU500a	0.44	60.6	1.2	91.0	78.1	-46.7	47.9	-20.4	-43.3
	277-KBU500b	0.49	60.4	1.2	90.1	77.4	-46.3	47.9	-20.4	-43.3
	277-KBU500c	0.48	60.6	1.2	90.7	77.9	-46.6	48.1	-20.4	-43.5
	277-KBU200	0.29	60.1	1.2	90.7	77.8	-46.5	48.5	-20.6	-43.9

The additional parameters, ξ, μ, ν, β and γ are expressed as Eqs. (4.6), (4.7), (4.8), (4.9) and (4.10), respectively.

(3.11). The equation can be rewritten for $\overline{w'\theta'}_0$ as

$$\overline{w'\theta'}_0 = \sigma_\theta^{3/2}\left(\frac{g}{\theta}h_i\right)^{1/2}\left[F\left(z/h_i\right)+c_1\mu^{c_2}+c_3\nu^{c_4}+c_5\beta^{c_6}+c_7\gamma^{c_8}+c_9\right]^{-3/4} \tag{4.12}$$

and the coefficients c_1 through c_9 were determined to minimize the rms difference between $\overline{w'\theta'}_0$ and $\overline{w'\theta'}_s$. Note that when γ is considered, the equation becomes implicit, and thus iteration is required to determine $\overline{w'\theta'}_0$. This was carried out in the same manner to solve (4.4); an initial value of $\overline{w'\theta'}_0 = \overline{w'\theta'}_s$ was first inserted into the RHS of (4.12), and the resulting value of $\overline{w'\theta'}_0$ from (4.12) was again inserted into the RHS of that. This was repeated until the value of $\overline{w'\theta'}_0$ had sufficiently been converged. As is the case of (4.4), the final value is not sensitive to the choice of the initial value. Note also that possible other functional forms were also tested since there is no *a priori* reason that these additional non-dimensional variables should be organized as a linear function. Although Crago and Brutsaert (1995) formulate the bulk similarity functions for mean wind speed of ABL as linear equation of baroclinicity and acceleration parameters on the basis of ideas by Arya and Wyngaard (1975), Garrat et al. (1982) and Joffre (1985), there is not a theory or a study that helps to organize a proper functional form for second order statistics, some arbitrary forms were tested, that included a product of the variables and a linear function of logarithm of these variables, among some others. However, the result was not very different from the one obtained by (4.12) and thus only the result with (4.12) will be shown. It is not clear if this is because the number of the data points is not sufficient to produce meaningful difference among the different functional forms or the process of the calibration took care of the difference of the formulation.

The results are shown in Figs. 4-5a to 4-5e and in Tables 4-1 and 4-2. It is evident that the inclusion of the additional parameters successfully reduced the rms difference. To investigate which parameter(s) have more contribution for the improvement of accuracy of the flux estimation, all possible combinations of the parameters were tested, and this result is given in Figs. 4-6a to 4-6c. It can be seen that in general the rms difference decreases as the number of parameters increases. In the case of addition of one parameter, β (and especially their y

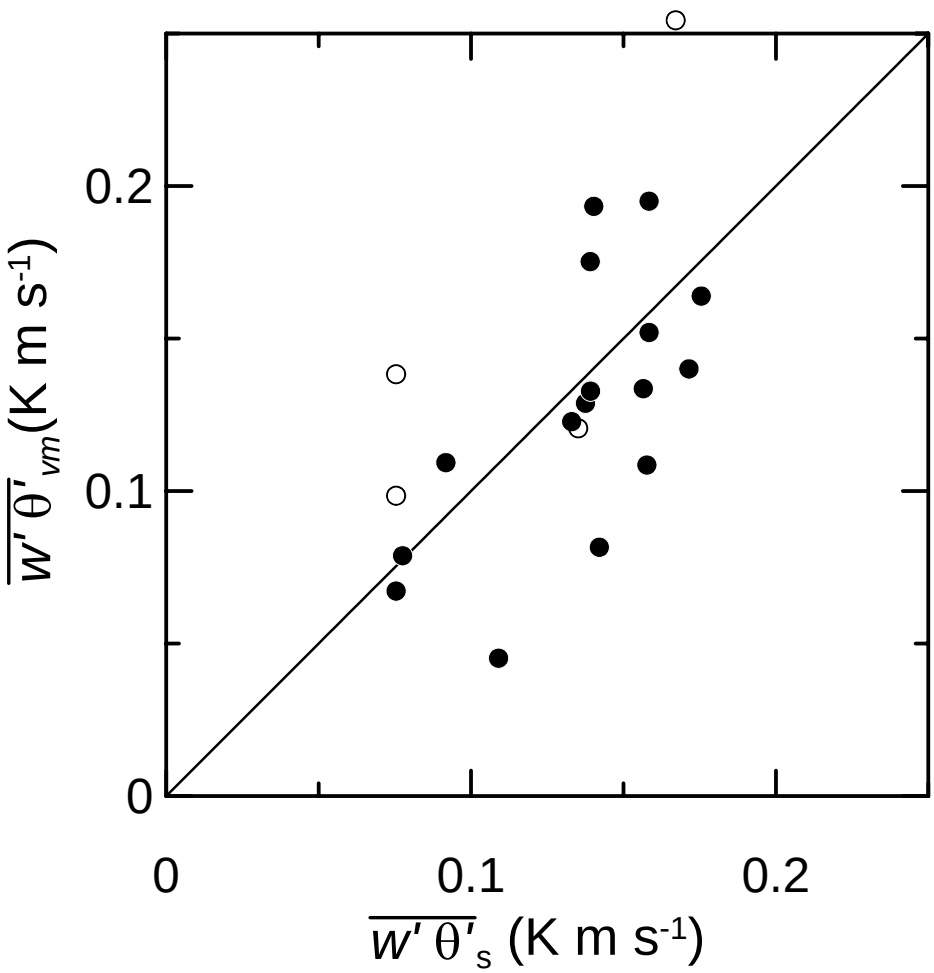

Fig. 4-5a Comparison between the sensible heat flux $\overline{w'\theta'}_{vm}$ estimated from Eq.(4.1) with calibrated constants and additional dimensionless parameters and $\overline{w'\theta'}_s$ observed by eddy covariance method at the the KBU flux station.

Solid and open circle show the data for normalized height $\xi < 0.5$ and $0.5 \leq \xi < 0.8$, respectively. (Calibration and parameters addition was carried out for the data of $\xi < 0.5$)

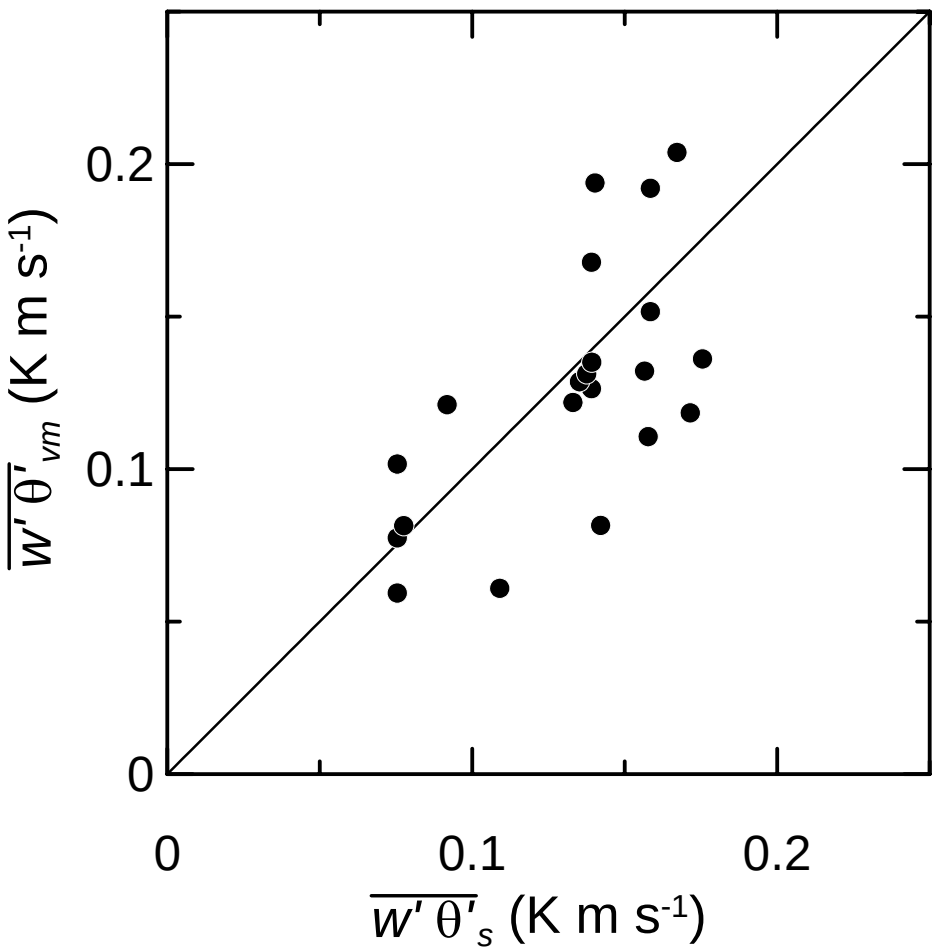

Fig. 4-5b Same as 4-5a but for Eq.(4.1) and the data of normalized height $\xi < 0.8$ (Calibration and parameters addition was carried out for the data of $\xi < 0.8$)

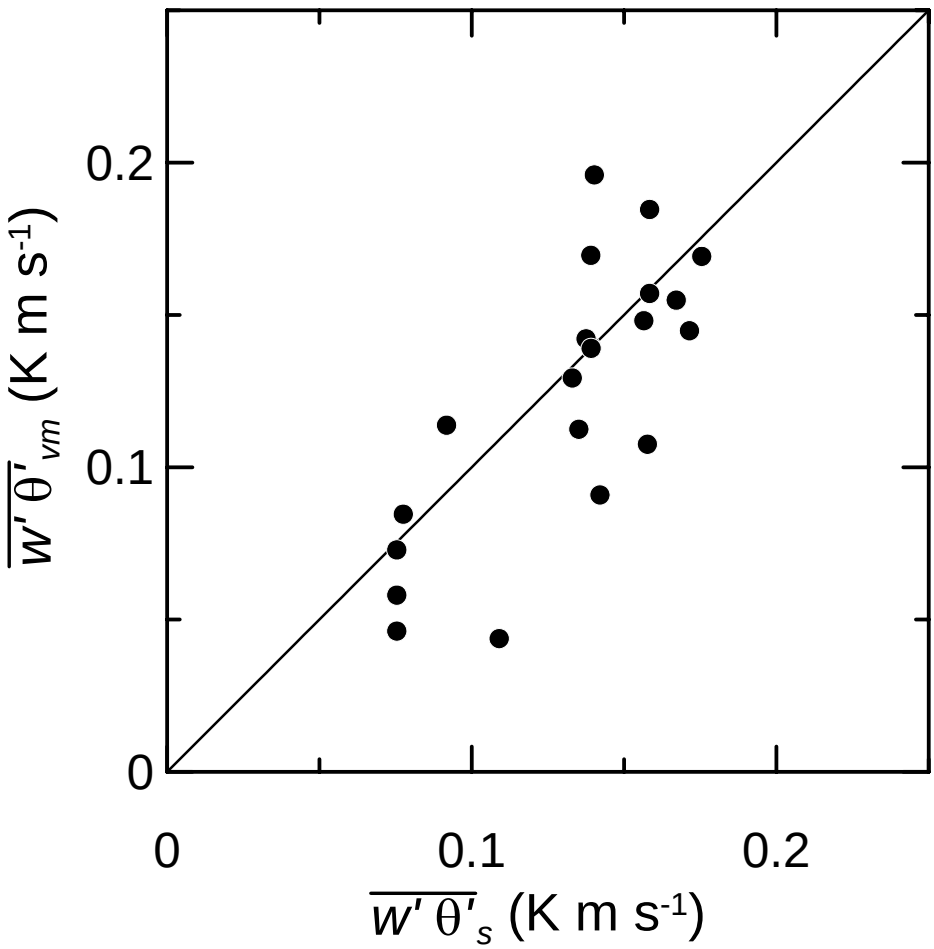

Fig. 4-5c Same as 4-5a but for Eq.(4.2) and the data of normalized height $\xi < 0.8$.

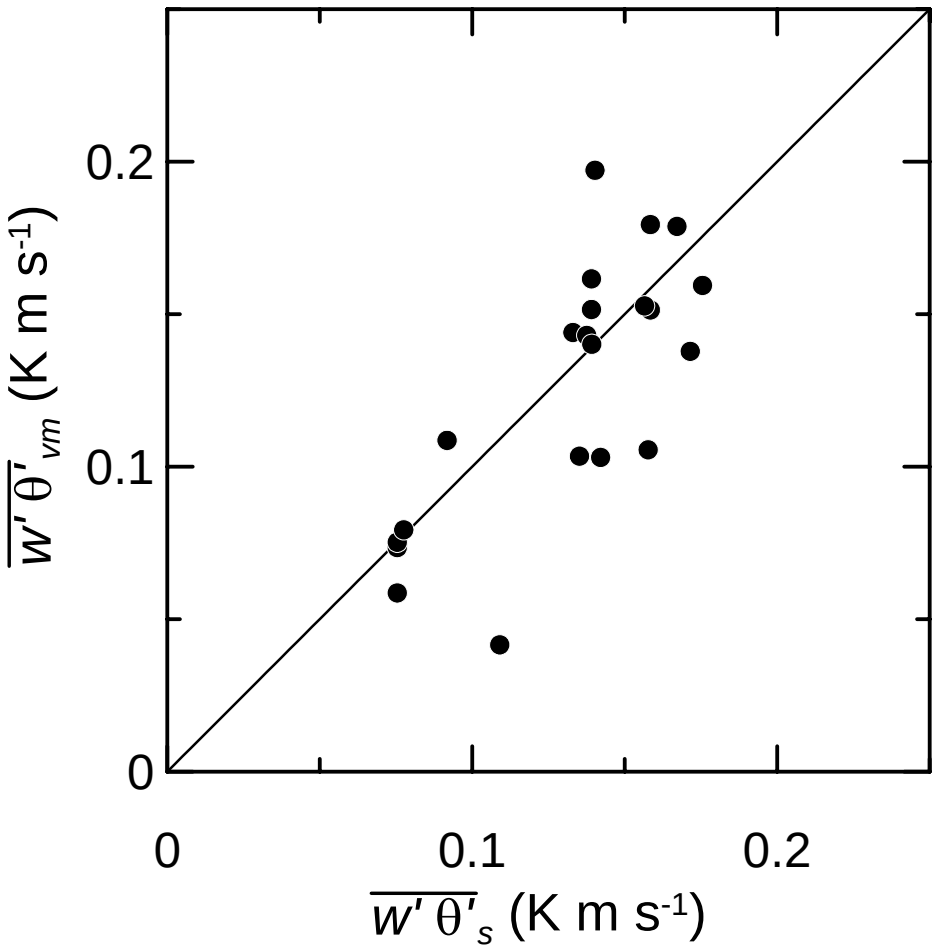

Fig. 4-5d Same as 4-5a but for Eq.(4.3) and the data of normalized height $\xi < 0.8$.

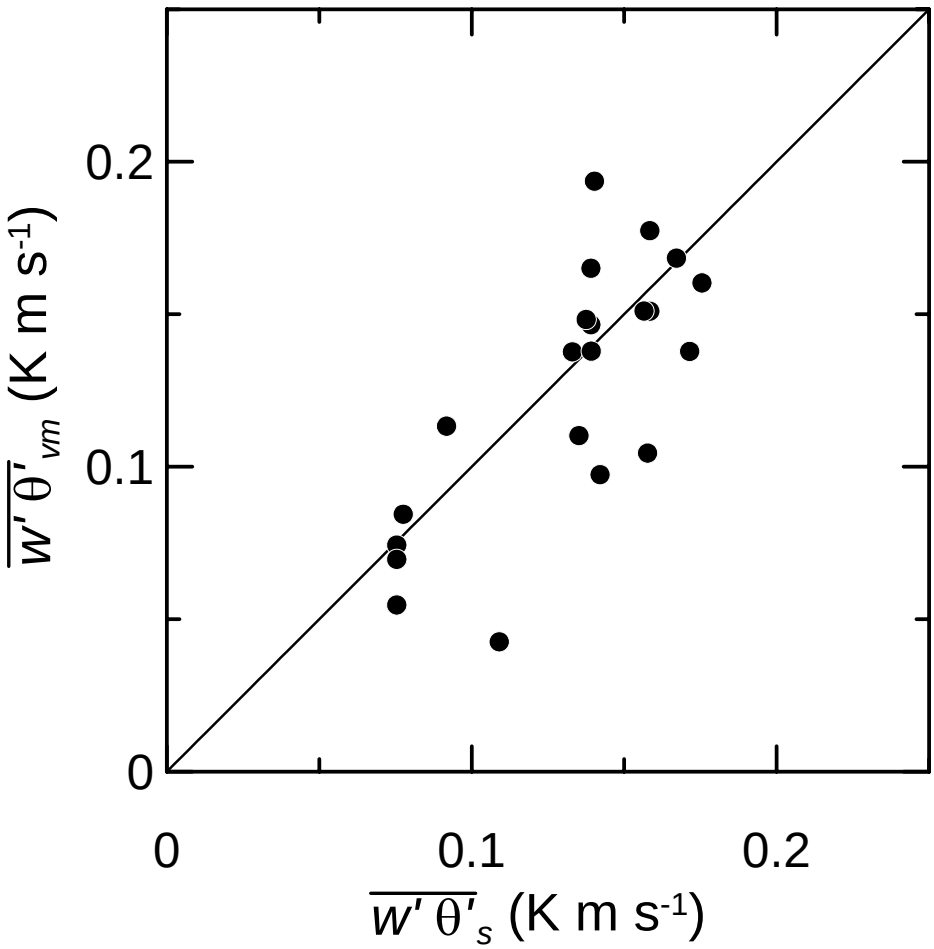

Fig. 4-5e Same as 4-5a but for Eq.(4.4) with velocity scale $v_0 = v_h = w_*$ and entrainment model (3.4), and the data of normalized height $\xi < 0.8$.

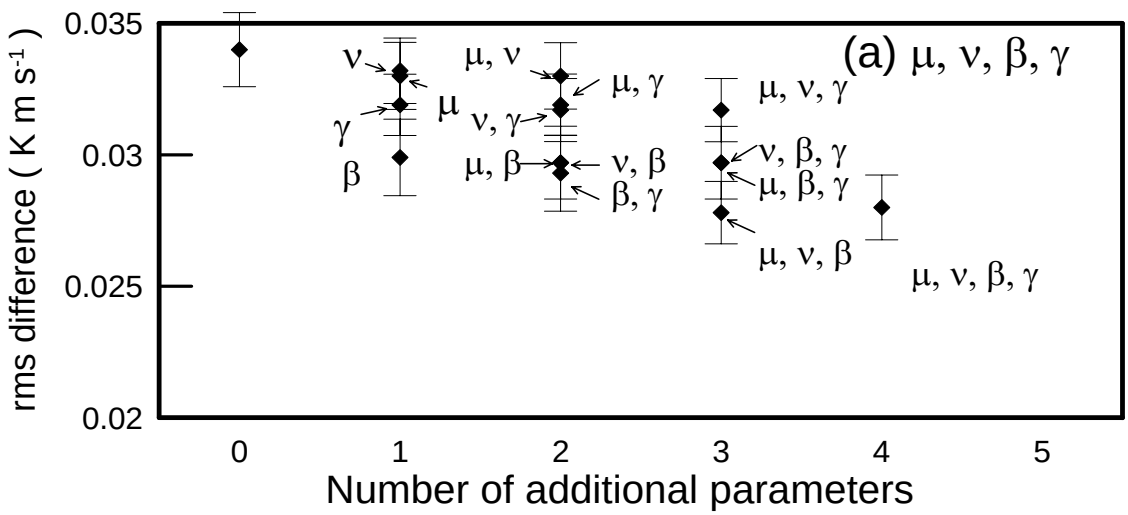

Fig. 4-6a Number of additional dimensionless parameters and resulted rms (root mean square) difference between $\overline{w'\theta'}_s$ derived from eddy covariance method at the KBU flux station and $\overline{w'\theta'}_{vm}$ estimated by the variance methods (4.4) with velocity scale $v_0 = v_h = w_*$ and entrainment model (3.4).

Added parameters are μ, ν, β and γ, which are given in Table 4-3.

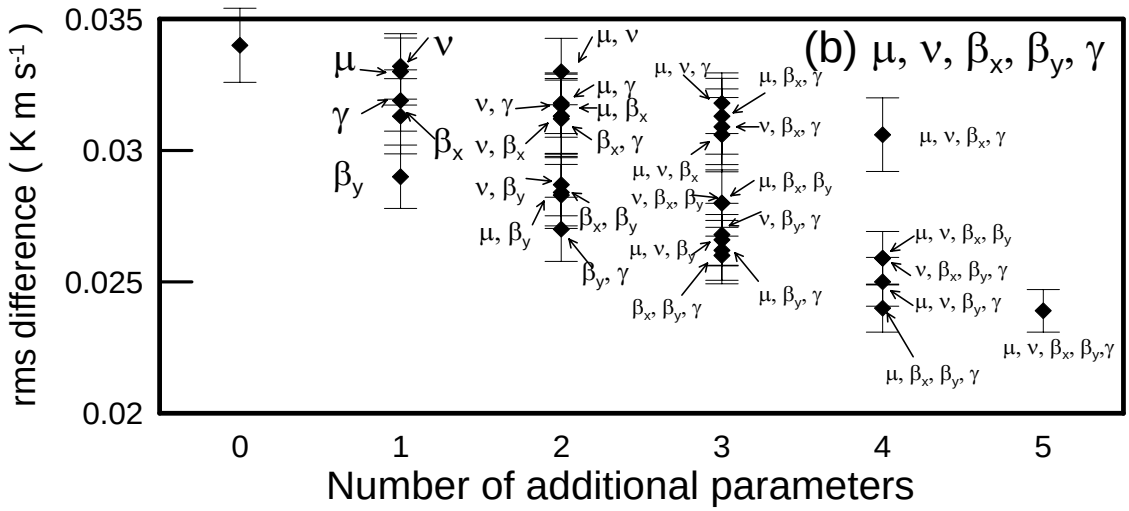

Fig. 4-6b Same as 4-6a but for parameters μ, ν, β_x, β_y and γ, which are given in Table 4-3.

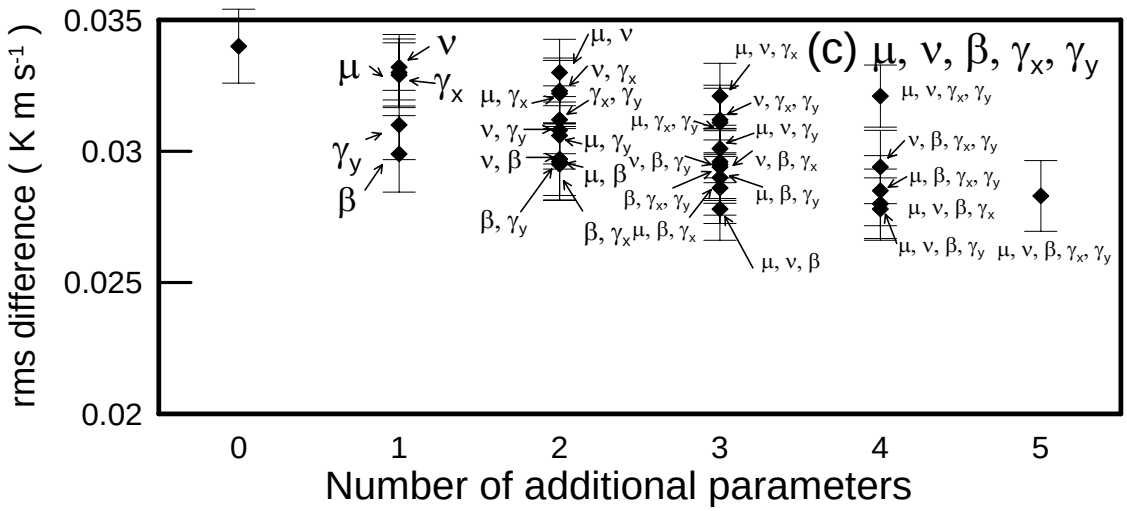

Fig. 4-6c Same as 4-6a but for parameters μ, ν, β, γ_x and γ_y, which are given in Table 4-3.

component) are slightly more effective to reduce the rms difference than the others, although the difference is not statistically significant at 5% level. The difference became less significant with increasing number of additional parameters. It was also found that the rms difference of the fluxes with (4.9) and (4.10) for the separate treatment of the x- and y-component and for the combined expressions, which are differed by only a few W m^{-2}. This is probably because the horizontal gradient of the wind and temperature fields in the atmosphere around the experimental area are more or less the same during the flights and thus it is the magnitude and not the direction of β that counted. Naturally in different settings, it is quite possible that the separate treatment works better. On the other hand, effects of the other parameter were not clear, which is partly because baroclinicity or advection tends to make unclear the dependence on these parameters, especially stability parameter μ (Tennekes, 1982).

4-4 Validity of the Variance Methods

As a whole, the rms differences reduced to about 3×10^{-2} - 4×10^{-2} K m s^{-1} which roughly correspond to H = 30 to 40 W m^{-2}, after the calibration of the constants, and further down to 3×10^{-2} K m s^{-1} (H = 30 W m^{-2}) or less with the introduction of the additional dimensionless parameters. The reduction of the rms error from the result with the original formulations to that with (4.12) was found statistically significant at 5% confidence level except for (3.2), for which it is significant only at 10% level. The difference among the results with different formulation of (3.2), (3.3), (3.10) and (3.11) with w_* scaling was not found significant even at the 10% level. In another word, the same level of agreement was obtained by all formulations. This is partly due to the fact that a local calibration was applied. Thus as long as the calibration is possible, the simplest form, i.e., (4.12) with (3.11) that covers the whole mixed layer may be a better choice from the practical point of view. For the application of the mixed layer variance methods without calibration, the next step would be to test (4.12) with multiple data sets, to assess whether or not the inclusion of additional variables reduced or eliminated the need of calibration.

To investigate the cause of remained deviation of the estimated fluxes from the reference

value, a simple error analysis was carried out. These variance equations contain variable parameters such as temperature variance, the normalized mixed layer height, and some large-scale atmospheric conditions, which affect the flux estimation. The scatter in the estimation error (relative to the reference flux) can be assessed with an error propagation equation for the variance methods expressed as,

$$\delta\overline{w'\theta'}_0 = \left[\left(\frac{\partial\overline{w'\theta'}_0}{\partial\sigma_\theta}\delta\sigma_\theta\right)^2 + \left(\frac{\partial\overline{w'\theta'}_0}{\partial\xi}\delta\xi\right)^2 + \left(\frac{\partial\overline{w'\theta'}_0}{\partial P}\delta P\right)^2 + \cdots\right]^{1/2} \tag{4.13}$$

where the symbol δ presents the absolute error, and P indicates group of additional parameter, which means the sum of the second through sixth term of (4.11). Those results for (4.12) with (3.2), (3.3), case i) of (3.10) and (3.11) for θ = 300 K, σ_θ = 0.15 K, h_i = 1000 m, P = 0.5, $\delta\sigma_\theta$ = 0.1 K, $\delta\xi$ = 0.1 and δP = 0.5 are plotted against ξ in Fig. 4-7. The value of $\frac{\partial\overline{w'\theta'}_0}{\partial\sigma_\theta}\delta\sigma_\theta$ is found larger in one to two-order than the other terms, and thus the terms except for $\delta\sigma_\theta$ were neglected as the source of the flux error. Since variance methods of (3.7) with the scaling velocity v_* are expressed as implicit function of $\delta\overline{w'\theta'}_0$, they cannot be subjected to the simple error analysis described above. Thus, an alternative sensitivity test was attempted as described in the previous section, in which it was found that the contribution of δu_* to $\delta\overline{w'\theta'}_0$ can be neglected compared to that of $\delta\sigma_\theta$, and $\delta\overline{w'\theta'}_0$ becomes larger at the middle part of the mixed layer for the case with $v_0 = v_*$, $v_h = w_*$ (Figs. 4-3a and 4-3b). It can be seen from Fig. 4-7 that the possible error is as large as 0.1-0.2 K m s^{-1} for the above condition and has the maximum at around ξ = 0.5 for (4.12) with (3.3), (3.10) and (3.11), and at ξ = 1.0 for (4.12) with (3.2), and thus it is possible that measurement error of σ_θ observed near the mid altitude contributed partly the remaining rms difference. In the future application, it can be recommended that the observation should be made in the height around in ξ = 0.2-0.3 and ξ = 0.7-0.8, for the case but (3.2), to obtain results with smaller errors for the same type of instruments, although in practice it is not necessarily easy to know the exact value of h_i and hence ξ during flights. Note also that Fig. 4-7 indicates that the magnitude of error of each equation is about the same except for (4.12) with (3.2), and thus, from the viewpoint of error reduction, there is not an advantage to choose a

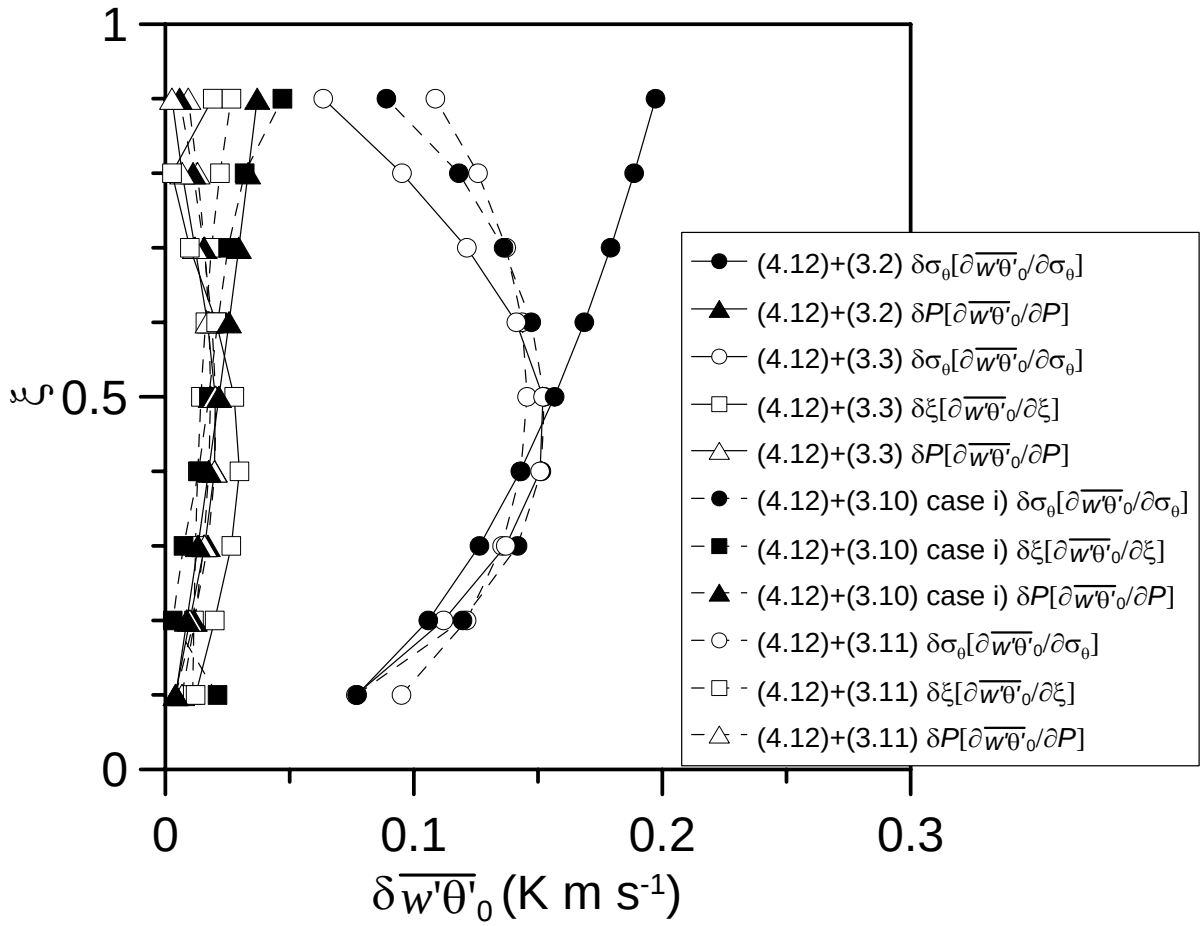

Fig. 4-7 Error propagation analysis for the variance methods.
The values used in this test is described in the text.

particular formulation.

From another viewpoint, the resultant rms difference with the calibrated constants is about the same as that reported by Sugita and Kawakubo (2003) with the data analysis observed from the meteorological tower. One can assume that the tower measurements are more stable and reliable than the aircraft measurements. The fact that both data sets produced similar statistics indicates the general robustness of the variance methods, and that the scalar variable is not susceptible to serious measurement error due to the aircraft platform instability even with a simple sensor setting employed in the present observations.

Finally, in this study, the calibration of the coefficients in the variance equations was carried out to fit the estimated fluxes to the ground based measurements, while the previous researches determined the constants to optimize variance values. With derived constants in this study, relations between estimated dimensionless variance and that obtained by aircraft observations normalized with ground observed fluxes are shown in Figs. 4-8a to 4-8d by means of (3.2), (3.3), (3.10) and (3.11), respectively. In contrast to Figs. 3-10a to 3-10d, the effect of flux-optimized calibration appears small and these results are summarized in Table 4-4. The rms difference between the estimation and observation reduced for (3.2) and (3.10) but remained nearly the same for (3.3). That value for (3.11) increased since the constants of (3.11) were determined by fitting the variance. Constants calibrations for optimizing flux estimation were found not to change the results of the variance evaluation. On the other hand, Eq. (3.11) was first calibrated to fit to the observed variance profile, and in the next step, to the flux. The flux estimation results for both the case are found essentially the same.

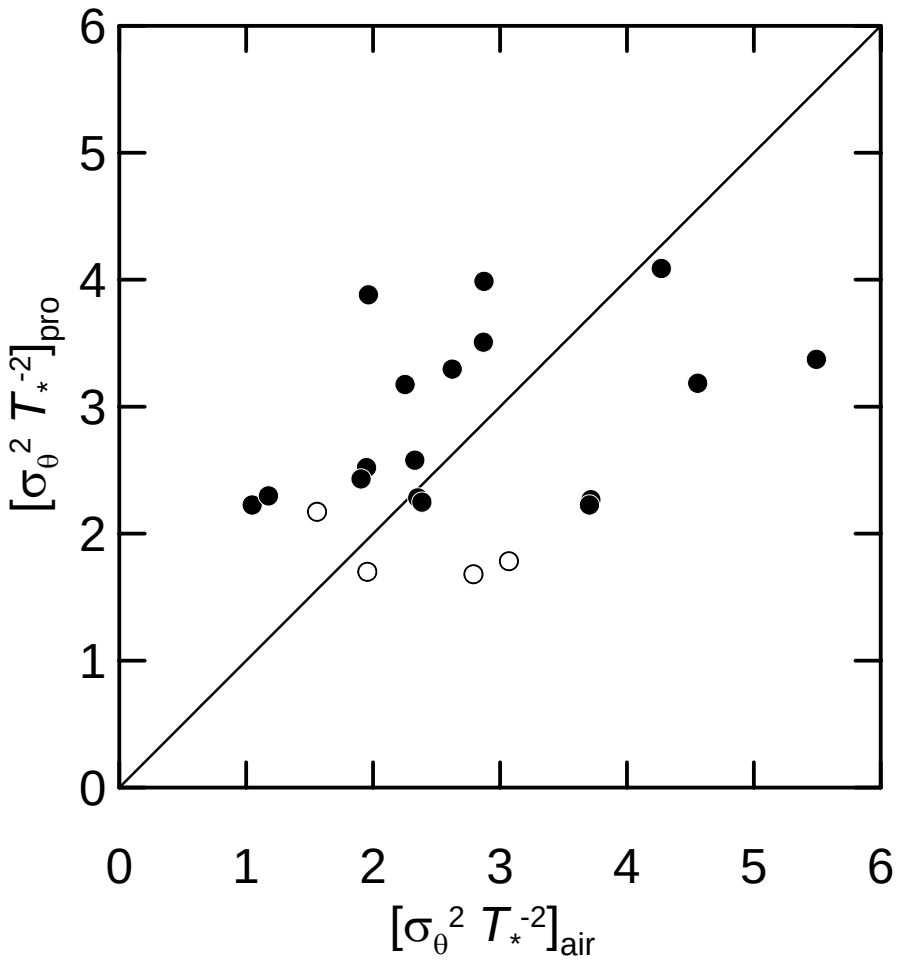

Fig. 4-8a Comparison between the normalized variance of potential temperature $[\sigma_\theta^2 T_*^{-2}]_{pro}$ estimated from Eq.(3.2) with calibrated constants and $[\sigma_\theta^2 T_*^{-2}]_{air}$ that of observed above the KBU area. Solid and open circle show the data for normalized height $\xi < 0.5$ and $\xi < 0.8$ respectively.

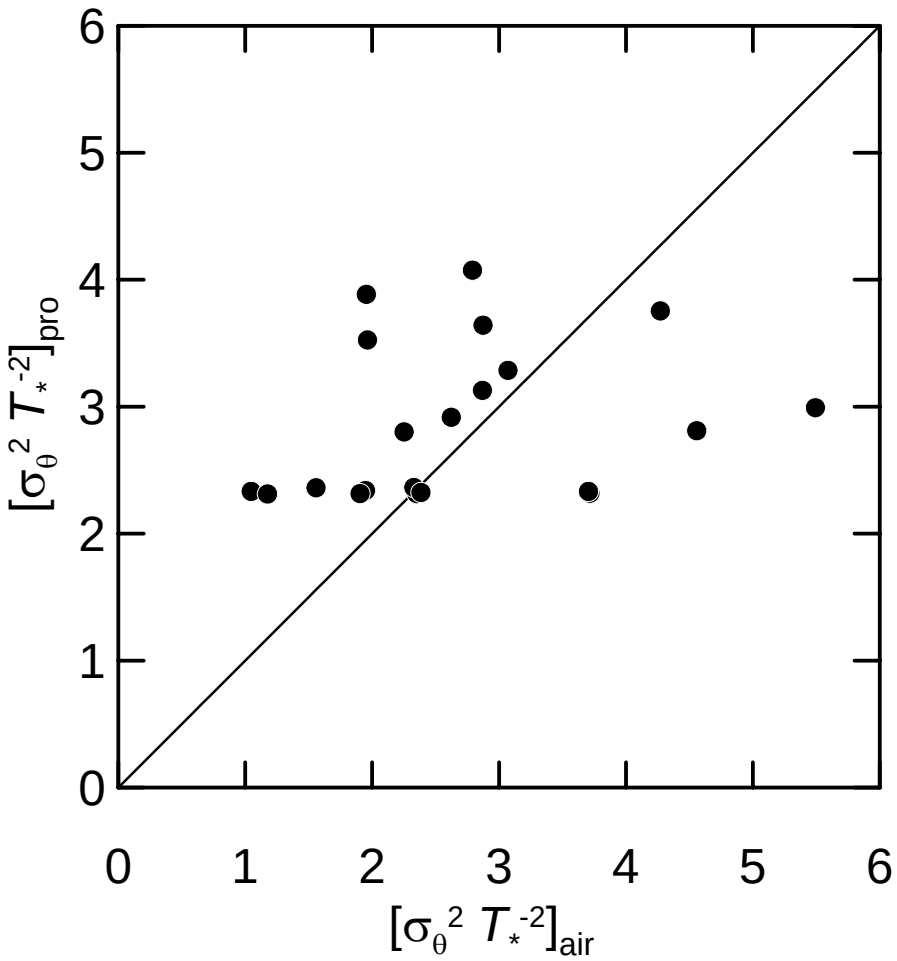

Fig. 4-8b Same as 4-8a but for Eq.(3.3) and the data of normalized height $\xi < 0.8$.

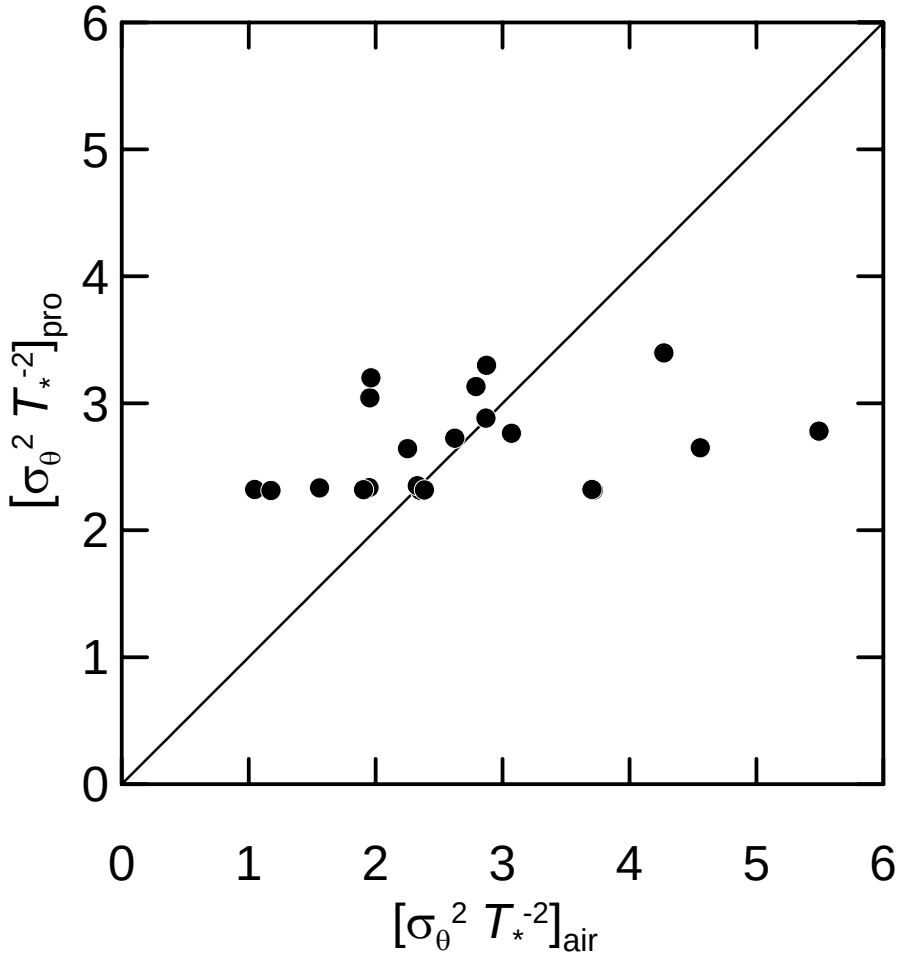

Fig. 4-8c Same as 4-8a but for Eq.(3.10) and the data of normalized height $\xi < 0.8$.

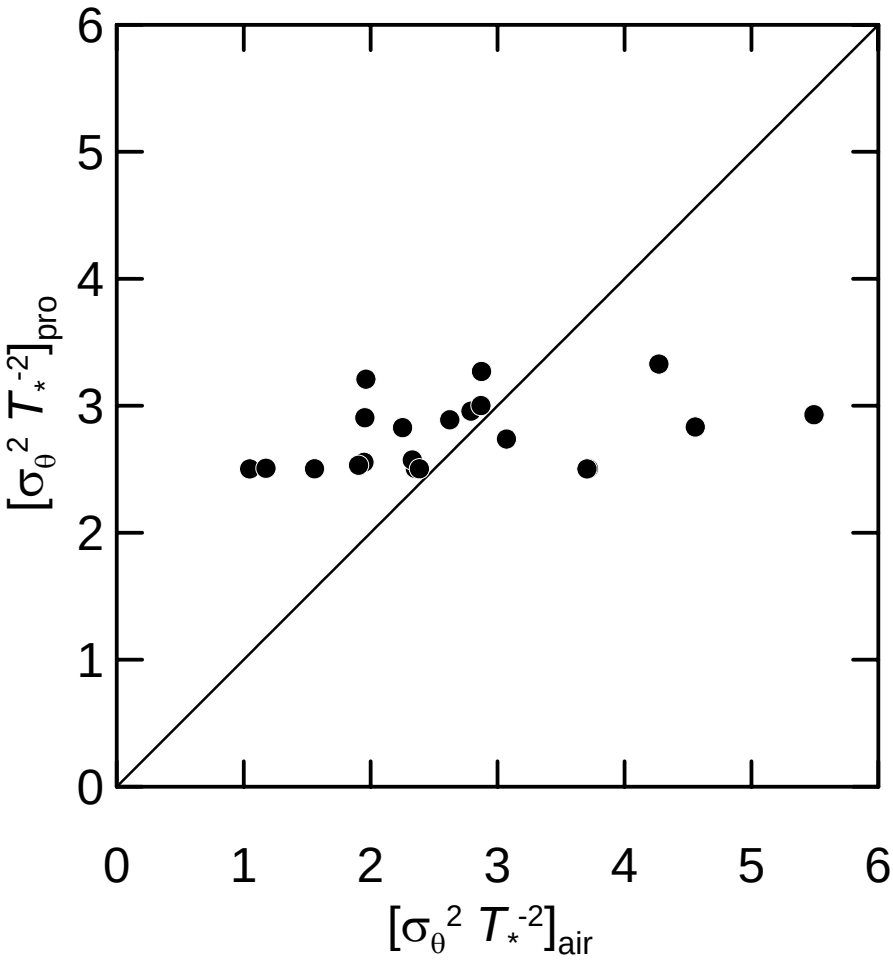

Fig. 4-8d Same as 4-8a but for Eq.(3.11) and the data of normalized height $\xi < 0.8$.

Table 4-4 Statistics in the comparison of flux, $[\sigma_\theta^2 T_*^{-2}]_{air}$ derived form the aircraft observations, and $[\sigma_\theta^2 T_*^{-2}]_{pro}$ estimated by the variance formulations.

variance formulation	z/h_i	N	rms difference	a	b	d	$[\sigma_\theta^2 T_*^{-2}]_{pro}/[\sigma_\theta^2 T_*^{-2}]_{air}$
(3.2) Kaimal et al. (1976)	<0.5	17	1.49	2.97	0.28	0.53	1.34
(3.2) C/C	<0.5	17	1.10	2.31	0.22	0.58	0.44
(3.3) Sorbjan (1989)	<0.8	21	1.11	1.72	0.33	0.64	0.96
(3.3) C/C	<0.8	21	1.11	2.49	0.14	0.47	1.06
(3.9) MW84	<0.8	21	1.17	1.49	0.25	0.58	0.81
(3.9) C/C	<0.8	21	1.04	2.37	0.11	0.42	0.98
(3.10)	<0.8	21	1.01	2.24	0.16	0.51	0.98
(3.10) C/C	<0.8	21	1.03	2.52	0.09	0.37	1.02

MW84: Moeng and Wyngaard (1984), C/C: Coefficients calibrated to optimize flux estimation in this study, *N*: number of data, rms: root mean square, *a*: intercept of regression line, *b*: slope of regression line ($[\sigma_\theta^2 T_*^{-2}]_{pro} = a + b[\sigma_\theta^2 T_*^{-2}]_{air}$), $[\sigma_\theta^2 T_*^{-2}]_{pro}$: normalized temperature variance predicted by variance profile equation $[\sigma_\theta^2 T_*^{-2}]_{air}$: aircraft observation variance normalized with convective temperature scale (including surface heat flux $\overline{w'\theta'}_s$), *d*: index of agreement (Willmott, 1981), $[\sigma_\theta^2 T_*^{-2}]_{pro} / [\sigma_\theta^2 T_*^{-2}]_{air}$: ratio of the mean $[\sigma_\theta^2 T_*^{-2}]_{pro}$ and $[\sigma_\theta^2 T_*^{-2}]_{air}$.

5 Remaining Issues of Mixed Layer Variance Methods

5-1 Observation Uncertainty in This Study

As presented in chapter 4, the estimation of the surface heat fluxes with the variance methods shows decreased deviation from the referenced values through the process of constants calibration and parameter additions. The resulting rms error was converged to some specific values around 30 W m^{-2} regardless of the equation form. This fact indicates that there are some limitations for refining accuracy of the variance similarity law. One of the possible reasons is the propagated error originated in the error of variables in the variance formulation as discussed in previous chapter. The other reasons stem from the observation data of both temperature variances by aircraft aboard instrument and the referenced surface fluxes at the ground station. These issues will be discussed in what follows.

5-1-1 Variance Observations by Aircraft

One of the possible and perhaps the most important causes for uncertainty of the flux estimation by the variance methods is the accuracy of measured temperature variance as found in the previous chapter. Although the accuracy of measurements and recording instruments is of course critical to the results and their improvements of the sensors are needed, there remains sampling problem, which includes issues of, mainly, sampling ratio and averaging length (time), which has direct influence to sampling error. Lenschow et al. (1994) separate the systematic error from the random error for higher moment of single variables (i.e., variance, skewness and kurtosis) and two variables (covariance). Hereafter, their notation with time in Lenschow et al. (1994) is rewritten as that with length for convenience to test the aircraft data.

The systematic error explains the underestimates caused by short data record which is missing the larger scale fluctuations that may contribute the turbulence transport. In other

words, it is the difference between the true, theoretical variance σ_θ^2 obtained by taking infinite observation length and the ensemble average of sampled σ_θ^2 for the averaging length L_{θ^2}, i.e., $\left\langle \sigma_\theta^2 \left(L_{\theta^2} \right) \right\rangle$ and expressed as

$$\frac{\sigma_\theta^2 - \left\langle \sigma_\theta^2 \left(L_{\theta^2} \right) \right\rangle}{\sigma_\theta^2} \approx 2 \frac{\lambda_{\theta^2}}{L_{\theta^2}} \tag{5.1}$$

in which < > indicates the ensemble average, λ_{θ^2} is the integral length scale of σ_θ^2. Similarly, the random error is the difference between σ_θ^2 evaluated for L_{θ^2} and its ensemble average $\left\langle \sigma_\theta^2 \left(L_{\theta^2} \right) \right\rangle$, and can be expressed by,

$$\frac{\left\langle \left| \sigma_\theta^2 \left(L_{\theta^2} \right) - \left\langle \sigma_\theta^2 \left(L_{\theta^2} \right) \right\rangle \right| \right\rangle}{\sigma_\theta^2} \approx \left[a_{RE} \frac{\lambda_{\theta^2}}{L_{\theta^2}} \right]^{1/2} \tag{5.2}$$

where a_{RE} is coefficient equal to 2 for Gaussian process but the value of 4.1 was derived for the realistic skewed process (Lenschow et al., 1994). Both errors can easily be determined once λ_{θ^2} has been known. This was estimated by an empirical function given by Lenschow and Stankov (1986),

$$\lambda_{\theta^2} = h_i \xi^{1/2}. \tag{5.3}$$

For the present flight segments, they produce values in the range from 8% to 31% with the average 16% for the systematic error and 40% to 70% with the average of 55% for the random error for estimating σ_θ^2. To suppress an underestimation due to these errors down to a level of 10%, it is required that the flight segments satisfies $L_{\theta^2} \geq 14$ km and $L_{\theta^2} \geq 295$ km with h_i = 1000 m and z = 500 m for the systematic and random error, respectively. In practice, although it is not easy to satisfy such requirements, it is a good idea to make sequential flights over the

same track at the same level to increase L_{θ^2} and reduce the sampling error (Sun and Mahrt, 1994).

Additionally, the measurements in the mixed layer bring another factors to be considered; the large scatter mainly due to contribution of the mesoscale variations, possible organization of the convective eddies or the effects of horizontally inhomogeneous surface on distribution and sizes of the convective eddies (Mann and Lenschow, 1994). Treatment of these relatively large-scale effects would have influence to systematic error. Considering of these points, an arrangement of the aircraft flight pattern can be one of the possibilities to reduce an uncertainty of the measurements. Santoso and Stull (1999) tested a variety of flight pattern in comparison of measurement and synthetic data consisting of coherent thermal structures and random small-scale turbulence with background profiles of mean variables, and tested a repeating slant ascent and decent leg to minimize scatter of line-averaged statistics for the lower part of the mixed layer. Similarly, Vihma and Kottmeier (2000) derive an optimising flight pattern to minimize difference between the true variance and sample variance of a quantity of interest (unexplained variance), with mesoscale flows evaluated by numerical model for the case of horizontal contrasting see-ice boundary zone, and found that the optimal flight patterns depend on the unexplained variance of fluxes itself.

5-1-2 Surface Fluxes Observations at the Ground Station

The observed surface fluxes used as referenced value to the estimation have also some issues to be considered. As shown in the description of ground observation in chapter 2, the sensible and latent heat fluxes at the surface were obtained by eddy covariance method. One of the problems found by the independent measurements of surface fluxes is the lack of energy balance closure (e.g., Mahrt, 1998; Twine et al, 2000). Sometimes, the accuracy of the measurements can be assessed with energy balance closure $D_{EB}=(H+LE)/(R_n+G)$. This value varies from 0.7 to 1.0 for the several observation results (Willson et al., 2000), and if $D_{EB}<0.7$ the data become troublesome especially for usage in land surface modelling that needs energy conservation at the surface (Kustas et al., 1999). Although the energy conservation is not relevant to this variance

study directly, the average of D_{EB} value during the observation is 0.67 (see section 2-3 Ground Based Observation section in chapter 2), and therefore the data set was corrected to meet the surface energy balance. Figure 5-1 shows the difference of the temperature variance normalized with temperature scale T_* in which is included surface flux with correction and without correction. The deviation from the functional curve with uncorrected data is larger than that with corrected data. Furthermore, the difference between the estimated flux by the constants in the literature with and without the energy-closed correction for eddy covariance surface flux is presented in Fig. 5-2. The rms difference between estimated flux $\overline{w'\theta'}_{vm}$ and observed flux $\overline{w'\theta'}_s$ found to be much smaller for the result by the data set with the correction, which can be expected by the deviation of variance profiles (Fig. 5-1). Furthermore, the same comparison but with the constants calibrated by $\overline{w'\theta'}_s$ with and without the energy closure correction is shown in Fig. 5-3, which resulted in opposites, i.e., the data set without correction produced smaller rms difference, but it cannot be concluded that the correction for energy-closure is invalid method and this correction might be applied for the present analysis since the other statistics such as regression coefficients and index of agreement (Willmott, 1981) are not always better. This tendency is common in the all formulation and the resultant statistics are summarized in Table 5-1.

The independently measured R_n and G values were used to close the energy balance. However, the uncertainly of G measurement remained because the value of G was measured at only one point in spite of its possible spatial variability (Kustas et al., 2000). Kato (2006) carried out observations of spatial distribution of G with 10 heat flux plates set around the routine measurement point through July to August in 2005, and some 20% of the underestimation in G value by the routine observation was suggested. If this underestimate had been the same in the 2003 observation, the surface energy budget tends to be closed and the correction for H and LE in this study would lead to the overestimation of them.

Another point to be considered in the surface flux observations is representativeness of the observed flux over the targeted region. This problem is examined in two ways: how regionally the point measurement responds to limited upwind area, and whether that area is typical for the field of interest (i.e., the source area of aircraft observation). The first question was answered by footprint analysis (e.g., Schmid, 1997). This was checked for the present

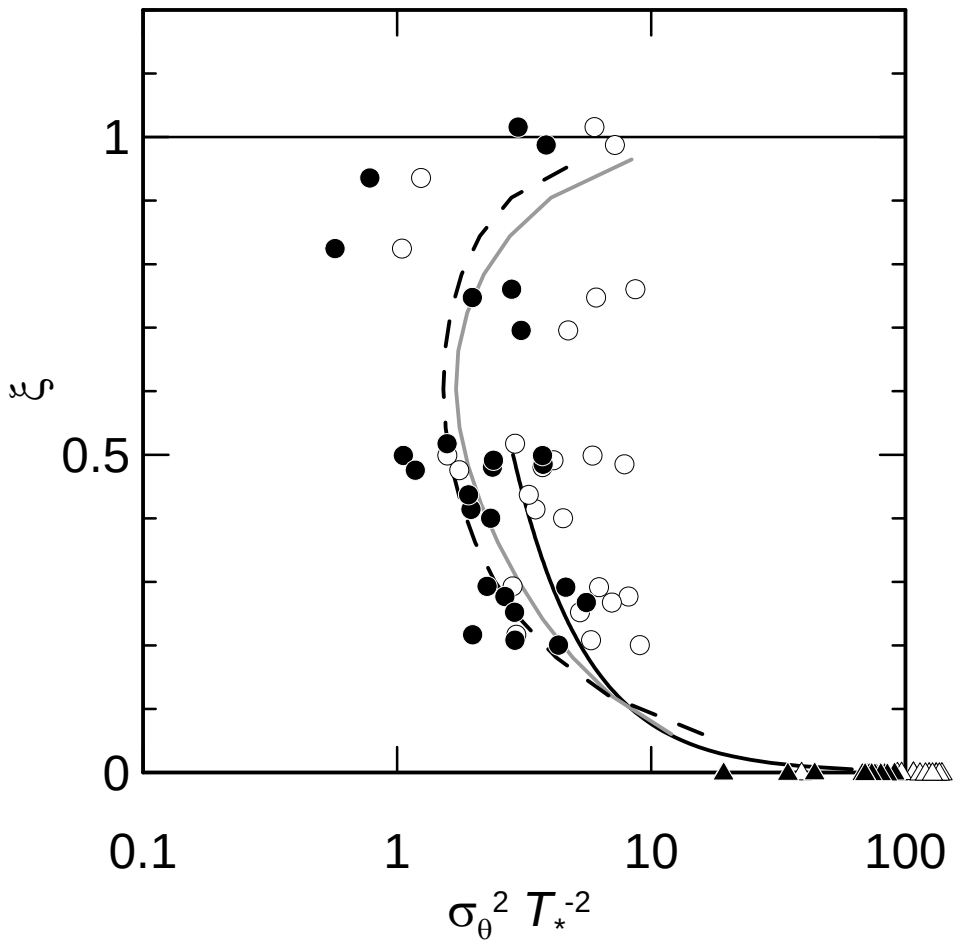

Fig. 5-1 Vertical profile of normalized variance of potential temperature $\sigma_\theta^2 T_*^{-2}$ observed above the KBU area, with previously proposed profile equations.

Solid line for Kaimal et al. (1976), gray line for Sorbjan (1989) and dashed line for Moeng and Wyngaard (1984). Solid and open circles show $\overline{w'\theta'}_s$ in T_* with and without energy closure correction, respectively

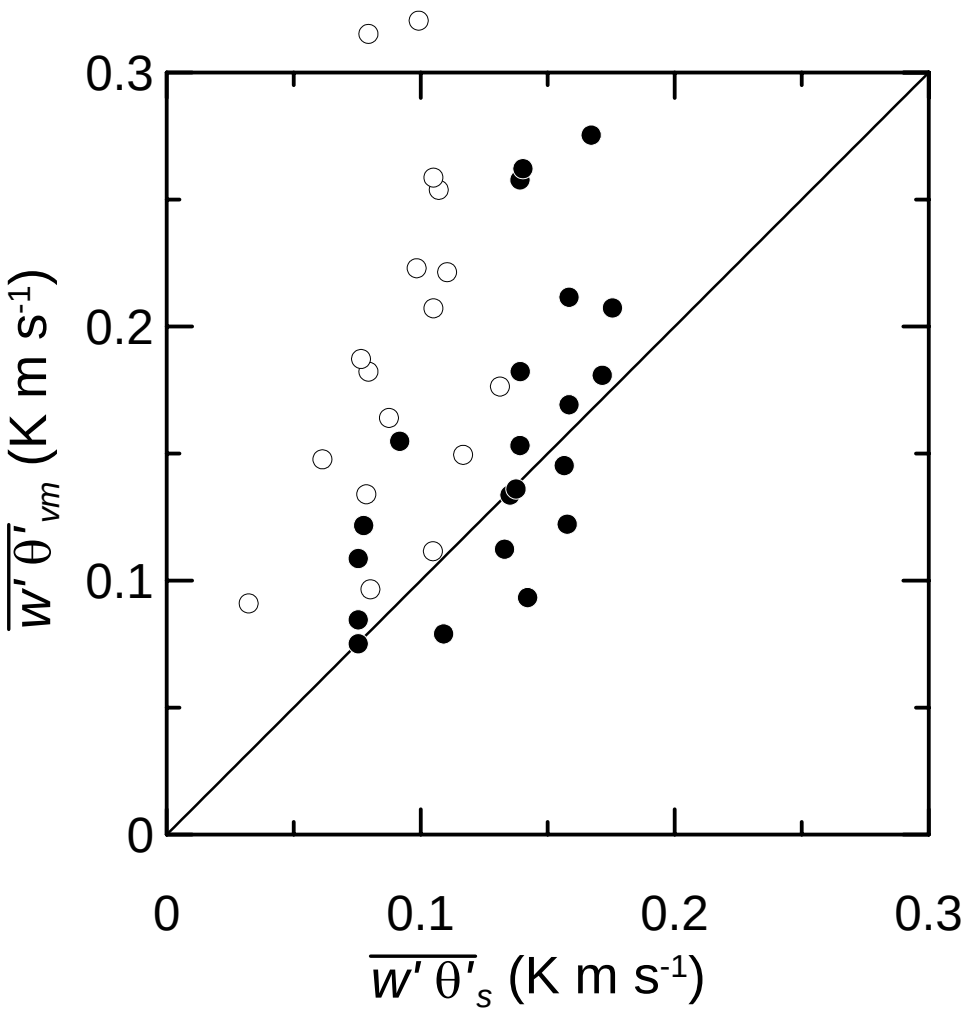

Fig. 5-2 Comparison between the sensible heat flux $\overline{w'\theta'}_{vm}$ estimated from Eq.(4.4) with the original constants and $\overline{w'\theta'}_{s}$ observed by eddy covariance method at the KBU flux station.
Solid and open circle show $\overline{w'\theta'}_{s}$ with and without energy closure correction, respectively.

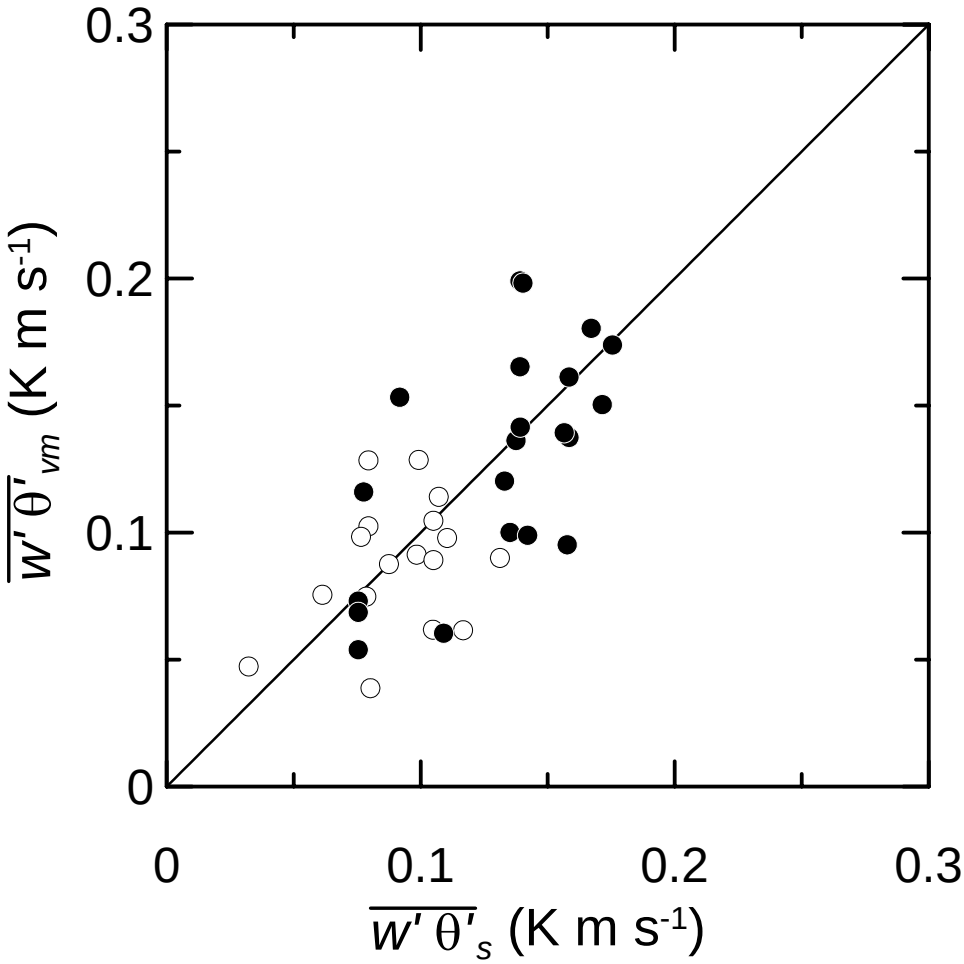

Fig. 5-3 Same as 5-2 but for Eq.(4.4) with calibrated constants.

Table 5-1 Statistics in the comparison of flux, $\overline{w'\theta'}_s$ derived form the eddy covariance method at the ground station, and $\overline{w'\theta'}_{vm}$ estimated by the variance methods, but correction for $\overline{w'\theta'}_s$ was not carried out.

(a) Eq. (4.1)

variance formulation	z/h_i	N	rms difference (K m s^{-1})	a	b	d	$\overline{w'\theta'}_s/\overline{w'\theta'}_{vm}$
Kaimal et al. (1976)	< 0.5	17	0.036	0.033	0.54	0.52	0.78
C/C	< 0.5	17	0.030	0.027	0.43	0.65	0.60
A/P	< 0.5	17	0.027	0.021	0.45	0.66	0.60
Kaimal et al. (1976)	< 0.8	21	0.041	0.024	0.64	0.58	0.82
C/C	< 0.8	21	0.030	0.018	0.49	0.69	0.62
A/P	< 0.8	21	0.026	0.016	0.50	0.75	0.62

(b) Eq. (4.2)

variance formulation	N	rms difference (K m s^{-1})	a	b	d	$\overline{w'\theta'}_s/\overline{w'\theta'}_{vm}$
Sorbjan (1989)	21	0.068	0.010	0.97	0.44	1.04
C/C	21	0.026	0.010	0.56	0.76	0.63
A/P	21	0.023	-0.005	0.67	0.82	0.63

(c) Eq. (4.3)

variance formulation	N	rms difference (K m s^{-1})	a	b	d	$\overline{w'\theta'}_s/\overline{w'\theta'}_{vm}$
fitting to normalized variance	21	0.049	0.019	0.77	0.57	0.92
C/C	21	0.026	0.013	0.53	0.75	0.63
A/P	21	0.023	0.002	0.62	0.81	0.64

Table 5-1 (continued)

(d) Eq. (4.4)

	variance formulation			N	rms difference (K m s^{-1})	a	b	d	$\overline{w'\theta'_s}/\overline{w'\theta'_{vm}}$
	v_0	v_h	entrainment model						
MW84	w_*	w_*	(3.4) with A_θ = 0.2	21	0.119	0.016	1.32	0.29	1.44
SK03	w_*	w_*	(3.4) with A_θ = 0.2	21	0.058	0.017	0.87	0.50	1.00
C/C	w_*	w_*	(3.4) with A_θ = 0.2	21	0.026	0.013	0.53	0.76	0.63
A/P	w_*	w_*	(3.4) with A_θ = 0.2	21	0.023	-0.003	0.68	0.82	0.66
A96	v_*	w_*	(3.4) with A_θ = 0.2	21	0.135	-0.072	1.90	0.27	1.35
SK03	v_*	w_*	(3.4) with A_θ = 0.2	21	0.040	0.002	0.74	0.62	0.75
C/C	v_*	w_*	(3.4) with A_θ = 0.2	21	0.034	0.012	0.66	0.68	0.75
A96	v_*	v_*	(3.9) with A = 0.2,B=5	21	0.451	0.904	-4.53	0.01	2.36
SK03	v_*	v_*	(3.9) with A = 0.2,B=5	21	0.757	1.785	-9.20	0.01	4.41
C/C	v_*	v_*	(3.9) with A = 0.2,B=5	21	0.076	0.097	-0.50	0.22	0.24

MW84: Moeng and Wyngaard (1984), SK03: Sugita and Kawakubo (2003), A96: Asanuma (1996), C/C: Coefficients calibrated to optimize flux estimation in this study, A/P: Coefficients calibrated in this study with additional parameters, *N*: number of data, rms: root mean square, *a*: intercept of regression line, *b*: slope of regression line ($\overline{w'\theta'_{vm}} = a + b\,\overline{w'\theta'_s}$), $\overline{w'\theta'_{vm}}$: estimated flux by variance methods, $\overline{w'\theta'_s}$: observed flux at the KBU station, *d*: index of agreement (Willmott, 1981), $\overline{w'\theta'_s}/\overline{w'\theta'_{vm}}$: ratio of the mean $\overline{w'\theta'_s}$ and $\overline{w'\theta'_{vm}}$

study site by the methods given by Horst and Weil (1994) and Horst (1999) which allow the estimation of the upwind distance from which 90% of the fluxes measured by an eddy covariance method, originate for a given measurement height, surface roughness and atmospheric stability. It was found that such upwind distance is in the range of 110-370 m for a typical atmospheric stability range of $-1.0 \le zL^{-1} \le -0.1$ in which z is the height of measurement and L is the Obukhov length. It is the next question whether this source area can be comparable to that of the aircraft observation. As shown in chapter 2, the source area of the aircraft segment is estimated as a few km in the upwind direction, and thus, the aircraft detected a broader area than the ground station instruments did. In the same study area, Asanuma and Iemoto (2006) carried out the observation with a large aperture scintillometer that allowed evaluation of the sensible heat flux H averaged over a distance of up to 5 km. In their results, the fluxes observed at the station and those along the scintillometer path are indeed comparable with each other, while the surface variability was detected in the difference of H between different paths by detailed analysis.

Moreover the regional characteristics of the ground surface, namely surface flux and its spatial distribution could add the uncertainty to the similarity relationships. It is assumed in the similarity approach that a given surface flux is identical to the objective space and time. Although the past studies used data set obtained at horizontally homogenous surface, actually, some heterogeneity exists at certain horizontal scale, pattern and intensity. Mahrt (2000) proposed distinct length scales according to relation between horizontal scale of surface heterogeneity and atmospheric structure. In the case of mixed layer, surface heterogeneous length scale L_{Rau} is proportional to the CBL length scale suggested by Raupach and Finnigan (1995),

$$L_{Rau} = C_{Rau} \frac{U h_i}{w_*} \tag{5.4}$$

where $C_{Rau} \approx 0.8$ is a nondimensional coefficient determined experimentally, Uh_i / w_* is the CBL length scale. With typical values of the mean horizontal wind velocity U = 10 m s^{-1}, height of CBL (mixed layer) h_i = 1000 m, and velocity scale w_* = 1.5 m s^{-1}, this scale was found to be 5.3

km. If surface heterogeneous scale is less than L_{Rau}, the effect of surface heterogeneity is confined below the CBL height. Strunin et al. (2004) show this effect of surface heterogeneity to applicability of similarity scaling with their aircraft data observed over non-homogeneous surface under different thermal conditions. For the present study site, some flight segments closer to the river channel (Fig. 2-5) might detect the surface heterogeneity with horizontal scale larger than L_{Rau}, which effect, however, was not clear.

5-2 Universality of Scalar Variance Formulations in the Mixed Layer

The variance formulations contain some experimental functions and constants, which are considered universal. In this study, through calibration the constants were re-determined and these results were found slightly different from the values in the literature, although attention should be paid to the fact that calibration process in this study was to minimize the difference between the estimated and the observed fluxes. Several previous research also evaluated the constants with their own data set (e.g., Sugita and Kawakubo, 2003; Bernard-Trottolo et al, 2004). For example, the coefficient of free convection variance formulation (Eq. 3.2) was evaluated as 1.8 (Kaimal et al., 1976; Lenschow et al., 1980), 1.2 (Bernard-Trottolo et al, 2004) and 1.4 in this study, and more complicated formulations with more parameters show variability of their coefficients (Table 4-1). This variability of 'universal' constants would absorb the deviation from an assumption of horizontal homogeneity and stationarity of each data set.

One of the causes of the variability might be due to the difference in observation (simulation) methods to obtain data for the constants evaluation. These include record length for averaging statistics, methods of filtering process, measurement instruments or platforms and so on. These variations could cause an inherent bias in each data set. The difference of data sampling by one point observation, i.e., instrumented tower (e.g., Sugita and Kawakubo, 2003) or tethered balloon (e.g., Kaimal et al., 1976) and spatial observation by aircraft (e.g., Asanuma, 1996) would not affect the results fundamentally if horizontal homogeneous and stationarity were assured. In contrast to them, Moeng and Wyngaard (1984) used their numerical simulation results to establish their variance formulation. Such data set might be ideal since it

could produce an ensemble average with repeatable calculations and inherently satisfies the assumption required for similarity approach mentioned above. Similarly, the methods of evaluating the reference surface fluxes were also not necessarily the same. The best or better observation strategy considerable at the moment was taken by each study, as for averaging length, measurement height, process of deriving surface flux and so on. Moreover, these flux values were obtained by the eddy covariance methods, but the energy closure problem of surface heat budget was not considered unlike this study. It is rather contradictive that the results with the corrected flux in this study agree to those without the correction in the past studies, although it is not clear whether the energy shortage of the eddy covariance flux existed or not. Furthermore, these surface fluxes should be spatially representative to match to spatial scale of the mixed layer observations, although the methods to obtain such data are not fully established today. This remaining uncertainty in the surface flux values is also added to data set bias.

The other possibility is insufficient or excessive parameters included in the similarity formulations. As mentioned before, the turbulence structure in the mixed layer depends on several variables such as the mixed layer height, entrainment flux, large scale advection, subsidence, geostrophic wind shear, wind speed at the top of the mixed layer and so on. Apparently, it becomes critical in the usage of similarity formulations whether or not could be achieved not only availability but also reduction of uncertainty in the variable parameters. Crago and Brutsaert (1995) present the dependency of ABL bulk similarity formulation of the mean wind on the additional similarity functions including baroclinicity and momentum advection (i.e., acceleration), but do not necessarily recommend their formulation because of its random measurement error. However, it is not clear at this point whether this is the case, since other factors mentioned above could be very well have dominated the remaining error and introduction of the other parameters or formulations may not have sufficient impacts on to the final results. This is partially true with the introduction of the larger scale atmospheric variables that have been achieved in this study. Availability of new data sets such as the outputs of regional climate model with finer resolutions in time and space enables to utilize such parameters in spite of a limitation of model outputs as mentioned in chapter 2.

6 Conclusions

Turbulence data obtained by aircraft observations in the mixed layer over an extensive steppe region in Mongolia were analysed to estimate the surface fluxes by means of the mixed layer variance methods. The aircraft observations carried out on eleven days in a period from July to October in 2003, in which several heights within and above the mixed layer were flown repeatedly above the flux observation site. This observation period contained wet and dry conditions, which covered the range of Bowen ratio from 0.8 to 3.0 and that of sensible heat flux observed at a flux station by eddy covariance method was from 80 W m^{-2} to 200 W m^{-2}. The characteristics of observed scalar structure in the mixed layer are summarised as follows;

- Vertical profiles of temperature and humidity showed vertical development of the mixed layer, and especially that of specific humidity was almost constant with height, which indicates suppressed evapotranspiration from the ground.
- Deviation of temperature variance from the profile formulation proposed by the previous studies was larger in wet period (sensible and latent heat fluxes at the surface were nearly equal) than in dry period.
- The lower half of the mixed layer showed large temperature variance and positive correlation between temperature and humidity, which were caused by heat and moisture fluxes from the ground surface, while in the upper half of mixed layer the tendency was unclear. The scattering of these variables possibly due to the effects of entrainment heat flux from the above atmosphere.
- The vertical profiles of the second moment about the mean, i.e., the variance, of temperature followed in general the functional forms proposed by previous researchers, and the root mean square (rms) difference between observed and predicted values was the same level regardless a type of formulation.

These variance statistics were applied to the variance formulations to estimate surface sensible

heat fluxes. First, the flux estimation was made with these equations and the constant parameters as proposed in previous studies. Then, the constants were re-calibrated with the current data set and used for flux estimation. Finally, additional variables, which represent the large scale atmospheric conditions mainly baroclinicity and horizontal advection, were considered for possible improvement of the flux estimation. The results of application of variance methods are summarized as follows;

- The convective scaling velocity met better results than scaling with shear effects.
- With the functional forms and the original constants, this procedure produced $\overline{w'\theta'}_0$ values that agree with the reference fluxes measured at the KBU flux station with an rms difference of about 40 to 100 W m^{-2}.
- After calibration of the constants with the current data set, the same procedure yielded the fluxes with an rms difference of 30 to 40W m^{-2}.
- Introduction of four additional parameters, which represent the large scale atmospheric influence, with calibration of the constants, further reduced the rms difference down to about 30 W m^{-2} or less.
- The large scale atmospheric parameters such as baroclinicity, i.e., horizontal temperature gradient, and horizontal advection could refine the estimation result effectively, and the effect of the other parameters was rather unclear.
- Difference among types of formulation was not significant, and thus the usage of simpler formulation, which needs less number of parameters, is preferable for the practical application of variance methods.
- The major cause of estimation error in the variance methods was the error of temperature variance, and the possible error is maximal at the higher level for free convection formulation and the middle level for the others.

The present analyses indicate that the mixed layer variance methods are capable of producing surface fluxes with turbulence data measured from an aircraft. However, it also indicates that local calibration of the constants in the mixed layer variance equations is needed to achieve flux estimation with sufficient accuracy. Remained uncertainty and expected treatment of the

current data set was as follows;

- Insufficient length of flight segment caused sampling error, and it required a few hundred kilometre of length to reduce these error to 10% level. Then, in order to achieve this condition, flight path should be designed, for instance, by repeating the same level.
- As reference surface flux, the eddy covariance flux observed at ground station was used with corrections to close the energy budget. Variance methods with the original constants produced smaller rms difference for data set with the correction than that without the correction, but in the case of flux estimation with calibrated constants, the results were opposite. It is not clear at this point whether correction of energy closure should be considered.
- The eddy covariance flux measured at the ground station was assured to be representative of the surrounding area, but there might remain heterogeneous effect by circumferential features.

Through these improvements of data acquirement system including measurement and data processing, errors in the data set would be reduced and then the accuracy of flux estimation would be raised. However, at the present, it is remain the problem whether or not the need of the local calibration is an indication of the lack of universality of the equations, given the wide range of data sets employed in the past. The need for the calibration means that these experimental constants would inherently contain problem of the variance formulations including unsuitable scaling and parameters, that is possibility of some relevant physics not sufficiently incorporated within the formulations, as well as uncertainties of measurements. As a whole, the reduction of the error by the local calibration suggests that refinement of the equations is still needed for the application of mixed layer variance methods with sufficient accuracy.

Acknowledgements

I wish to express my gratitude to Dr. M. Sugita, Associate professor of Graduate School of Life and Environmental Sciences, University of Tsukuba, for his continuous guidance and encouragements throughout my graduate work, which has led me attracted to the land-atmosphere research.

I am also grateful to Dr. N. Tase and Dr. T. Tanaka, Professor of Graduate School of Life and Environmental Sciences, University of Tsukuba, for their plentiful suggestions and guidance. Dr. J. Asanuma, Associate professor of Terrestrial Environment Research Center, University of Tsukuba and Dr. S.-G. Li of Japan Science and Technology Agency gave me advice and support in the field experiments. I would like to appreciate Dr. H. Okura, Professor of Graduate School of Life and Environmental Sciences, University of Tsukuba and at National Research Institute for Earth Science and Disaster Prevention, Dr. M. Tsujimura Assistant professor of Graduate School of Life and Environmental Sciences, University of Tsukuba, Dr. T. Yamanaka, Assistant professor of Terrestrial Environment Research Center, University of Tsukuba, and Dr. S. Iida, Graduate School of Life and Environmental Sciences, University of Tsukuba, for their countless comments and opportunity of fruitful discussion. I am also grateful to Dr. W. Brutsaert, Professor of Cornell University for his advice and encouragement.

A part of data in aircraft observation owes to Dr. D. Matsushima, Associate professor of Chiba Institute of Technology, and the data of regional climate model was prepared by Dr. T. Sato of Japan Science and Technology Agency. I would like to thank them to allow me using their dataset and give me significant advice. Through the field experiments in Mongolia, people in Institute of Meteorology and Hydrology of Mongolia, and local people supported me.

Many thanks to my colleagues Mr. M. Saito and Mr. H. Iwata, University of Tsukuba, for sharing time of discussing. I feel appreciating Mr. H. Kato and Mr. Byanbahuu, University of Tsukuba, Mr. T. Kojima of NTT Data Co. and Mr. H. Tanaka of Climatec Inc. for their coorporation in my graduate work. And also thanks to all of the staff and students in hydrology group.

Finally, I express special thanks my family to give me a chance to study and continuous encouragements.

This work has been supported by a CREST project (The Rangelands Atmosphere -Hydrosphere -Biosphere Interaction Study Experiment in Northeastern Asia) of JST (Japan Science and Technology Agency)

Abrams, M., 2000. The advanced spaceborne thermal emission and reflection radiometer (ASTER): data products for the high spatial resolution imager on NASA's Terra platform. Int. J. Rem. Sens., 21, 847-859.

André, J. C., Goutorbe, J.-P. and Perrier, A., 1986. HAPEX-MOBILHY: A hydrologic atmospheric experiment, for the study of water budget and evaporation flux at the climate scale. Bull. Am. Meteorol. Soc., 67, 138-144.

André, J. C., LaCarrere, P. and Mahrt, L. J., 1979. Sur la distribution verticale de l'humidite dans une couche limite convective. J. Rech. Atmos., 13, 135-146.

Arya, S. P. S., 1999. Air Pollution Meteorology and Dispersion. Oxford University Press, New York. 310 pp.

Arya, S. P. S., 2001. Introduction to Micrometeorology. 2nd Ed., Academic Press, San Diego. 420 pp.

Arya, S. P. S. and Wyngaard, J. C., 1975. Effect of baroclinicity on wind profiles and the geostrophic drag law for the convective planetary boundary layer. J. Atmos. Sci., 32, 767-778.

Asanuma, J., 1996. Turbulence Variance Characteristics in the Unstable Atmospheric Boundary Layer above Flat Pine Forest. Ph.D. Thesis, Cornell University.

Asanuma, J. and Brutsaert, W., 1999. Turbulence variance characteristics of temperature and humidity in the unstable atmospheric surface layer above a variable pine forest. Water Resour. Res., 35, 515-521.

Asanuma, J. and Iemoto, K., 2006. Measurements of regional sensible heat flux over Mongolian grassland using large aperture scintillometer. J. Hydrol., in press.

Asanuma, J., Dias, N. L., Kustas, W. P. and Brutsaert, W., 2000. Observations of neutral profiles of wind speed and specific humidity above a gently rolling landscape. J. Meteorol. Soc. Jpn., 78, 719-730.

Berger, B. W., Davis, K. J., Yi, C., Bakwin, P. S. and Zhao, C. L., 2001. Long-term carbon

dioxide fluxes from a very tower in a northern forest: flux measurement methodology. J. Atmos. Oceanic Technol., 18, 529-542

Bernard-Trottolo, S., Campistron, B., Druilhhet, A., Lohou, F. and Saïd, F., 2004. TRAC98: Detection of coherent structures in a convective boundary layer using airborne measurements. Bound.-Layer Meteorol., 111, 181-224.

Betts, A. K. and Ball, J. H., 1994. Budget analysis of FIFE 1987 Sonde Data. J. Geophys. Res., 99, 3655-3666.

Blackader, A. K. and Tennekes, H., 1968. Asymptotic similarity in neutral barotropic planetary boundary layers. J. Atmos. Sci., 25, 1015-1020.

Brutsaert, W., 1982. Evaporation into the Atmosphere. D. Reidel, Dordrecht. 299pp.

Brutsaert, W. and Mawdsley, J. A., 1976. The applicability of planetary boundary layer theory to calculate regional evapotranspiration. Water Resour. Res., 12, 852-858.

Brutsaert, W. and Sugita, M., 1991. A bulk similarity approach in the atmospheric boundary layer using radiometric skin temperature to determine regional surface fluxes. Bound.-Layer Meteorol., 55, 1-23.

Caughey, S. and Palmer, S., 1979. Some aspects of turbulent structure through the depth of the convective boundary layer. Q. J. R. Met. Soc., 105, 811-827.

Cleugh, H. A., Raupach, M. R., Briggs, P. R. and Coppin, P. A., 2004. Regional-scale heat and water vapour fluxes in an agricultural landscape: an evaluation of CBL budget methods at OASIS. Bound.-Layer Meteorol., 110, 99-137.

Crago, R. D. and Brutsaert, W., 1994. The estimation of surface momentum flux under unstable conditions from the atmospheric pressure field. Water Resour. Res., 30, 617-623.

Crago, R. D. and Brutsaert, W., 1995. Dependence of geostrophic drag on the intensity of convection, baroclinicity, and acceleration. Boundary-Layer Meteorol., 73, 211-225.

Deardorff, J. W., 1970a. Primary results from numerical integration of the unstable planetary boundary layer. J. Atmos. Sci., 27, 1209-1211.

Deardorff, J. W., 1970b. Convective velocity and temperature scales for the unstable planetary boundary layer and for Rayleigh convection. J. Atmos. Sci., 27, 1211-1213.

De Bruin, H. A. R. and Hartfensis, O. K., 2005. Variance method to determine turbulent fluxes of momentum and sensible heat in the stable atmospheric surface layer. Boundary-Layer

Meteorol., 116, 385-392. DOI 10.1007/s10546-004-1986-2.

De Roode, S. R., Jonker, H. J. J., Duynkerke, P. G. and Stevens, B., 2004. Countergradient fluxes of conserved variables in the clear convective and stratocumulus-topped boundary layer: the role of the entrainment flux. Boundary-Layer Meteorol., 112, 179-196.

Driedonks, A. G. M., 1982. Models and observations of the growth of the atmospheric boundary layer. Boundary-Layer Meteorol., 23, 283-306.

Eng, K., Coulter, R. L. and Brutsaert, W., 2003. Vertical velocity variance in the mixed layer from Radar wind profilers. J. Hydrologic Engrg., 8, 301-307.

Grant, A. L. M. and Mason, P. J., 1990. Observations of boundary layer structure over complex terrain. Quart. J. Roy. Mereor. Soc., 116, 159-186.

Garrat, J. R., 1992. The atmospheric boundary layer. Cambridge University Press, Cambridge. 316 pp.

Garrat, J. R., Wyngaard, J. C. and Francey, R. J., 1982. Winds in the atmospheric boundary layer –prediction and observation. J. Atmos. Sci., 39, 1307-1316.

Garrat, J. R., Hess, G. D., Physick, W. L. and Bougeault, P., 1996. The atmospheric boundary layer – advances in knowledge and application. Boundary-Layer Meteorol., 78, 9-37.

Hägeli, P., Steyn, D. G. and Strawbridge, K. B., 2000. Spatial and temporal variability of mixed-layer depth and entrainment zone thichkness. Boundary-Layer Meteorol., 97, 47-71.

Hechtel, L. H., Moeng, C.-H. and Stull, R. B., 1990. The effects of nonhomogeneous surface fluxes on the convective boundary layer: a case study using large-eddy simulation. J. Atmos. Sci., 47, 1721-1741.

Hiyama, T., Sugita, M. and Kotoda, K., 1996. Regional roughness parameters and momentum fluxes over a complex area. J. Appl. Meteor., 35, 2179-2190.

Horst, T. W., 1999. The footprint for estimation of atmosphere-surface exchange fluxes by profile techniques. Boundary-Layer Meteorol., 90, 171-188.

Horst, T. W. and Weil, J. C., 1994. How far is far enough – the fetch requirements for micrometeorological measurement of surface fluxes. J. Atmos. Oceanic Technol., 11, 1018-1025.

Joffre, S. M., 1985. Effects of local accelerations and baroclinicity on the mean structure of the atmospheric boundary layer convection over the sea. Boundary-Layer Meteorol., 32,

237-255.

Jonker, H. J. J., Duynkerke, P. G. and Cuijpers, J. W. M., 1999. Mesoscale fluctuations in scalars generated by boundary layer convection. J. Atmos. Sci., 56, 801-808.

Kader, B. A. and Yaglom, A. M., 1990. Mean field and fluctuation moments in unstably stratified turbulent boundary layers. J. Fluid Mech., 212, 637-662.

Kaimal, J. C. and Finnigan, J. J., 1994. Atmospheric Boundary Layer Flows. Oxford University Press, New York. 289 pp.

Kaimal, J. C., Wyngaard, J. C., Haugan, D. A., Cote, O. R. and Izumi, Y., 1976. Turbulence structure in the convective boundary layer. J. Atmos. Sci., 33, 637-662.

Kalnay, E. Kanamitsu, M., Kistler, R., Collins, W., Deaven, D., Gandin, L., Iredell, M., Saha, S., White, G., Woollen, J., Zhu, Y., Leetmaa, A. and Reynolds, B., 1996. The NCEP/NCAR 40-year reanalysis project. Bull. Amer. Meteor. Soc., 77, 437-471.

Kato, H., 2006. Effect of grazing on vegetation and surface fluxes of momentum, heat, and CO2. MS thesis, University of Tsukuba. In preparation.

Katul, G., Hsieh, C.-I., Oren, R., Ellsworth, D. and Phillips, N., 1996. Latent and sensible heat flux predictions from a uniform pine forest using surface renewal and flux variance methods. Boundary-Layer Meteorol.,80, 249-282.

Katul, G., Stewart, M. G., Hsieh, C.-I., Cheng, Y., Mowry, F. and Sigmon, J., 1995. Estimation of surface heat and momentum fluxes using the flux-variance method above uniform and non-uniform terrain. Boundary-Layer Meteorol., 74, 237-260.

Kim, H.-J., Noh, Y. and Raasch, S., 2004. Interaction between wind and temperature fields in the planetary boundary layer for a spatially heterogeneous surface heat flux. Boundary-Layer Meteorol., 111, 225-246.

Kimmel, S. J., Wyngaard, J. C. and Otte, M. J., 2002. “Log-chipper” turbulence in the convective boundary layer. J. Atmos. Sci., 59, 1124-1134.

Kustas, W. P. and Brutsaert, W., 1986. Wind profile constants in a neutral atmospheric boundary layer over complex terrain. Boundary-Layer Meteorol., 34, 35-54.

Kustas, W. P. and Brutsaert, W., 1987a. Virtual heat entrainment in the mixed layer over very rough terrain. Boundary-Layer Meteorol., 38, 141-157.

Kustas, W. P. and Brutsaert, W., 1987b. Budget of water vapor in the unstable boundary layer

over rugged terrain. J. Clim. Appl., 607-620.

Kustas, W. P., Prueger, J. R., Humes, K. S. and Starks, P. J., 1999. Estimation of surface heat fluxes at field scale using surface layer versus mixed layer atmospheric variables with radiometric temperature observations. J. Appl. Meteorol., 38, 224-238.

Kustas, W. P., Prueger, J. H., Hatfield, J. L., Ramalingam, K. and Hipps, L. E., 2000. Variability in soil heat flux from a mesquite dune site. Agric. For. Meteorol., 108, 249-264.

Lenschow, D. H., 1986. Aircraft measurements in the boundary layer. In Lenschow, D. H., Ed., Probing the Atmospheric Boundary Layer, American Meteorological Society, Boston, 39-55.

Lenschow, D. H. and Stankov, B. B., 1986. Length scale in the convective boundary layer. J. Atmos. Sci., 43, 1198-1209.

Lenschow, D. H. and Stephens, P. L., 1980. The role of thermals in the convective boundary layer. Boundary-Layer Meteorol., 19, 509-532.

Lenschow, D. H., Mann, J. and Kristensen, L., 1994. How long is long enough when measuring fluxes and other turbulence statistics? J. Atmos. Oceanic Technol., 11, 661-673.

Lenschow, D. H., Wyngaard, J. C. and Pennell, W. T., 1980. Mean-field and second-moment budgets in a baroclinic, convective boundary layer. J. Atmos. Sci., 37, 1313-1326.

Lettau, H., 1969. Note on aerodynamic roughness-parameter estimation on the basis of roughness-element description. J. Appl. Meteor., 8, 828-832.

Li, S-G., Asanuma, J., Kotani, A., Eugster, W., Davaa, G., Oyunbaatar, D. and Sugita, M., 2005. Net ecosystem carbon dioxide exchange over grazed steppe in central Mongolia. Global Change Biol., 11, 1941-1955. DOI 10.1111/j.1365-2486.2005.01047.x

Liu, X., and Ohtaki, E., 1997. An independent method to determine the height of the mixed layer. Boundary-Layer Meteorol., 85, 497-504.

Lloyd, C. R., Culf, A. D., Dolman, A. J. and Gash, J. H. C., 1991. Estimates of sensible heat fluxes from observations of temperature fluctuations. Boundary-Layer Meteorol., 57, 311-322.

Mahrt, L., 1976. Mixed layer moisture structure. Mon. Wea. Rev., 104, 1403-1407.

Mahrt, L., 1998. Flux sampling errors for aircraft and towers. J. Atmos. Oceanic Technol., 15, 416-429.

Mahrt, L., 2000. Surface heterogeneity and vertical structure of the boundary layer.

Boundary-Layer Meteorol., 96, 33-62.

Mahrt, L. and Paumier, J., 1985. Simple formulation of heat flux in the unstable atmospheric boundary layer. Boundary-Layer Meteorol., 33, 61-75.

Mann, J. and Lenschow, D. H., 1994. Errors in airborne flux measurements. J. Geophys. Res., 99, 14519-14526.

Moeng, C. -H. and Wyngaard, J. C., 1984. Statistics of conservative scalars in the convective boundary layer. J. Atmos. Sci., 41, 3161-3169.

Monin, A. S. and Obukhov, A. M., 1954. Basic laws of turbulent mixing in the atmospheric near the ground. Tr. Akad. Nauk., SSSR Geophiz. Inst., 24(151), 1963-1987.

Monin, A. S. and Yaglom, A. M., 1971. Statistical Fluid Mechanics: Mechanics of Turbulence. Vol. 1, English trans., ed. Lumley, J. L. MIT Press, Cambridge, 769 pp.

Padro, J., 1993. An investigation of flux-variance methods and universal functions applied to three land-use types in unstable conditions. Boundary-Layer Meteorol., 66, 413-425.

Raupach, M. R. and Finnigan, J. J., 1995. Scale issues in boundary-layer meteorology: Surface energy balances in heterogeneous terrain. Hydrol. Process., 9, 589-612.

Saandar, M. and Sugita, M., 2004. Digital Atlas of Mongolian Natural Environments, (1) Vegetation, Soil, Ecology and Water, CD-ROM, Monmap Engineering Service Co., Ltd, Ulaanbaatar 210646, Mongolia.

Santoso, E. and Stull. R., 1999. Use of synthetic data to test flight patterns for a boundary layer field experiment. J. Atmos. Oceanic Technol., 16, 1157-1171.

Sato, T. and Kimura, F., 2005. Diurnal cycle of convective instability around the central mountains in Japan during the warm season. J. Atmos. Sci., 62, 1626-1636. DOI 10.1175/JAS3423.1

Sato, T., Kimura, F. and Kitoh A., 2006. Projection of global warming onto regional precipitation over Mongolia using a regional climate model. J. Hydrol., in press.

Schmid, H. P., 1997. Experimental design for flux measurements: matching scales of observations and fluxes. Agric. For. Meteorol., 87, 179-200.

Sorbjan, Z., 1989. Structure of the Atmospheric Boundary Layer, Prentice Hall, New Jersey. 317pp.

Sorbjan, Z., 2004. Large-eddy simulations of the baroclinic mixed layer. Boundary-Layer

Meteorol., 112, 57-80.

Sorbjan, Z., 2005. Statistics of Scalar Fields in the Atmospheric Boundary Layer Based on Large-eddy Simulations. Part 1: Free Convection. Boundary-Layer Meteorol., 116, 467-486. DOI 10.1007/s10546-005-0907-3.

Strunin, M. A., Hiyama, T., Asanuma, J. and Ohata, T., 2004. Aircraft observations of the development of thermal internal boundary layers and scaling of the convective boundary layer over non-homogeneous land surfaces. Boundary-Layer Meteorol., 111, 491-522.

Stull, R. B., 1988. An Introduction to Boundary Layer Meteorology. Kluwer Academic Publishers, Dordrecht. 670 p.

Sugita, M. and Brutsaert, W., 1990. Wind velocity measurements in the neutral boundary layer above hilly prairie. J. Geophys. Res., 95 (D6), 7617-7624.

Sugita, M. and Kawakubo, N., 2003. Surface and mixed-layer variance methods to estimate regional sensible heat flux at the surface. Boundary-Layer Meteorol., 106, 117-145.

Sugita, M., Endo, N. and Hiyama, T, 1999. Regional surface momentum flux derived from atmospheric boundary layer bulk similarity approach. J. Geophys. Res., 104 (D14), 16965 -16972.

Sugita, M., Asanuma, J., Tsujimura, M., Mariko, S., Lu M., Kimura, F., Azzaya, D. and Adyasuren Ts., 2006, An Overview of the Rangelands Atmosphere-Hydrosphere-Biosphere Interaction Study Experiment in Northeastern Asia (RAISE), J. Hydrol., in press.

Sun and Marhr, L., 1994. Spatial distribution of surface fluxes estimated from remotely sensed variables. J. Appl. Meteorol., 33, 1341-1353.

Tennekes, H., 1973. A model for the dynamics of the inversion above a convective boundary layer. J. Atmos. Sci., 30, 558-567.

Tennekes, H., 1982. Similarity relations, scaling laws and spectral dynamics. In Nieuwstadt, F. T. M. and van Dop, H. Eds., Atmospheric Turbulence and Air Pollution Modeling, D. Reidel, Dordrecht, 37-68.

Tillman, J. E., 1972. The indirect determination of stability, heat and momentum fluxes in the atmospheric boundary layer from simple scalar variables during dry unstable conditions. J. Appl. Meteorol., 11, 783-792.

Twine, T.E., Kustas, W. P., Norman, J. M., Cook, D. R., Houser, P. R., Meyers, T. P., Prueger, J.

H., Starks, P. J. and Wesely, M. L., 2000. Correcting eddy-covariance flux underestimates over a grassland. Agric. For. Meteorol., 103, 279-300.

UNEP, 1997. World Atlas of Desertification, 2nd ed. 182p.

van Dop, H., van As, D., van Herwijnen, A., Hidderd, M. F. and Jonker, H., 2005. Length scales of scalar diffusion in the convective boundary layer: laboratory observations. Boundary-Layer Meteorol., 116, 1-35. DOI 10. 1007/s10546-004-2165-1.

Vihma, T. and Kottmeier, C., 2000. A modelling approach for optimising flight patterns in airborne meteorological measurements. Boundary-Layer Meteorol., 95, 211-230.

Weil, J. C. and Horst, T. W., 1992. Footprint estimates for atmospheric flux measurements in the convective boundary layer. In Schwarts, S.E. and Slinn, W. G. N. Eds., Precipitation Scavenging and Atmosphere-Surface Exchange, Vol.2, Hemisphere, Washington, DC, 717-728.

Wesely, M. L., 1988. Use of variance techniques to measure dry air-surface exchange rates. Boundary-Layer Meteorol., 44, 13-31.

Willmott, C. J., 1981. On the validation of models. Phys. Geogr., 2, 184-194.

Wilson, K., Goldstein, A., Falge, E., Aubinet, M., Baldocchi, D., Berbigier, P., Bernhofer, C., Ceulemans, R., Dolman, H., Field, C., Grelle, A., Ibrom, A., Law, B. E., Kowalski, A., Meyers, T., Moncrieff, J., Monson, J., Oechel, W., Tenhunen, J., Valentini, R. and Verma, S., 2000. Energy balance closure at FLUXNET sites. Agric. For. Meteorol., 113, 223-243.

Wyngaard, J. C., 1985. Structure of the planetary boundary layer and implications for its modelling. J. Clim. Appl. Meteorol., 24, 1131-1142.

Wyngaard, J. C. and Brost, R. A., 1984. Top-down and buttom-up diffusion of a scalar in the convective boundary layer. J. Atmos. Sci., 41, 102-112.

Wyngaard, J. C., Coté, O. R. and Izumi, Y., 1971. Local free convection, similarity, and the budgets of shear stress and heat flux. J. Atmos. Sci., 28, 1171-1182.

Wyngaard, J. C., Pennel, W. T., Lenschow, D. H. and LeMone, M. A., 1978. The temperature-humidity covariance budget in the convective boundary layer. J. Atmos. Sci., 35, 47-58.

Zilitinkevich, S. S., 1975. Resistance laws and prediction equations for the depth of the planetary boundary layer. J. Atmos. Sci., 32, 741-752.

Appendices

A-1 Estimation of the Mixed Layer Height

The value of mixed layer height h_i was estimated using a method proposed by Liu and Ohtaki (1997), with the peak frequency f_p of the spectra of the horizontal wind speed data obtained at the KBU flux station. Since it is not always easy to identify f_p from a single spectral curve, it was decided to evaluate f_p as the average peak frequency of the six spectral curves. In order to implement this procedure, six 55-min time series were generated out of the raw turbulence data obtained over a 90-min period that included the time of each flight segment. Their power spectra were evaluated and then were used to derive the mean spectral curve that was finally used to evaluate f_p for this flight segment. Since it is quite possible to have errors of around 100 m in the estimation of h_i with this procedure, and since it produces only a single value for the selected 90-min period, the same h_i value was assigned to all flight segments within the same 90-min period. This is probably acceptable, since Sugita and Kawakubo (2001) reported that the mixed layer variance methods are not very sensitive to the exact value of h_i. It was found that h_i was around 700 – 1600 m during the flight observation periods (Table 2-1).

A-2 Evaluation of Regional Friction Velocity

Since velocity was not directly measured by the aircraft in the present study, u_* was estimated from a formulation based on Rossby-number similarity which relates the surface stresses and the geostrophic wind (e.g., Blackader and Tennekes, 1968; Zilitinkevich, 1975),

$$\frac{u_*^{\,2}}{GW^2} = k^2 \left\{ \left[\ln\left(\frac{u_*}{|f| z_0} \right) - A_G \right]^2 + B_G^{\,2} \right\}^{-1} \tag{A.1}$$

where GW is the geostrophic wind, f is the Coriolis parameter, k is von Kármán's constant, and z_0 is the surface roughness length. The symbols A_G and B_G represent universal functions of the stability h_i /L where L is the Obukhov length, and those proposed by Zilitinkevich (1975) were adopted in the analysis. The northward and eastward components of GW, i.e., U_g and V_g, were evaluated from the pressure gradient on a 800 hPa isobaric surface from the outputs of the regional climate model as described in chapter 2 and appendix A-3. The value of z_0 was estimated from the formulation of Grant and Mason (1990), (A.2), which is based on the idea that the total stress at a particular height should be the sum of the form drag on major roughness elements such as topography and the shear stress acting on the local surface,

$$\frac{z_0}{h} = \frac{1}{2}\left(\exp\left\langle \frac{k}{\left\{ \lambda D_{h/2} + k^2 \left[\ln\left(h / 2z_{0l} \right) \right]^{-2} \right\}^{1/2}} \right\rangle \right)^{-1} \tag{A.2}$$

where h is the mean height of the major obstacles, $\lambda = A / S$ is the roughness density with A being the silhouette area of the roughness elements on a horizontal area S, $D_{h/2}$ is the drag coefficient of the major obstacles evaluated at $z = h/2$ and z_{0l} is the local roughness length of the surface. To apply (A.2), $D_{h/2}$ and z_{0l} must be known. The drag coefficient $D_{h/2}$ was evaluated from an expression of Lettau (1969), which was derived from an experiment with bushel baskets placed in different arrays on an icy lake surface,

$$\frac{z_0}{h} = c\lambda \tag{A.3}$$

where c is a constant (≈ 0.5). The z_0 value of (A.3) in his experiment was mostly from the major obstacles of the baskets and the contribution from the shear stress of the icy surface itself was probably minimal, and thus can be used to estimate $D_{h/2}$ in (A.2). Once z_0 has been evaluated from (A.3), it can be converted to the drag coefficient $D_{h/2}$ as follows. The form drag F can be given as

$$F = D_{h/2}\rho A u_{h/2}^2 \tag{A.4}$$

where $u_{h/2}$ is the wind speed at $z=h/2$. The wind profile equation in surface layer derived from Monin-Obukhov similarity theory (e.g., Brutsaert, 1982), on the other hand, can be given as,

$$u = \frac{u_*}{k}\left[\ln\left(\frac{z-d_0}{z_0}\right) - \Psi_m\left(\frac{z-d_0}{L}\right)\right] \tag{A.5}$$

where Ψ_m is the stability correction function for momentum with Obukhov length L. By assuming neutral stability ($\Psi_m = 0$), neglecting the regional scale displacement height d_0, and by noting $\tau = \rho u_*^2 = F / S$, one can be rewrite (A.4) as

$$\lambda D_{h/2} = k^2\left[\ln\left(\frac{h}{2z_0}\right)\right]^{-2} \tag{A.6}$$

which allows a conversion from z_0 estimated by (A.3) to $D_{h/2}$ to be used in (A.2).

For the actual application, first, λ of the target area was evaluated. Although the original definition of λ is the aerial density, it is not straightforward to determine λ from topographic information. Thus, the streamwise density (Kustas and Brutsaert, 1986; Sugita and Brutsaert, 1990; Hiyama et al., 1996) was used instead in the present analysis, and it was estimated by applying,

$$\lambda = \frac{\sum_{i=1}^{n} y_i}{\sum_{i=1}^{n} \delta_i} = \frac{\sum_{i=1}^{n} y_i}{X} \tag{A.7}$$

where y_i is the height of the ith roughness obstacle, δ_i is the distance between the i-th and (i – 1) th obstacle along the line, and X is the length of the cross-sectional line. To obtain cross sections, two 10-km lines from the KBU site in the major flight directions of respectively, NW

and SE were established and terrain profiles were derived from two types of DEM data set. One of them is with a horizontal resolution of 7-12.5 m and a vertical resolution of 15 m, produced as part of ASTER 3D data set (Abrams, 2000), the other is GTOPO30, which is arranged by the U.S. Geological Survey, with 30-arc second (approximately 70-80 m around study area) horizontal grid spacing and vertical resolution is 18m in this area (http://edc.usgs.gov/products/elevation/gtopo30.html). The value of y_i is taken as the height of the windward side of the obstacles and used in Eq. (A.7) to derive the value of λ. The value of λ and derived z_0 values for each direction of each dataset is presented in Table A-1. Although a difference of resolution makes individual λ and h value for each dataset, the resultant z_0 is found essentially the same, and ASTER dataset was taken for usage in this study.

The local roughness length z_{0l} was estimated by means of (A.5) with the data sets of u_*, u, H and LE measured at the KBU flux station by assuming d_0/h = 2/3. The resulting z_{0l} value was found to be in the range of 10^{-2} to 10^{-4} m during the observation periods. Since there was no clear seasonal trend observed in the derived z_{0l} values, a logarithmic mean value z_{0l} =0.003 m was used in what follows. With these values of $D_{h/2}$ and z_{0l}, the roughness length of the area was determined from (A.2) as z_0 = 0.054 m and z_0 = 0.430 m for NW and SE directions, respectively. The larger roughness of the SE direction was due to the presence of a hilly area as can be seen in Fig.1. With the derived z_0 value, u_* values were evaluated from (A.1) and w_* from h_i and $\overline{w'\theta'}_0$. Note that regional roughness length also can be estimated on the basis of past experience at the other similar site (e.g., Asanuma et al. (2000) listed that of several observation height) when there is no topographic data or a simpler method is required.

A-3 Evaluation of Atmospheric Parameters

The outputs of regional climate model (RCM) was used to evaluating the geostrophic wind, baroclinicity and horizontal temperature advection. As described in chapter 2, these variables were calculated with the space and time average; first the grid data was averaged in period from 9 to 15 in MDST, and then spatial average was calculated in 450×450 km^2 domain for evaluation of the geostrophic wind and baroclinicity parameters. For derivation of horizontal advection,

Table A-1 Estimation of surface roughness length with DEM data.

	ASTER		GTOPO30	
	NW	*SE*	NW	SE
λ	0.0048	0.018	0.0029	0.011
h (m)	7.9	33.3	14.3	52.3
z_{0drag} (m)	0.019	0.30	0.020	0.27
z_{0l} (m)	0.003	0.003	0.003	0.003
z_0 (m)	0.054	0.43	0.066	0.44

λ: roughness density, h: mean height of major obstacles, z_{0drag}: roughness length due to form drag, z_{0l}: roughness length due to skin drag, z_0: roughness length due to these two effects

the 16 grids around the KBU site that cover an area of about 120×120 km^2 were used (see below).

The geostrophic wind components U_g and V_g are

$$U_g = -\frac{1}{\rho f}\frac{\partial p}{\partial y} = -\frac{g}{f}\frac{\partial Z}{\partial y}, \quad V_g = \frac{1}{\rho f}\frac{\partial p}{\partial x} = \frac{g}{f}\frac{\partial Z}{\partial x} \tag{A.8}$$

where ρ is air density, f Coriolis parameter, g gravity acceleration, p air pressure of isohypse plane and Z height of isobaric plane. The isobaric plain gradient i.e., $\partial Z/\partial x$ and $\partial Z/\partial y$ is derived with Z at 800hPa isobaric plane, and, at first, regression analysis was applied to fit a second-order polynomial surface to the isobaric height;

$$Z = A_1 x^2 + A_2 y^2 + A_3 xy + A_4 x + A_5 y + A_6 \tag{A.9}$$

in which A_1 to A_6 is regression coefficients. The partial derivative of (A.9) $\partial Z/\partial x$ and $\partial Z/\partial y$ at the object point was determined with the coordinate of the point as constant.

The components of geostrophic shear (i.e., baroclinicity) is given as thermal wind relation,

$$\frac{\partial U_g}{\partial z} = -\frac{g}{fT}\frac{\partial T}{\partial y}, \quad \frac{\partial V_g}{\partial z} = \frac{g}{fT}\frac{\partial T}{\partial x} \tag{A.10}$$

$\partial T/\partial x$ and $\partial T/\partial y$ are evaluated with temperature data at 800hPa isobaric plane through the same method for the Z gradient evaluation as described above.

The horizontal advection of temperature $\partial \overline{u}\overline{\theta}/\partial x$ and $\partial \overline{v}\overline{\theta}/\partial y$ is derived by rather different process. For five grid points on the each side of 120×120 km^2 (5×5 grids) rectangle surrounding the object grid point, the spatial averaged wind component u, v and temperature θ on the 800hPa isobaric plane were calculated. Then the product $\overline{u}\overline{\theta}$ was evaluated for two of north-south sides and their differential was divided by the distance of two sides at the middle latitude. Also the same process was done for $\overline{v}\overline{\theta}$ for two of west-east sides to obtain $\partial \overline{v}\overline{\theta}/\partial y$.